EJEAS

European Journal of Engineering and Applied Sciences

ISSN:2651-3412. Volume:6 Number:1

ISSN: 2651-3412

European Journal of Engineering and Applied Sciences
http://dergipark.gov.tr/ejeas
Volume 6 Number 1, July 2023

European Journal of Engineering and Applied Sciences

Volume: 6 Number: 1 July 2023

Eur J Eng Appl Sci

https://dergipark.org.tr/tr/pub/ejeas
email: ejeas@nku.edu.tr

ISSN: 2651-3412

ISSN: 2651-3412

European Journal of Engineering and Applied Sciences
http://dergipark.gov.tr/ejeas
Volume 6 Number 1, July 2023

Owner

Correspondance Address

T.N.K.Ü. Çorlu Mühendislik Fakültesi Dekanlığı Silahtarağa Mahallesi Üniversite 1. Sokak No:13 59860
Çorlu / Tekirdağ, TURKEY
e-mail: ejeas@nku.edu.tr
Tel: +90 282 2502300
Fax: +90 282 2509924
Front & Back Pages Designed by Abdurrahman Özdemir

ISSN: 2651-3412

European Journal of Engineering and Applied Sciences
http://dergipark.gov.tr/ejeas
Volume 6 Number 1, July 2023

Yayın hayatına başlarken,

Trakya'nın kalbinde 1992 yılında kurulan Tekirdağ Namık Kemal Üniversitesi Çorlu Mühendislik Fakültesi'nin "European Journal of Engineering and Applied Sciences (EJEAS)" isimli dergisi yayın hayatına başlıyor. Temel ve uygulamalı mühendislik konularında evrensel düzeyde bilgi üretmek, ürettiği bilgiyle teknolojik gelişmelere yön verebilmek ve bu bilgileri toplumsal faydaya dönüştürmek misyonuna sahip fakültemizin bu ilk sayısı ile yayın hayatına kazandırdığı dergimiz yılda iki kez yayınlanacaktır.

European Journal of Engineering and Applied Science (EJEAS) disiplinler arası alanlarda orjinal araştırma makalelerini, vaka çalışmalarını ve teknik raporları, derleme ve analiz raporlarını yayınlamayı amaçlamaktadır. Yayın ücreti bulunmayan ve bilimsel hakemli araştırma dergisinde Fen ve Mühendislik Bilimlerinde deneysel, teorik veya hesaplamalı Türkçe ve İngilizce hazırlanmış güncel ve özgün bilimsel çalışmalara yer verilecektir. EJEAS konusu aşağıdaki disiplinlerdeki çalışmaları kapsayacaktır, ancak konu kapsamı bunlarla sınırlı tutulmayacaktır:

• Otomasyon ve mekatronik mühendisliği
• Biyomedikal mühendisliği
• Bilgisayar bilimi ve yazılım mühendisliği
• İnşaat mühendisliği ve mimarlık
• Elektrik, elektronik ve telekomünikasyon mühendisliği
• Çevre mühendisliği
• Endüstriyel ve imalat mühendisliği
• Makine mühendisliği
• Malzeme bilgisi
• Tekstil mühendisliği

Dergiye gelen tüm çalışmalar çift-kör hakem değerlendirme sürecinden geçerek uygun bulunanalar yayınlanma sürecine alınacaktır.

Bu ilk sayısıyla yayın hayatına başlayan dergimizin size ulaşmasında emeği geçen herkese teşekkür eder, dergimize yayın hayatında başarılar dilerim.

Prof. Dr. Lokman Hakan TECER
Tekirdağ Namık Kemal Üniversitesi, Çorlu Mühendislik Fakültesi Dekanı

ISSN: 2651-3412

European Journal of Engineering and Applied Sciences
http://dergipark.gov.tr/ejeas
Volume 6 Number 1, July 2023

Değerli Bilim İnsanları,

“European Journal of Engineering and Applied Sciences (EJEAS)” isimli dergimiz, 2018 yılında yayın hayatına başlamış olup, bilimsel hakemli dergi olarak, Fen ve Mühendislik disiplinlerinde “Türkçe ve İngilizce” hazırlanmış güncel araştırma ve derleme çalışmalarına yer vermekte ve yılda iki sayı olarak yayınlanmaktadır.

Dergimizin ilk yılında, Tekirdağ Namık Kemal Üniversitesi Çorlu Mühendislik Fakültesi’nin farklı disiplinlerinde görev yapmakta olan çok değerli akademisyenleri, gönüllü olarak dergimizin tüm süreçlerine destek vermiştir. Bu durum bizleri daha güçlü kılmış ve çalışmalarımızda sinerji yaratarak, azim ve kararlılığımıza önemli katkı sağlamıştır. Dergimizin ilerleyen sayılarında daha güçlü bir yapı ile daha iyi noktalara ulaşmasını, alana ve literatüre daha fazla katkı sağlayarak tüm dünyadaki bilim insanları tarafından yayın gönderilen bir dergi konumuna gelmesini ümit ediyorum.

Dergimizin bu iki sayısında değerli çalışmalarını bizimle paylaşıp dergimizde yayınlanmasına katkı sağlayan tüm yazarlarımıza, yayınların değerlendirilmesi ve süreç içerisinde her türlü bilgi ve tecrübesi ile bizleri yanlız bırakmayan çok değerli hakemlerimize, makalelerin dergimizde yayınlanma sürecinin başından sonuna kadar özveriyle çalışan alan editörlerimize ve editörler kurulumuza, bu süreçte desteklerini esirgemeyen Tekirdağ Namık Kemal Üniversitesi Çorlu Mühendislik Fakültesi’nin dekanı sayın Prof. Dr. Lokman Hakan Tecer’e sonsuz teşekkürlerimi sunarım.

Prof. Dr. Aysun SAĞBAŞ
EJEAS Baş Editörü

ISSN: 2651-3412

European Journal of Engineering and Applied Sciences
http://dergipark.gov.tr/ejeas
Volume 6 Number 1, July 2023

Dear Colleagues,

Our “European Journal of Engineering and Applied Sciences (EJEAS)” journal has begun in 2018 as a scientific refereed journal. EJEAS includes up to date Turkish and English languages based research in Science and Engineering and publishes two issues in a year.

In the first year of EJEAS, very valuable academicians of Tekirdag Namik Kemal University have contributed and supported all the processes voluntarily. This made us stronger and with the synergy, it boosted our willingness. I hope that it will achieve better success soon, contribute more to the community, and become a globally recognized journal which publishes journals to entire science community in the world.

For these two issues, I would like to thank our authors who share their studies with us to contribute the journal, our reviewers for assessing the articles with their knowledge and experience, our editors and editorial board for their willingness from the beginning to the end, lastly, dear Dean of Engineering at Tekirdag Namik Kemal University, Prof. Dr. Lokman Hakan Tecer for his ultimate support.

Prof. Dr. Aysun SAĞBAŞ
Editor in-Chief pf EJEAS

ISSN: 2651-3412

European Journal of Engineering and Applied Sciences
http://dergipark.gov.tr/ejeas
Volume 6 Number 1, July 2023

CONTENT

Research Articles

European Journal of Engineering and Applied Sciences

ISSN: 2651-3412 (Print) & 2667-8454 (Online)
Journal homepage: http://dergipark.gov.tr/EJEAS
Published by Çorlu Faculty of Engineering, Tekirdağ Namık Kemal University

European J. Eng. App. Sci. 6(1), 1-7, 2023

Research Article

An Optocoupler-based Biryukov Oscillator Design

Mendi Arapi[1,*], Reşat Mutlu[2]

[1,2] Electronics and Communication Engineering Department, Çorlu Engineering Faculty, Tekirdağ Namık Kemal University, Tekirdağ, Türkiye

[1*]1170605609@nku.edu.tr , [2]rmutlu@nku.edu.tr

Geliş: 05.01.2023 *Kabul: 07.06.2023* *DOI: 10.55581/ejeas.1230140*

Abstract: A Biryukov Equation is a special case of the Liénard equation. Liénard oscillators are commonly found in scientific literature and they have so many variants. The Biryukov Equation is used to model a set of damped oscillators. Unlike other Liénard oscillators, to the best of our knowledge, there is not a Biryukov oscillator that is experimentally examined in the literature, yet. In this study, a Biryukov oscillator is made using a microcontroller-controlled hand-made optocoupler, a negative impedance converter, and a gyrator. An STM32F070RB is used for the required switching. The oscillator's operation has been examined experimentally. The optocoupler made of an LDR and a LED placed in a box allows the resistive switching required by a Biryukov oscillator to occur. The experimental results show that the circuit operates as an oscillator and performs well. It is also shown that an underdamped or an overdamped Biryukov oscillator can be made by varying circuit parameters.

Keywords: *Biryukov Equation, Biryukov Oscillator, Circuit Dynamics*

Bir Optokuplör Tabanlı Biryukov Osilatörü Tasarımı

Öz: Biryukov Denklemi, Liénard denkleminin özel bir halidir. Liénard osilatörleri bilimsel literatürde yaygın olarak bulunur ve pek çok çeşidi vardır. Biryukov Denklemi, sönümlü osilatörlerin bir setini modellemek için kullanılır. Bildiğimiz kadarıyla diğer Liénard osilatörlerinden farklı olarak literatürde henüz deneysel olarak incelenen bir Biryukov osilatörü yoktur. Bu çalışmada, mikrodenetleyici kontrollü el yapımı bir optokuplör, bir negatif empedans dönüştürücü ve bir jiratör kullanılarak bir Biryukov osilatörü yapılmıştır. Gerekli anahtarlama için bir STM32F070RB kullanılmıştır. Bu osilatörün çalışması deneysel olarak incelenmiştir. Kutuya yerleştirilmiş bir LDR ve bir LED'den oluşan optokuplör, Biryukov osilatörünün ihtiyaç duyduğu dirençli anahtarlamanın gerçekleşmesini sağlar. Deneysel sonuçlar, devrenin bir osilatör olarak çalıştığını ve iyi performans gösterdiğini göstermektedir. Ayrıca, devre parametrelerini değiştirerek, düşük sönümlemeli veya aşırı sönümlemeli Biryukov osilatörünün yapılabileceği gösterilmiştir.

Anahtar Kelimeler: *Biryukov Denklemi, Biryukov Osilatörü, Devre Dinamikleri*

1. Introduction

Liénard's equations were proposed by Alfred-Marie Liénard in 1928 to model a set of oscillators [1]. Van der Pol oscillators are a subset of the Liénard equations [2-5]. Van der Pol oscillator and the Liénard Oscillator are historically significant [2, 6]. Liénard and Van der Pol oscillators are commonly used for chaos studies [7-9]. A Liénard Oscillator or a Van der Pol oscillator can be made using various circuit elements such as diodes and lasers [1, 8-12]. Liénard Oscillator circuit has numerous circuit variations. An optical resonance tunneling diode-based oscillator can also be modeled with the Liénard

∗Corresponding author:
E-mail address: 1170605609@nku.edu.tr (M.Arapi)

equation [10]. In [11], a Van der Pol oscillator makes use of anti-parallel Shottky-diode strings. In [12], a Liénard oscillator is made with a nonlinear resistance circuit employing a Schottky-diode bridge fed JFET. An FPGA-based chaotic van der pol oscillator is made in [13] but FPGAs are still expensive devices. A microcontroller-based Liénard oscillator is made in [14]. The Biryukov equation named after Vadim Biryukov is a non-linear second-order differential equation used to model some damped oscillators (Biryukov oscillators) and is also one of the special cases of the Liénard equation [15, 16]. The behavior of limit cycles of the Biryukov equation, considering its applicability has been examined in [17]. The Biryukov oscillator has only been examined with simulations and analytically. To the best of our knowledge, a Biryukov Oscillator has not been made in the literature yet. In this study, a Biryukov Oscillator has been designed and realized for the first time in the literature. Its nonlinear resistor is made using a hand-made optocoupler inspired by [18]. The optocoupler is controlled with a microcontroller. An STM32F070RB is chosen for that purpose. The circuit simulations are done in Matlab™. Then, the circuit is assembled, and its experimental waveforms are acquired. The voltage and the switching function of the Biryukov Oscillator circuit are presented.

The paper is arranged as follows. The second section gives basic information on the Biryukov Equation and the Biryukov Oscillator. In the third section, the proposed Biryukov Oscillator circuit is given. In the fourth section, the switching algorithm of the LED is presented. In the fifth section, Matlab simulations of the Biryukov Oscillator are given. In the sixth section, the experimental results of the circuit are given. The paper is finished with the conclusion section.

2. Biryukov Equation and the Biryukov Oscillator

In this section, the Biryukov Equation is given and briefly explained. The Biryukov equation has been proposed by Vadim Biryukov as

$$\frac{d^2y}{dt^2} + f(y)\frac{dy}{dt} + y = 0 \tag{1}$$

where y is a state variable and $f(y)$ is a piecewise constant function that is positive except for small y and it is expressed as

$$f(y) = \begin{cases} -F, |y| \le Y_0 \\ F, |y| > Y_0 \end{cases} \tag{2}$$

where F and Y_0 are positive constants (F >0 and Y_0>0).

f(y) is an even function since *f(y)= f(-y)*. Eq. (1) is a special case of the Liénard equation; it describes the auto-oscillations dependent on Eq. (2).

The generic Liénard oscillator is made of an inductor, a capacitor, and a nonlinear resistor. The generic Liénard oscillator is shown in Figure 1 [12]. Since the Biryukov equation is also a special case of the Liénard equation, it is also true that the Biryukov oscillator also consists of an inductor, a capacitor, and a nonlinear resistor.

The constitutive equations of the capacitor, the inductor, and the nonlinear resistor are given as

$$i_C(t) = C\frac{dv_C(t)}{dt}, \tag{3}$$

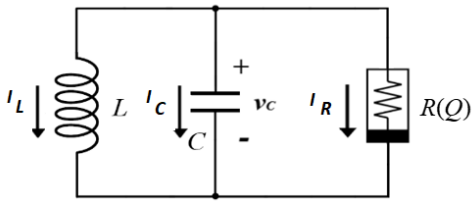

Fig. 1. *The generic Liénard oscillator [12].*

$$v_L(t) = L\frac{di_L(t)}{dt}, \tag{4}$$

and

$$v_R(t) = Ri_R(t). \tag{5}$$

Using Kirchhoff's laws, these following equations can be written:

$$v_R(t) = v_C(t) = v_L(t). \tag{6}$$

and

$$i_R(t) + i_C(t) + i_L(t) = 0 \tag{7}$$

By combining Eq.s (3)-(7), the capacitor voltage of the circuit is described as

$$LC\frac{d^2v_C(t)}{dt^2} + \frac{L}{R(Q)}\frac{dv_C(t)}{dt} + v_C(t) = 0 \tag{8}$$

or

$$\frac{d^2v_C(t)}{dt^2} + \frac{1}{R(Q)C}\frac{dv_C(t)}{dt} + \frac{1}{LC}v_C(t) = 0 \tag{9}$$

where $v_C(t)$ is the oscillator or the capacitor voltage, L is the inductance of the oscillator, $R(Q)$ is the resistance of the oscillator, and C is the capacitance of the oscillator.

We need to obtain a nonlinear resistor. Comparing Eq. (2) and Eq. (9), it is seen that $f(y)$ must satisfy

$$f(y) = \frac{1}{R(Q)C} \tag{10}$$

A nonlinear resistor, whose nonlinear resistance is an even function of voltage, must be used in the Liénard Oscillator and also in the Biryukov oscillator [12]. However, the nonlinear resistor in the Biryukov oscillator can be obtained by switching an active resistor $-R$ and passive resistor R periodically as shown in Figure 2. Therefore, the mechanical switches S_1 and S_2 must be controlled to obtain the desired resistance $R(Q)$. The switching function Q can be expressed as

$$Q = \begin{cases} 1 & , \ |v_C(t)| \le v_{C0} \\ 0 & , \ |v_C(t)| > v_{C0} \end{cases} \quad (11)$$

where v_{C0} is a positive voltage value.

When the switch S is on, Q=1 and vice versa. The resistance value of $R(Q)$ as a function of the switching function is written as

$$(Q) = \frac{1}{f(y)C} = \begin{cases} -\frac{1}{F}, |v_C(t)| \le v_{C0} \\ \frac{1}{F}, |v_C(t)| > v_{C0} \end{cases} = \begin{cases} -\frac{1}{F}, Q = 1 \\ \frac{1}{F}, Q = 0 \end{cases} \quad (12)$$

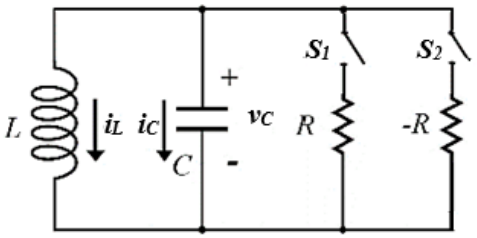

Fig. 2. *A Biryukov oscillator*

3. The Proposed Biryukov Oscillator Topology

The proposed Biryukov oscillator circuit and its components are explained in this section.

3.1. The Optocoupler-based Equivalent Resistor of the Biryukov Oscillator

In [18], a hand-made optocoupler is used to obtain an even resistance function. Such an optocoupler is also used in this study. The circuit schema of the optocoupler and its arrangement in the box are shown in Figure 3. A LED and an LDR are placed in a box to make the optocoupler and it is also wrapped with black bandages to eliminate the effect of the ambient light or the undesired light sources as shown in Figure 3.a. More information about how to design such an optocoupler can be found in [18]. The photographs of the system are given in Figure 3.b. The LDR resistance R_{LDR} is only a function of the light provided by the LED. R_{LDR} takes its minimum value when the LED is on and its resistance is maximum when the LED is off. To make a fine-tuning, the resistance value of the resistor R_1 is adjusted in the experiments so that the LDR resistance can be adjusted as desired for a better performance.

The experimental setup in Figure 4 is used to measure the resistance value of the LDR resistor depending on whether the LED is on or off. LED is controlled with the STM32F070RB microcontroller. Using an ohmmeter, the LDR resistance designated as R_{on} is measured as 136 Ω when the LED is on and the LDR resistance designated as R_{off} is measured as 377 $k\Omega$ when the LED is off.

The switching function Q is defined as equal to 1 if the LED is on. The switching function Q is equal to 0 if the LED is off, The LDR resistance can be described as

$$R_{LDR}(Q) = \begin{cases} R_{on}, |v_C(t)| \le v_{C0} \\ R_{off}, |v_C(t)| > v_{C0} \end{cases} = \begin{cases} R_{on}, Q = 1 \\ R_{off}, Q = 0 \end{cases} \quad (13)$$

It must be provided that

$$R_{off} \gg R_{on} \quad (14)$$

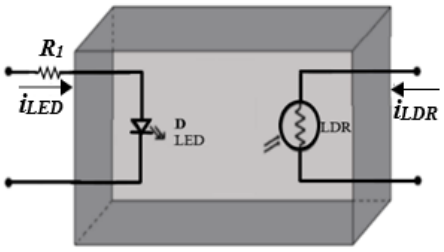

(a)

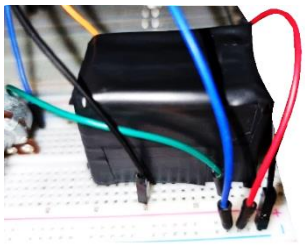

(b)

Fig. 3. *a) The topology and the circuit of the optocoupler and b) the external view of the optocoupler box made.*

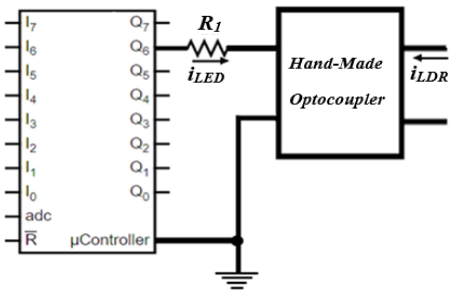

Fig. 4. *Optocoupler test circuit.*

3.2 The Negative Resistance Circuit

An opamp-based negative resistor circuit is shown in Figure 5.a. R_{FB} of the negative resistor circuit is replaced with the optocoupler circuit to obtain the nonlinear resistor of the Biryukov Oscillator as shown in Figure 5.b. Then, the negative resistor's resistance is given as

$$R_{neg} = -R_3 R_{LDR}/R_2 \quad (15)$$

If $R_3 = R_2$, the negative resistor's resistance turns into

$$R_{neg} = -R_{LDR} \tag{16}$$

A microcontroller is used to control the resistance of the LDR in the optocoupler of the oscillator by turning on and off the LED connected to its digital output. The negative resistor circuit is connected in parallel with an LTI resistor whose resistance is equal to R_p=2R_{on} to obtain the nonlinear resistor of the Biryukov oscillator shown in Figure 8.

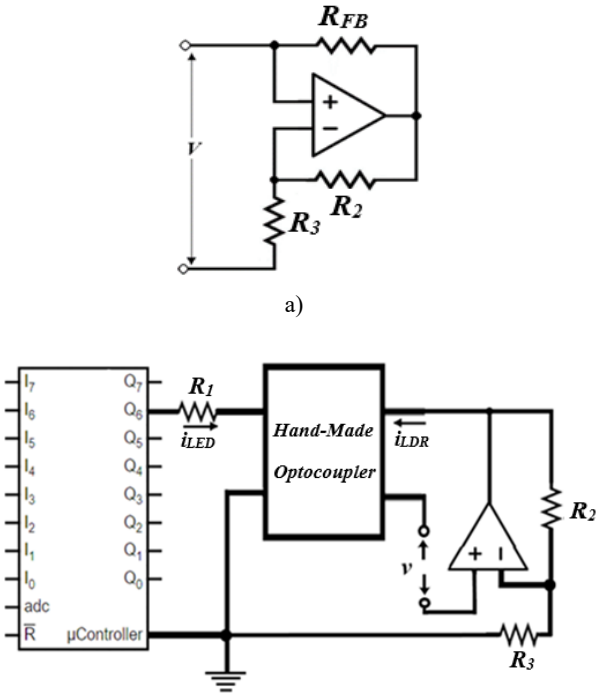

Fig. 5. *a) The opamp-based negative resistor circuit and b) The modified negative resistor circuit of the oscillator.*

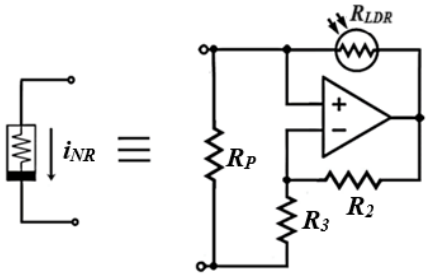

Fig. 6. *The nonlinear resistor of the Biryukov oscillator*

If there is no light:

$$R_{LDR} = R_{off} = 377\ k\Omega \tag{17}$$

Considering the LDR parameters, the following is true:

$$R_{off} \gg R_p \tag{18}$$

If the LED of the optocoupler is off or the LDR is not illuminated, the equivalent resistance of the nonlinear resistor of the Biryukov oscillator can be approximated as follows.

$$R(Q) = R_{ON} = \frac{R_p \cdot (-R_{LDR})}{R_p - R_{LDR}} \cong \frac{R_p \cdot (-R_{max})}{-R_{max}} \cong R_p \tag{19}$$

If the LED of the optocoupler is turned on or the LDR is illuminated:

$$R(Q) = R_{OFF} = \frac{R_p \cdot (-R_{LDR})}{R_p - R_{LDR}} = \frac{2R_{on} \cdot (-R_{on})}{2R_{on} - R_{on}} = -2R_{on} = -R_p \tag{20}$$

3.3. The Gyrator Circuit

Gyrator circuits are commonly used to make adjustable inductors [19]. In this study, A gyrator circuit is also used to obtain the required inductor of the Biryukov oscillator as shown in Figure 7. In periodic steady-state under sinusoidal excitation, its input impedance is given as

$$Z_{in} = (R_L + j\omega R_L R_G C)//\left(R_G + \frac{1}{j\omega C}\right) \tag{21}$$

R_G is chosen sufficiently large such that the RC circuit's impact on the input impedance is negligible. Then, the input impedance of the gyrator is given as

$$Z_{in} = R_L + j\omega R_L R_G C = R_L + j\omega L \tag{22}$$

Then, its input inductance is:

$$L = R_L R_G C \tag{23}$$

If the resistance of the resistor R_L *is* chosen low enough, the gyrator can be assumed to behave as if an ideal inductor. In this study, R_L is taken to be 110 Ω which is much lower than the minimum resistance of the LDR, R_{on}. The resistance value of the resistor R_G is adjusted using a potentiometer.

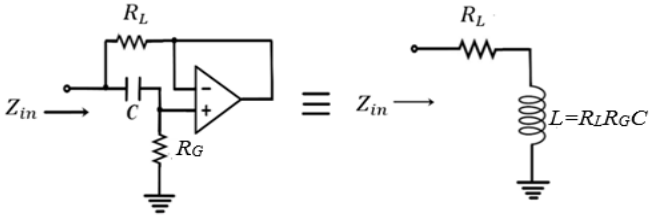

Fig. 7. *The Gyrator circuit behaving as the inductor of the oscillator.*

3.4 The Microcontroller-based Voltage Reading and Optocoupler Control Circuit

The circuit schematic of the microcontroller-controlled Biryukov oscillator circuit is shown in Figure 8. It consists of an STM32F070RB microcontroller, the nonlinear resistor made in the previous section, and the gyrator. The microcontroller controls the LED to adjust the LDR resistance. Adjusting the LDR resistance by turning on and off the LED of the optocoupler results in the oscillation of the circuit. An opamp-based summing circuit that is shown in Figure 8 and has the resistors R_4, R_5 R_6, and R_7, is used to add

up the oscillator voltage with 1.5 V DC voltage before reading it with one of the ADCs of the microcontroller since the microcontroller cannot read negative voltages. This process provides the proper voltage range for the microcontroller`s ADC input. The Microcontroller`s ADC resolution is set to 12-bit and its operating frequency is set to 48 MHz.

4. The Switching Program Algorithm

The microcontroller is programmed in C. The algorithm of the microcontroller program is given as the flowchart shown in Figure 9. The microcontroller reads the capacitor voltage $v_C(t)$ and then compares it with v_{C0}. If the absolute value of $v_C(t)$ is less than v_{C0}, the LED is turned on and vice versa. This is repeated as an infinite loop.

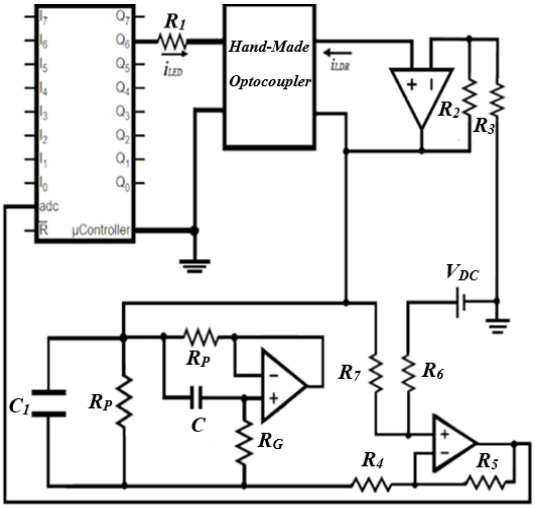

Fig. 8. *The Biryukov oscillator circuit schematic*

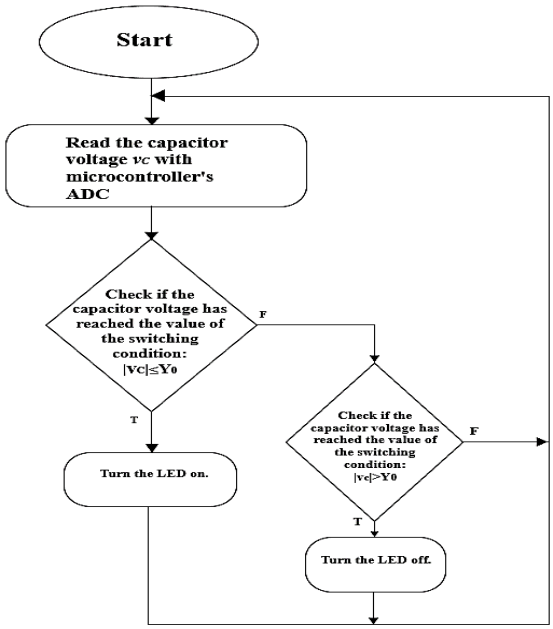

Fig. 9. *The flowchart of the Biryukov oscillator program.*

5. Simulation Results of the Biryukov Oscillator

A simulation program for the oscillator circuit shown in Figure 2 is written in Matlab. The circuit is simulated for two different F values. The Biryukov oscillator voltage $v_C(t)$ is plotted and shown in Figure 11. Both of the waveforms in the periodic steady-state have half-wave symmetry as can be seen in Figure 10.

For a lower value of F such as 0.01, the Biryukov oscillator voltage resembles a sinusoidal signal more as shown in Figure 10.a since the oscillator circuit has a lower equivalent resistance R_p and operates as an almost ideal *L-C* tank circuit. However, it has harmonics.

For a higher value of F such as 4, the capacitor voltage resembles a relaxation oscillator or a sawtooth oscillator signal more as shown in Figure 10.b. since the circuit has a higher resistance R_p. In this case, its harmonic content is much higher.

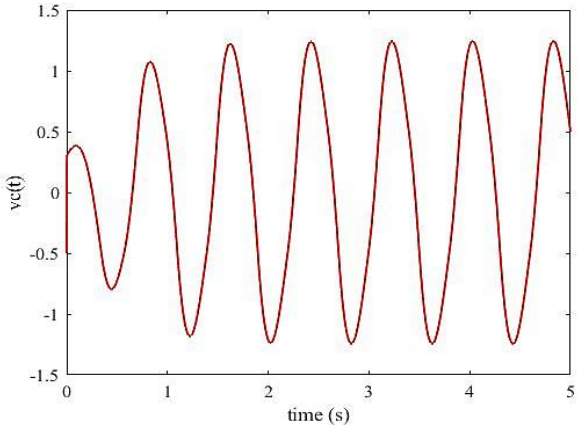

(a)

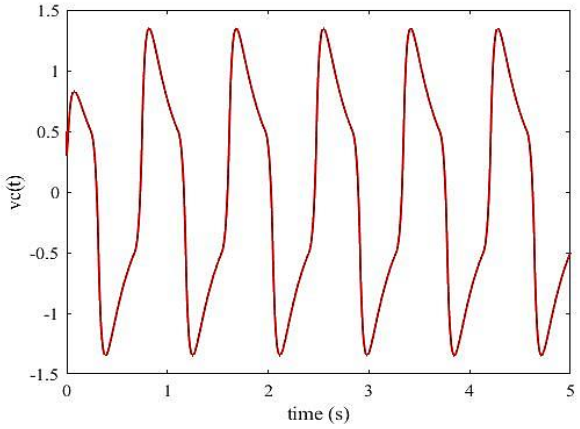

(b)

Fig. 10. *The simulated Biryukov oscillator or the capacitor voltage* $\boldsymbol{v_C(t)}$ *for a) F=0.01 and b) F=4*

6. Experimental Results of the Biryukov Oscillator

In this section, the experimental results of the Biryukov oscillator circuit are given. The Biryukov oscillator circuit is assembled on a protoboard and is also shown in Figure 11. In order to generate the experimental oscillator waveforms, the circuit parameters given in Table 1 is used. The resistance of the resistor R_p is adjusted using a potentiometer and its final value is given in Table 1. The experimental waveforms are acquired by the STM32CubeMonitor that is a monitor program installed on a PC. The application helps to fine-tune and diagnose STM32 applications at run-time by reading and

visualizing their variables in real-time. The STM CubeMonitor which interfaces with the microcontroller STM32F070RB in real time and shows the variation of the capacitor voltage variable $v_C(t)$ in this study. The microcontroller is connected with the PC via usb 3.0 and the monitor program operates at 4.6 MHz frequency. The acquired experimental time domain waveforms are shown in Figure 12. The capacitor voltages have 1.5 Volt DC offset since the oscillator waveform is summed with a 1.5 Volt DC voltage as can be seen in Figure 12. The experimental results shown in Figure 12 resemble the simulated ones given in Figure 10 and it can be said that the Biryukov Oscillator can produce the desired state variable $v_C(t)$ and performs well. An underdamped and an overdamped Biryukov oscillator can be made by varying circuit parameters as shown in Figure 12 respectively.

Table 1 Circuit parameters.

	Circuit Parameters for the waveform given in Figure 13.a	Circuit Parameters for the waveform given in Figure 13.b
R_p	4.2 $k\Omega$	3.8 $k\Omega$
R_{LDR}	2.32 $k\Omega$	1.7 $k\Omega$
C_1	2.2 μF	2.2 μF
C	10 μF	10 μF
R_L	110 Ω	110 Ω
R_G	8.279 $k\Omega$	39 $k\Omega$
R_2	51 $k\Omega$	51 $k\Omega$
R_3	51 $k\Omega$	51 $k\Omega$
R_4	22 $k\Omega$	22 $k\Omega$
R_5	22 $k\Omega$	22 $k\Omega$
R_6	18 $k\Omega$	18 $k\Omega$
R_7	18 $k\Omega$	18 $k\Omega$

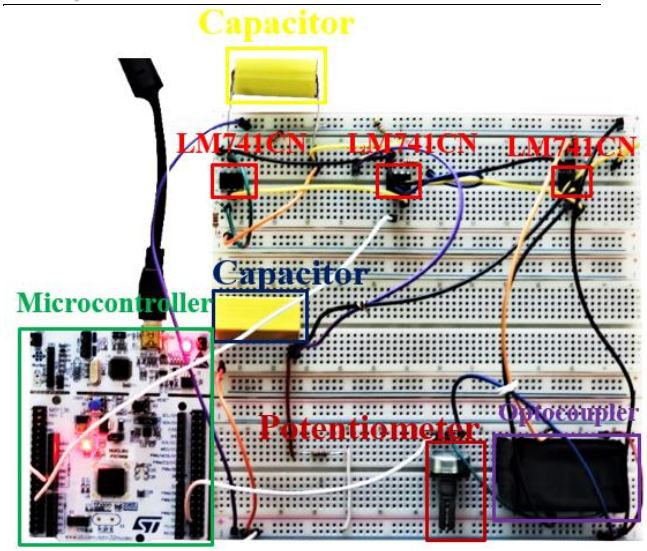

Fig. 11. *Photograph of the implemented Biryukov oscillator circuit.*

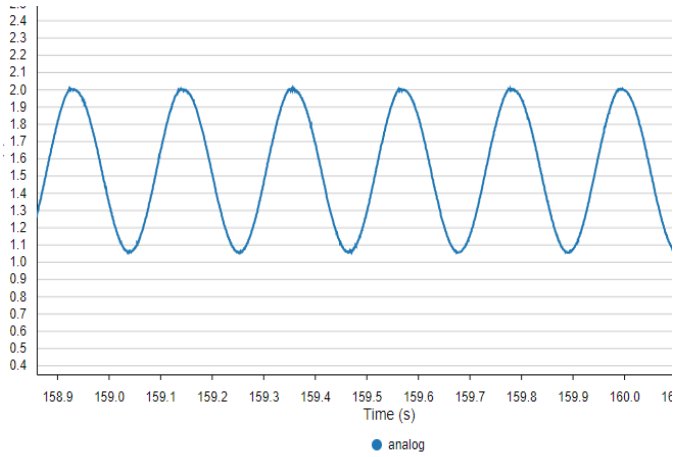

(a)

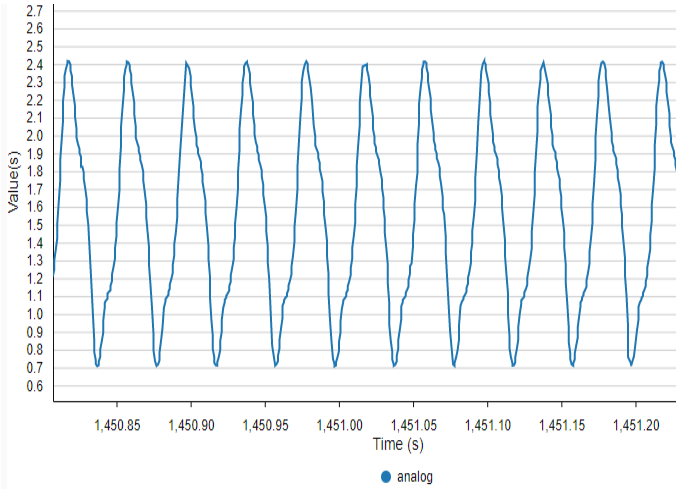

(b)

Fig. 12. *The experimental Biryukov Oscillator voltage $v_C(t)$ for a) F=0.01 (the underdamped case) and b) F=4 (the overdamped case)*

7. Conclusions

In this paper, a microcontroller-based Biryukov Oscillator is made for the first time in the literature. In this work, a cheap and easy-to-use STM32F070RB microcontroller is preferred for this purpose. With one of its ADCs, it reads the capacitor voltage and controls the LED via its digital output. To the best of our knowledge, the Biryukov oscillator signal has been obtained in analog form for the first time in the literature. The experiments have confirmed that the circuit operates as a Biryukov Oscillator. It is also shown that it is possible to obtain an underdamped and an overdamped Biryukov oscillator by varying the oscillator parameters. As a future work, by modifying the light intensity produced by the LED controlled by the microcontroller, new types of oscillator waveforms can be obtained. The Biryukov oscillator circuit can also be employed in circuit laboratories for educational purposes. The coupling of the Van der Pol or Liénard Oscillators is a hot research topic and the coupling of a Biryukov oscillator with the other oscillators can also be examined in the future.

Author Contribution

Formal analysis –Reşat Mutlu (RM); Investigation – RM; Experimental Performance – Mendi Arapi (MA); Data

Collection RM– MA; Processing – MA; Literature review – RM; Writing – RM, MA; Review and editing – RM, MA;

Declaration of Competing Interest

The authors declared no conflicts of interest with respect to the research, authorship, and/or publication of this article.

References

[1] A. Liénard, Etude des oscillations entretenues, Revue générale de l'électricité, 23, pp. 901–912 and 946–954, 1928

[2] B. van der Pol, A theory of the amplitude of free and forced triode vibrations, Radio Review, 1, pp. 701–710, 754–762, 1920.

[3] J. M. Ginoux, C. Letellier. (2012). Van der Pol and the history of relaxation oscillations: Toward the emergence of a concept, *Chaos: An Interdisciplinary Journal of Nonlinear Science*, 22(2), 023120, 2012.

[4] B. Van der Pol, LXXXVIII. (1926). On "relaxation oscillations", *The London, Edinburgh, and Dublin Philosophical Magazine and Journal of Science*, 2(11), 978-992.

[5] B. van der Pol, The nonlinear theory of electric oscillations, Proc. IRE, 22, pp. 1051–1086, 1934.

[6] M. L. Cartwright, I. Van der Pol's Equation for Relaxation Oscillations, In Contributions to the Theory of Nonlinear Oscillations (AM-29), Volume II, Princeton University Press., (pp. 1-18), 2016.

[7] J. Gleick, M. Berry. (1987). Chaos-making a new science, *Nature*, 330, 293.

[8] S. Ahmad, Study of Non-linear Oscillations Using Tunnel Diode, Doctoral dissertation, 1962.

[9] J. Brechtl, X. Xie, P. K. Liaw. (2019). Investigation of chaos and memory effects in the Bonhoeffer-van der Pol oscillator with a non-ideal capacitor, *Communications in Nonlinear Science and Numerical Simulation*, 73, 195-216.

[10] T. J. Slight, B. Romeira, L. Wang, J. M. Figueiredo, E. Wasige, C. N. Ironside, (2008). A Liénard oscillator resonant tunnelling diode-laser diode hybrid integrated circuit: model and experiment, *IEEE Journal of Quantum Electronics*, 44(12), 1158-1163.

[11] Çakır, K., Mutlu, R., & Karakulak, E. (2021). Ters-Paralel Bağlı Schottky Diyot Dizisi Tabanlı Van der Pol Osilatörü Devresinin Modellenmesi ve LTspice ve Simulink Kullanarak Analizi. *EMO Bilimsel Dergi*, 11(21), 81-91.

[12] Çakır, K., Mutlu, R. (2022). Modeling and analysis of Schottky Diode Bridge and JFET based Liénard Oscillator circuit. DOI:10.14744/sigma.2022.00082.

[13] Dursun, M., Kaşifoğlu, E. (2018). Design and implementation of the FPGA-based chaotic van der pol oscillator. *International Advanced Researches and Engineering Journal*, 2(3), 309-314.

[14] Mevsim, E., Mutlu, R. (2022). A Microcontroller-based Liénard Oscillator. *European Journal of Engineering and Applied Sciences*, 5(2), 80-85.

[15] Pilipenko A. M., and Biryukov V. N. (2013). Investigation of Modern Numerical Analysis Methods of Self-Oscillatory Circuits Efficiency. *Journal of Radio Electronics*, 9 ,1-9.

[16] Biryukov, V. N., Gatko. L (2012). Exact stationary solution of the oscillator nonlinear differential equation, *Nonlinear World*, 10(9), 613–616.

[17] Gasimov, Y. S., Guseynov, S. E., & Valdés, J. E. N. (2020). On some properties of limit cycles of the Biryukov equation. Proceedings of the Institute of Mathematics and Mechanics, Azerbaijan National Academy of Sciences, 46(2), 321-345.

[18] Tulumbacı, F., & Mutlu, R. (2021). An optoelectronic-based memristor emulator circuit with a rational memristance function. Optoelectronics and Advanced Materials, *Rapid Communications*. 15(9-10), 487-497.

[19] Karakulak, E. Mutlu, R. (2016). Adjustable Inductor using a memristor for integrated circuits, Materials, *Methods & Technologies*, 10, 283-293.

European Journal of Engineering and Applied Sciences

ISSN: 2651-3412 (Print) & 2667-8454 (Online)
Journal homepage: http://dergipark.gov.tr/EJEAS
Published by Çorlu Faculty of Engineering, Tekirdağ Namık Kemal University

European J. Eng. App. Sci. 6(1), 8-18, 2023

Research Article

Comparative Thermodynamic Optimization of Organic Rankine Cycle Configurations for Geothermal Power Generation from an Abandoned Oil Well

Joseph Oyekale[1,*], Oluwaseun Olawumi Adetona[2]

[1] Department of Mechanical Engineering, Federal University of Petroleum Resources, Effurun, P.M.B. 1221 Effurun, Delta State, Nigeria
[2] Department of Petroleum Engineering and Geosciences, Petroleum Training Institute, Effurun, P.M.B. 20 Effurun, Delta State, Nigeria
[1*]oyekale.oyetola@fupre.edu.ng, [2]sadetona@yahoo.com

Received: 15.03.2023 *Accepted: 22.07.2023* *DOI: 10.55581/ejeas.1265828*

Abstract: This study was aimed at quantifying the net electrical power producible from an abandoned oil well in Nigeria using different organic Rankine cycle (ORC) configurations and working fluids. The geological features of a typical Nigerian oil well were employed in the study and a borehole heat exchanger was used for simulating the thermodynamic parameters of the heat source. Specifically, a subcritical ORC without a recuperator (SBC), a subcritical ORC with a recuperator (SBC-R), a supercritical ORC without a recuperator (SPC), and a supercritical ORC with a recuperator (SPC-R) were analyzed, using R115, R236fa, and R1234yf as working fluids. Results showed that between 272 kW and 875 kW of electrical power could be produced from the abandoned oil well using the most basic ORC configuration (SBC). Furthermore, it was obtained that the introduction of a recuperator would increase the ORC net power by about 13% for R236fa, 33% for R1234yf, and 107% for R115. Similarly, a switch from a subcritical ORC to a supercritical ORC configuration would increase net power for all the working fluids. Specifically, an increase in net power was estimated at 3.6% for R236fa, 46% for R1234yf, and 152% for R115 regarding a switch from the SBC to the SPC. Moreover, decreasing the condensation pressure of the ORC plants was observed to improve net power in all cases.

Keywords: Abandoned Oil Well Retrofit, Geothermal Power Production, Organic Rankine Cycle, Energy Efficiency, Sustainable Energy System.

Terk Edilmiş Bir Petrol Kuyusundan Jeotermal Enerji Üretimi İçin Organik Rankine Çevrim Konfigürasyonlarının Karşılaştırmalı Termodinamik Optimizasyonu

Öz. Bu çalışma, farklı organik Rankine çevrimi (ORC) konfigürasyonları ve çalışma sıvıları kullanılarak Nijerya'da terk edilmiş bir petrol kuyusundan üretilebilen net elektrik gücünü ölçmeyi amaçlıyordu. Çalışmada tipik bir Nijerya petrol kuyusunun jeolojik özellikleri kullanılmış ve ısı kaynağının termodinamik parametrelerini simüle etmek için bir sondaj kuyusu ısı eşanjörü kullanılmıştır. Spesifik olarak, geri kazanım cihazı olmayan bir kritik altı ORC (SBC), bir geri kazanım cihazı olan bir kritik altı ORC (SBC-R), bir geri kazanım cihazı olmayan bir süper kritik ORC (SPC) ve bir geri kazanım cihazı olan bir süper kritik ORC (SPC-R) kullanılarak analiz edildi. Çalışma sıvıları olarak R115, R236fa ve R1234yf. Sonuçlar, en temel ORC konfigürasyonu (SBC) kullanılarak terk edilmiş petrol kuyusundan 272 kW ile 875 kW arasında elektrik enerjisinin üretilebileceğini gösterdi. Ayrıca, bir geri kazanım cihazının eklenmesinin ORC net gücünü R236fa için yaklaşık %13, R1234yf için %33 ve R115 için %107 artıracağı elde edildi. Benzer şekilde, kritik altı bir ORC'den süper kritik bir ORC konfigürasyonuna geçiş, tüm çalışma sıvıları için net gücü artıracaktır. Spesifik olarak,

*Corresponding author
E-mail: oyekale.oyetola@fupre.edu.ng (J. Oyekale)

SBC'den SPC'ye geçişle ilgili olarak net güçteki artışın R236fa için %3,6, R1234yf için %46 ve R115 için %152 olduğu tahmin edilmiştir. Ayrıca, ORC tesislerinin yoğuşma basıncının düşürülmesinin her durumda net gücü iyileştirdiği gözlemlenmiştir.

Anahtar Kelimeler: Terk Edilmiş Petrol Kuyusu Güçlendirmesi, Jeotermal Enerji Üretimi, Organik Rankine Çevrimi, Enerji Verimliliği, Sürdürülebilir Enerji Sistemi.

1. Introduction

Crude oil and gas are among the most sought-after fossil fuels due to their substantial contribution to powering the world and the enormous economic benefits that accrue to any nation where they are deposited [1]. Depending on the geological features of the earth containing oil and gas reserves, wells are to be dug in varying degrees of depth for profitable oil and gas explorations [2]. But since oil reserves are non-renewable and would deplete from the wells over time [3], adequate measures are statutorily required for proper decommissioning and termination of wells at their end of life [4]. However, standard oil decommissioning processes add sizeable costs to the operational expenses of oil well development [5]. Also, it is common for oil and gas wells to simply be abandoned in some regions with weak legal frameworks on such practices, thereby contributing hazards to the environment [6]. Thus, alternative ways of elongating the useful life of oil and gas wells are currently being researched in the literature [7], [8], [9] to minimize production costs and environmental impacts in the oil and gas industry.

The conversion of abandoned oil wells to geothermal energy sources is one viable way being explored in the literature to prolong the useful life of oil and gas wells [10]. As the oil and gas reserves in a typical well approach depletion, continuous production becomes unprofitable, and it is believed that a modification of the oil well's purpose to generate geothermal energy can be a viable alternative. The geothermal energy so generated can be used directly for heating purposes and it can be converted to electrical power using a power cycle such as the organic Rankine cycle (ORC). The ORC is particularly suited for the production of power from geothermal energy of an abandoned oil well due to the use of an organic working fluid with a low boiling point, which can be evaporated by a low-temperature heat source. Several studies have proposed and analyzed different possible schemes for the conversion of abandoned oil wells to geothermal energy sources and profitable production of useful energy products therefrom. The most striking of such studies are succinctly reviewed in the following paragraph.

Liu et al. [11] reviewed critically the oil and gas reservoirs globally where heat energy is being harnessed for power production in practice, or the potential being investigated. They then proposed a roadmap that could be used to screen mature oil and gas reservoirs for a profitable conversion to a geothermal power source. A quantitative analysis conducted based on the Villafortuna-trecate oil field in Italy revealed that a 500 kW power plant could be sustainably serviced, with the capacity to generate a total of 25 GWh of electrical power in 10 years. Chmielowska et al. [12] surveyed the world trend on the utilization of oil wells as geothermal energy sources and reiterated that it is increasingly being implemented in reality, particularly with the use of borehole heat exchangers. Duggal et al. [13] identified the conversion technology choice, transient ambient conditions, and fluid handling system among the issues that should be handled well for maximum benefits from geothermal power production from an oil well. Also, Oyekale and Emagbetere [14] discussed some steps that could be taken for a quick feasibility assessment of geothermal power production from abandoned oil and gas wells. Kaplanoglu et al. [15] reported that the use of downhole heat exchangers can facilitate the conversion of abandoned oil wells to geothermal sources in Southeastern Turkey for an improved economy of the region. Gong et al. [16] employed the technical features of the LB reservoir from the Huabei oil field (China) to simulate numerically the effects of mass flow rate and temperature of the injected water on the reservoir temperature. They identified the limits of the injection mass flow rate and temperature at which geothermal energy can be co-produced efficiently in a reservoir. Mehmood et al. [17] reported that abandoned oil wells can not only be repurposed for geothermal power production in China but also the power can be generated at a competitive price relative to other energy sources. Naseer et al [18] demonstrated the possibility of improving the sustainability of repurposing abandoned oil and gas wells by a coproduction of electricity and power, with additional potential for direct H_2S and CO_2 capture. Gharibi et al. [19] studied the feasibility of using a U-tube heat exchanger to extract geothermal energy from abandoned oil wells based on the real data of such a well in Southern Iran. They reported that the U-tube heat exchanger is adequate for the extraction both for direct use of the geothermal energy and for power conversion. Wight and Bennett [20] demonstrated the advantages of using water as the wellbore fluid in conjunction with a closed well, for the generation of electrical power from abandoned oil wells using binary power plants. Based on the well log data for over 2500 wells in Texas (USA), the authors obtained the possibility of net power generation in the range of 190 kW – 630 kW. Similarly, Milliken [21] estimated the power producible from the Naval Petroleum Reserve 3 (NPR-3) at about 300 kW based on the available technologies in the early 2000s, although thermal energy equivalent to about 22 MW power was estimated to be lost daily. Sanyal and Butler [22] discussed the basic technological and cost requirements for geothermal energy production from abandoned oil wells, those still in use but with high water cuts, and geo-pressured brine wells with dissolved gas. Case histories were also presented for the estimation of available power capacity in a well or a group of wells. Harris et al. [23] investigated the potential of directionally drilled wells in maximizing geothermal power production from abandoned oil wells. Based on 2 vertically drilled wells each 4000 m deep and a horizontally drilled well 4800 m, the authors estimated the production of 2 MW of thermal energy which could be converted to about 200 kW of electrical power using an ORC plant. Noorollahi et al. [24] estimated from a numerical simulation that about 138 kW and 364 kW of electrical power can be generated respectively from the AZ-II and DQ-II wells in the Ahwaz oil field in Southern Iran. Patihk et al. [25] obtained that about 4.4 GWe can be produced from 6 wells in the Forest Reserve Field in Trinidad over 25 years of

operation, at an $0.05 electricity cost, saving about 50 Mtons of CO_2 cumulatively. Singh [26] also reported a survey of Indian oil fields with their potential for geothermal power production either with the use of a downhole heat exchanger or by in-situ combustion of hydrocarbons in the wells that are hard to exploit.

The foregoing literature review is a testament to the global interest in geothermal energy production from oil and gas wells with high water cuts which is particularly common with abandoned wells. Also, ORC can be identified as a viable power conversion technology for the exploitation of geothermal energy from oil and gas wells. However, the majority of the literature studies on this subject focused hitherto on feasibility assessments with little or no detail on the effects of ORC thermodynamic characteristics on performance. Additionally, no specific technical feasibility studies exist for power generation from abandoned oil and gas wells in Nigeria, despite ranking the largest oil producer in Africa and the 12th largest in the world as of 2016 [27]. Thus, this study investigates for the first time the power production potential of ORC plants utilizing geothermal energy from an abandoned oil well in Nigeria. Moreover, emphasis is placed on the impacts of ORC configurations and working fluids on the performance, thereby closing an existing gap in the field as aforementioned. The specific objectives of the study are:

- To quantify the geothermal electrical power producible from a typical abandoned oil well in Nigeria using thermodynamically optimized ORC plants with different working fluids;
- To assess the technical impacts of incorporating an internal heat recuperator on the ORC performance for the intended heat source;
- To assess the impacts of adopting a supercritical configuration on the ORC performance for the oil well based geothermal energy source;
- To investigate the sensitivities of the optimal ORC parameters to a change in the condensation temperature of the cycle.

2. Materials and Methods

2.1 System Configuration

The heat source comprises a coaxial borehole heat exchanger (BHE) exploiting the thermal contents of an abandoned oil well in form of geothermal energy. The numerical analysis presented in [28] was adopted in this study using the geometrical parameters of a typical abandoned oil well in the Niger Delta region of Nigeria [29]. The main features of the abandoned well and the BHE are highlighted in Table 1. The main interest in this study for the COMSOL simulation of the BHE [28] is the temperature of the geothermal fluid (brine) that could be generated from the abandoned well, for the production of electrical power using the ORC system.

Four ORC configurations were analyzed for the same abandoned oil well turned geothermal energy heat source. The first ORC configuration is a subcritical ORC configuration without a recuperator, dubbed SBC in this study. The highest cycle pressure of a subcritical ORC plant is below the critical pressure of the working fluid, while an ORC plant having no recuperator connotes that the working fluid leaving the turbine condensed directly without recouping/re-using its heat within the cycle. The second ORC configuration analyzed in this study assumes a subcritical type still, but a recuperator is added, dubbed here as SBC-R. Here, the recuperator utilizes the thermal energy content of the organic working fluid exiting the turbine to pre-heat the liquid working fluid leaving the pump before the geothermal heat source is applied in the evaporator/pre-heater. The third configuration considered is a supercritical ORC type with no recuperator, dubbed SPC in this study. By definition, supercritical/transcritical ORC plants have the minimum cycle pressure to be less than the working fluid critical pressure but the maximum cycle pressure (evaporation pressure) to be greater. Lastly, the fourth ORC configuration analyzed in this study assumes a supercritical ORC type with a recuperator, dubbed here as SPC-R. For each of the four ORC configurations, the organic working fluids R115, R236fa, and R1234yf were analyzed. These working fluids were selected based on their good acceptance as suitable working fluids in real ORC plants [30], [31], [32]. Air is considered the heat sink for all the ORC configurations considering the scarcity of water in most West African countries. Moreover, brine is considered the heat transfer mechanism from the geothermal well to the ORC plant, as aforementioned. Figures 1a and 1b illustrate the ORC configuration with and without a recuperator, respectively. Again, the figures could suffice for both the subcritical and supercritical configurations depending on the state properties employed during ORC design.

2.2 Design Modeling of the ORC Configurations

Zero-dimensional models based on the First Law of Thermodynamics were employed for the design modeling of the ORC plants for the different configurations investigated in this study. Specifically, each component of the ORC plant was modeled to satisfy the general mass and energy balance equations defined in (1) and (2), respectively. The actual models that apply for the ORC configurations with and without a recuperator are discussed hereunder.

$$\sum \dot{m}_i = \sum \dot{m}_o \tag{1}$$

$$\sum \dot{m}_i h_i + \dot{Q} = \sum \dot{m}_o h_o + \dot{W} \tag{2}$$

The symbols $\dot{m}$, h, $\dot{Q}$, and $\dot{W}$ denote respectively the mass flow rate, state enthalpy, heat energy inlet, and work output. The subscripts '*i*' and '*o*' signify inlet and outlet flow for a given component.

2.2.1 ORC Plant Without a Recuperator

The ORC unit interacts with the heat source (marine engine exhaust gas heat) through the evaporator and the preheater. Referring to Fig. 1a, the total heat supplied to the ORC externally is given by:

$$\dot{Q}_{HS} = \dot{m}_{HTF} c_p (HTF\_T_i - HTF_{T,o}) = \dot{m}_{OF}(h_{OF,4} - h_{OF,2}) \tag{3}$$

where $HTF\_T_{,i}$ and $HTF\_T_{,o}$ represent respectively the inlet and the exit temperatures of the heat source, and the subscripts '*HS'* and '*OF'* represent respectively the heat source and the ORC working fluid.

The expander power output is given by:

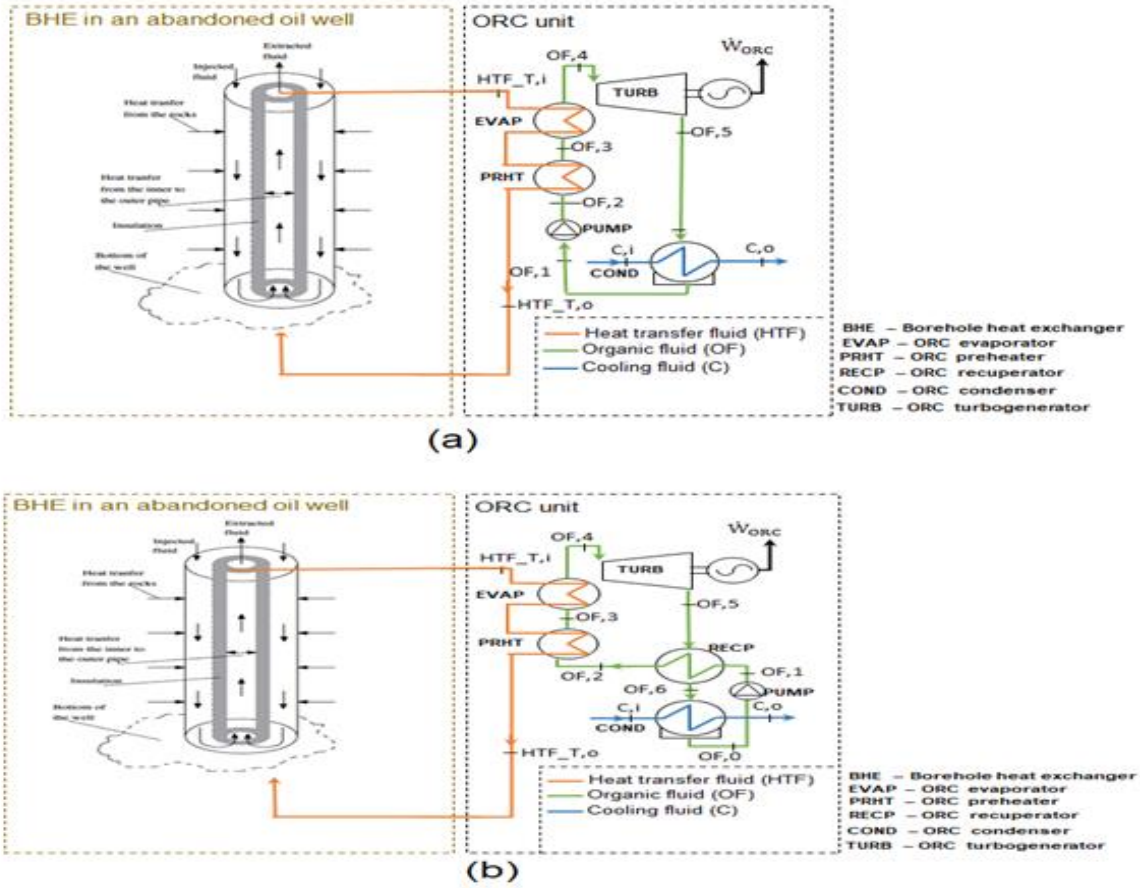

Fig. 1. *Interaction of the geothermal energy from an abandoned oil well with the ORC unit*

$$\dot{W}_{TURB} = \dot{m}_{OF}(h_{OF,4} - h_{OF,5}) = \dot{m}_{OF}(h_{OF,4} - h_{OF,5s})\eta_{s,T} \quad (4)$$

where $\eta_{s,T}$ is the turbine isentropic efficiency. The heat rejected by the condenser is given by

$$\dot{Q}_{COND} = \dot{m}_{OF}(h_{OF,5} - h_{OF,1}) = \dot{m}_{C}(h_{C,o} - h_{C,i}) \quad (5)$$

where the subscript 'c' represect the coolog fluid taken as air in this study.

The power consumed by the pump is given by:

$$\dot{W}_{PUMP} = \dot{m}_{OF}(h_{OF,2} - h_{OF,1}) = \dot{m}_{OF}\frac{(h_{OF,2s} - h_{OF,1})}{\eta_{s,P}} \quad (6)$$

where $\eta_{s,P}$ is the pump isentropic efficiency.

The net power output is given by:

$$\dot{W}_{NET} = \dot{W}_{TURB} - \dot{W}_{PUMP} - \dot{W}_{C} \quad (7)$$

where $\dot{W}_C$ is the power expended to drive the cooling air through the condenser.

The ORC thermal efficiency (η_{th}) is given by:

$$\eta_{th} = \frac{\dot{W}_{NET}}{\dot{Q}_{HS}} \quad (8)$$

2.2.2 ORC plant with a recuperator

The same principle applies to modeling the ORC configuration with a recuperator as illustrated in Fig. 1b. The heat supplied to the ORC unit and the turbine work output has the same models as defined in eq. 3 and eq. 4, respectively. The heat rejected by the condenser is slightly adjusted with the introduction of thermal recuperation within the system, given in this case by:

$$\dot{Q}_{COND} = \dot{m}_{OF}(h_{OF,6} - h_{OF,0}) = \dot{m}_{C}(h_{C,o} - h_{C,i}) \quad (9)$$

The pump power consumption is given by:

$$\dot{W}_{PUMP} = \dot{m}_{OF}(h_{OF,1} - h_{OF,0}) = \dot{m}_{OF}\frac{(h_{OF,1s} - h_{OF,0})}{\eta_{s,P}} \quad (10)$$

The internal heat recuperated within the system is given by

$$\dot{Q}_{RECP} = \dot{m}_{OF}(h_{OF,5} - h_{OF,6}) = \dot{m}_{OF}(h_{OF,2} - h_{OF,1}) \quad (11)$$

The net power output and the ORC thermal efficiency for this configuration also have the same models as defined

respectively by eq. 7 and eq. 8. The design modeling and simulation were implemented in MATLAB for all the configurations examined.

2.2.3 Optimization approach of the ORC systems

The optimization models which were also programmed in MATLAB defined the maximization of the net power output of the ORC plant as the objective function. For each of the ORC configurations considered, the optimization tools require the following input parameters:

- The temperature of the HTF (heat source) at the ORC exit;
- The minimum cycle (condensation) temperature; and
- HTF mass flow rate at the ORC inlet.

Additionally, other cycle parameters were fixed in the optimization tools as independent variables, as follows:

- Pinch point temperatures of the heat exchangers (evaporator; pre-heater; condenser; and recuperator in the case of the SBC-R and SPC-R);
- Isentropic and electromechanical efficiencies of the pump;
- Isentropic and electric generator efficiencies of the turbine; and
- Mechanical efficiency of the fan.

The values assigned to these fixed variables are highlighted in Table 1.

The decision variables optimized by the tool to maximize net output power are as follows:

- Maximum pressure and temperature of the ORC;
- ORC working fluid mass flow rate;
- Degree of superheat; and
- Minimum cycle pressure.

2.4 Sensitivity analysis

The sensitivity of the objective function (net output power) to the condensation temperature of the HTF heated by the engine exhaust gas was also investigated in the study. This was considered necessary to take into account the transient operation of the ORC system in which case a change in ambient conditions would vary thermodynamic properties during condensation, with a consequence on the overall system performance. Additionally, ORC thermal efficiency that corresponds to each output power was also computed during the sensitivity analysis for all the ORC configurations. Suffice it to mention that the optimization models were used for the sensitivity analysis, such that the results obtained remain the optimal choices for each of the working fluids and ORC configurations.

Table 1 Characteristics of the heat source and the ORC plant

Abandoned oil well and BHE		ORC unit	
Well head	4500 m	Working fluid	R115, R236fa, and R1234yf
BHE tube radius	3.8 cm	Heat sink	Air
BHE annulus radius	8.9 cm	Net electrical power	Optimized
BHE thickness	1 cm	Nominal input thermal power	Decision variable
Brine temperature	155 ^{o}C	Nominal HTF flow rate	Decision variable
		Isentropic efficiency - pump	0.80
		Motor efficiency - pump	0.98
		Isentropic efficiency - turbine	0.85
		Electromechanical efficiency	0.92
		Mechanical efficiency – cooling fan	0.60
		Pinch point temperature difference	5 ^{o}C

3. Results and Discussion

3.1 Thermodynamic optimization results for the different ORC configurations for utilizing geothermal energy from an abandoned oil well

The most significant thermodynamic optimization results are reported in this section for the ORC schemes and working fluids analyzed in this study.

3.1.1 Subcritical ORC without a recuperator (SBC)

Table 2 reports the main results of thermodynamic optimization for the SBC configuration, for the 3 working media examined in this study. As can be seen, electrical power of between about 273 kW and 875 kW can be produced from the referenced abandoned oil well when converted to a geothermal energy source, using the SBC. Specifically, using R236fa as the ORC working fluid for utilizing geothermal energy from the abandoned oil well would yield the highest net power, about 44% and 220% above what is obtainable using the fluids R1234yf and R115, respectively. Similarly, the SRC with working fluid R236fa would convert the geothermal energy to power at a thermal efficiency of about 7.19%, more efficient than using R1234yf and R115 by around 2.7 percentage points, and 5.2 percentage points, respectively. Furthermore, it is noteworthy that using R115 would mean that about 786 kW of the total power production would be expended as an auxiliary energy, instead of about 752 kW for R1234yf and 713 kW for R236fa. The cycle auxiliary energy is very high for all the fluids due to the use of air as the heat sink, requiring substantial electrical power to drive the fan.

3.1.2 Subcritical ORC with recuperator (SBC-R)

The basic thermodynamic optimization results for the SBC-R are highlighted in Table 3, referencing the 3 working fluids investigated in this study. Again, the fluid R236fa was obtained with the highest net power of about 992 kW for the SBC-R utilizing geothermal energy from the abandoned oil well. Additionally, for the SBC-R, the fluid R1234yf yielded net power about 180 kW below R236fa and about 247 kW

beyond R115. It suffices to report explicitly here that a switch from the SBC to the SBC-R would yield a more thermodynamically efficient system irrespective of working fluid. Specifically, a comparative analysis of the SBC and the SBC-R reveals that net power would increase by around 13% for R236fa, 33% for R1234yf, and 107% for R115, while thermal efficiency would increase by about 1 percentage point for R236fa, 3.3 percentage points for R1234yf, and 3.8 percentage points for R115. It thus means that the introduction of a recuperator is less significant with increasing net power and thermal efficiency facilitated by the choice of an optimal ORC working fluid.

Table 2 Thermodynamic optimization results for the subcritical ORC plant without a recuperator

Parameter	R115	R236fa	R1234yf
Net Work (kW)	272.8	874.8	609.3
Pump Work (kW)	201.2	223.2	192.4
Fan Work (kW)	585.0	490.1	560.0
Max Pressure (MPa)	2.82	2.88	3.04
Max Temperature (°C)	106.87	120.69	108.13
Min Pressure (MPa)	1.31	0.44	1.02
Min Temperature (°C)	40	40	40
Superheat Degrees (°C)	31.96	1	18.72
ORC mass flow rate (kg/s)	107.1	73.0	75.9
Thermal Efficiency (%)	1.99	7.19	4.53

Table 3 Thermodynamic optimization results for the subcritical ORC plant with a recuperator

Parameter	R115	R236fa	R1234yf
Net Work (kW)	564.5	991.6	811.4
Pump Work (kW)	183.3	223.2	166.4
Fan Work (kW)	303.4	370.9	318.7
Max Pressure (MPa)	2.82	2.88	3.04
Max Temperature (°C)	122.29	120.69	121.6
Min Pressure (MPa)	1.31	0.44	1.02
Min Temperature (°C)	40	40	40
Superheat Degrees (°C)	47.39	1	32.20
ORC mass flow rate (kg/s)	97.6	73.0	65.7
Thermal Efficiency (%)	5.83	8.15	7.82

3.1.3 Supercritical ORC without recuperator (SPC)

Table 4 summarizes the optimal thermodynamic parameters for the SPC, for all the working fluids analyzed in this study. It can be seen that the fluid R236fa would extend its optimal performance to this case study, yielding a net power of around 906 kW; about 15 kW more than what obtains with R1234yf, and around 218 kW above the net power produced with R115. Similarly, the SPC with the working fluid R236fa yielded a thermal efficiency of about 7%, only around 0.1 Percentage points beyond what obtains with R1234yf, and about 1.5 percentage points more than R115. Furthermore, results showed that the use of a supercritical configuration would improve the performance of the ORC plant for all the working fluids. Specifically, comparing the results of SBC with those of SPC shows that the net power would increase by about 3.6% for R236fa, 46% for R1234yf, and 152% for R115. However, results showed that the thermal efficiency could be negatively impacted by using the supercritical configuration. Specifically, a lower thermal efficiency of 7.03% was recorded for the SPC with R236fa, relative to 7.19% with the SBC. The other working fluids showed increased thermal efficiency with a switch from SBC to SPC.

3.1.4 Supercritical ORC with recuperator (SPC-R)

The optimal thermodynamic performance parameters of the SPC-R are highlighted in Table 5, for all the working fluids assessed in this study. For this case study, the highest net power output of 1043 kW was obtained with R1234yf as the working fluid; about 12 kW more than what obtains with R236fa, and around 143 kW beyond that with R115. It is important to emphasize the observation here that the fluid R1234yf performed better in terms of net power production than R236fa which had hitherto yielded the highest net power in all the other ORC configurations. Additionally, the working fluid R115 was obtained with the highest thermal efficiency for the SPC-R, rated at about 9.5%; about 0.4 percentage points more than R1234yf and about 1.6 percentage points above R236fa. Furthermore, a comparative assessment of SPC and SPC-R reinforces the submission earlier that incorporating a recuperator would improve performance for all the working fluids considered. The same can be said for a switch from a subcritical ORC configuration to a supercritical one in terms of net power output with all the working fluids studied. It can however be observed that the fluid R236fa reduced the ORC thermal efficiency for the switch from the subcritical to the supercritical configuration, from 8.15% in SBC-R to 7.91% in SPC-R.

Table 4 Thermodynamic optimization results for the supercritical ORC plant without a recuperator

Parameter	R115	R236fa	R1234yf
Net Work (kW)	688.2	906.4	891.1
Pump Work (kW)	613.9	292.7	450.4
Fan Work (kW)	509.0	519.8	519.2
Max Pressure (MPa)	6.64	3.28	5.84
Max Temperature (°C)	146.72	126.85	136.85
Min Pressure (MPa)	1.31	0.44	1.02
Min Temperature (°C)	40	40	40
Superheat Degrees (°C)	66.77	1.93	42.15
ORC mass flow rate (kg/s)	92.19	82.36	74.68
Thermal Efficiency (%)	5.52	7.03	6.95

Table 5 Thermodynamic optimization results for the supercritical ORC plant with a recuperator

Parameter	R115	R236fa	R1234yf
Net Work (kW)	900.4	1,031.1	1,043.2
Pump Work (kW)	521.9	300.5	394.8
Fan Work (kW)	283.9	398.3	349.7
Max Pressure (MPa)	6.06	3.29	5.48
Max Temperature (°C)	147.44	126.85	136.85
Min Pressure (MPa)	1.31	4.37	1.02
Min Temperature (°C)	40	40	40
Superheat Degrees (°C)	67.49	1.93	42.15
ORC mass flow rate (kg/s)	88.0	84.3	70.8
Thermal Efficiency (%)	9.47	7.91	9.03

3.2 Sensitivity of the optimal ORC performance to waste heat temperatures

This section reports the sensitivities of the optimized power output and conversion efficiency for the various ORC schemes and working fluids considered in the study. These sensitivities are shown illustrated in Fig. 2 for the SBC utilizing geothermal energy from an abandoned oil well. As can be seen, lowering the condensation pressure favors both the net power produced and the thermal efficiency linearly for all the working fluids considered. Also, the order of performance of the working fluids is preserved throughout the range of condensation temperatures investigated; R236fa>R1234yf>R115 for both the net power output and the thermal efficiency. It can however be seen also that the margins between the net power produced between the fluid R236fa and R1234yf close up narrowly with decreasing condensation temperature, while that between R1234yf and R115 widens very slightly at lower condensation temperatures. The implication is that adopting a lower condensation temperature would be slightly more favorable with some working fluids (R1234yf) than others.

The sensitivity analysis results for the SBC-R are plotted in Fig. 3, showing some sorts of correlations with what obtains with the SBC, but with slight distinctions. The distinctions are more pronounced with the variations in thermal efficiency; the fluid R115 closes up drastically with R1234yf and R236fa as the condensation temperature drops. For instance, while the thermal efficiency of R1234yf exceeds that of R115 by about 5.6 percentage points at a condensation temperature of 50 °C, it has reduced to only about 0.4 percentage points at 30 °C. The reverse is the case between R236fa and R1234yf; the margin of the improved thermal efficiency recorded with R236fa reduces as the condensation temperature increase, both generating power at almost the same thermal efficiency at 50 °C

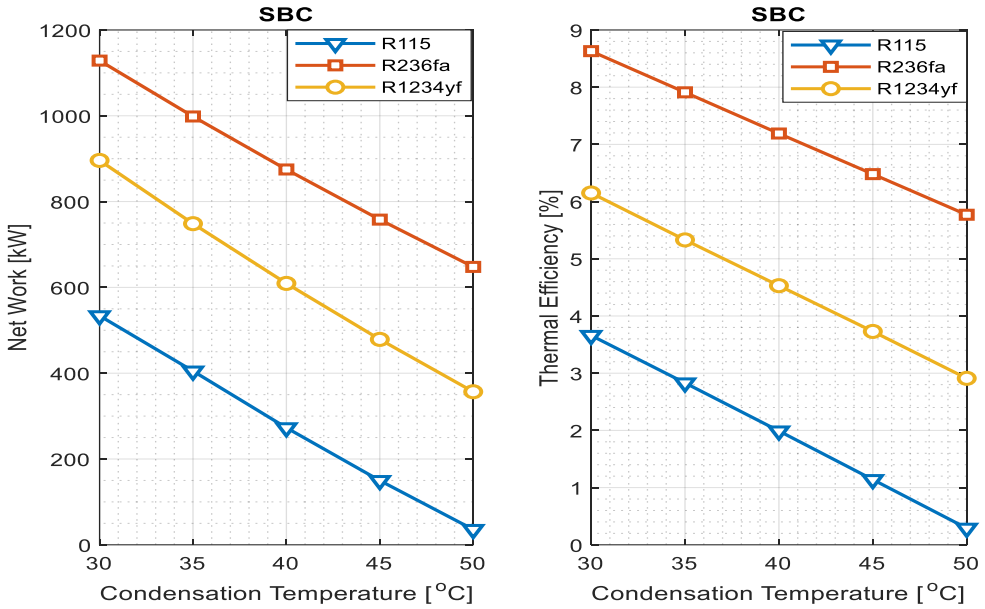

***Fig. 2**. Sensitivities of net power and thermal efficiency to the condensation temperature for the subcritical ORC without a recuperator*

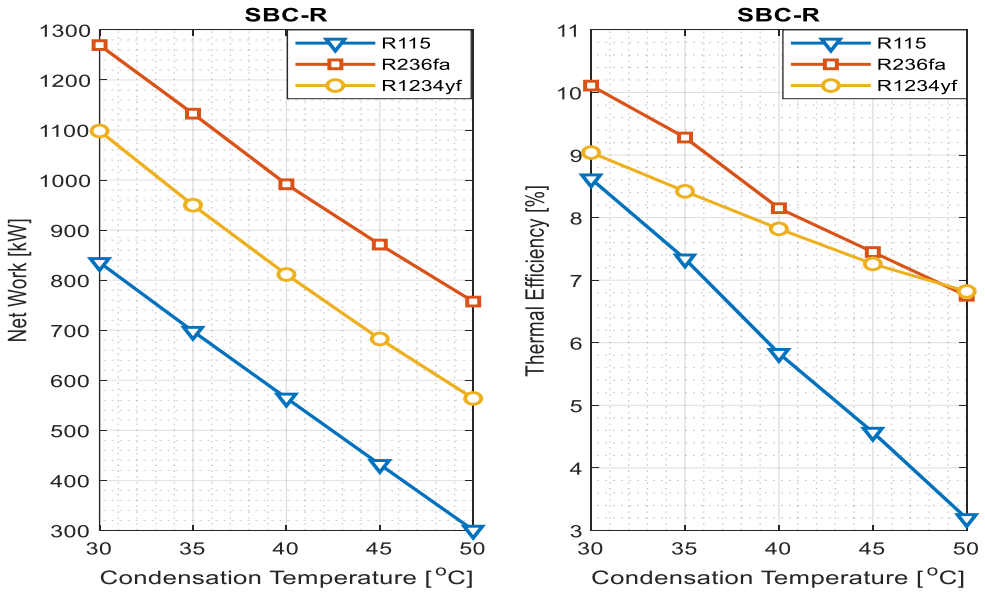

***Fig. 3.** Sensitivities of net power and thermal efficiency to the condensation temperature for the subcritical ORC with a recuperato*

Furthermore, the variations of the net power and thermal efficiency with condensation temperature are shown in Fig. 4 for the SPC. It should be reiterated here that a switch to the supercritical ORC configuration not only improves net power for all the fluids considered; the fluid R1234yf exhibited a closely matched performance with R236fa, with only very slight margins for both the net power and thermal efficiency. The fluid R1234yf produces net power increasingly lower than R236fa with decreasing condensation temperature but at a closer thermal efficiency. The two fluids produced power at about the same thermal efficiency at 30 ^{o}C.

Finally, the variations of net power and thermal efficiency are illustrated in Fig. 5 for the SPC-R, for all the working fluids considered. It is worth noting here again that the two fluids R236fa and R1234yf produced almost the same net power at lower condensation temperatures, say between 30 ^{o}C and 38 ^{o}C. Even at higher condensation temperatures up to 50^{o}C, the difference in net power produced by the two fluids is only marginal. However, the conversion thermal efficiency of the ORC is observed much lower with the fluid R236fa for all the range of condensation temperatures examined, contrary to what obtains with the other ORC configurations discussed earlier. The fluid R115 showed much better conversion efficiency throughout the condensation temperatures examined for the SPC-R, contrary to what would be expected. It thus shows that the performance of working fluids clearly

differs for different ORC configurations, and an optimal selection should only be made after thorough computations.

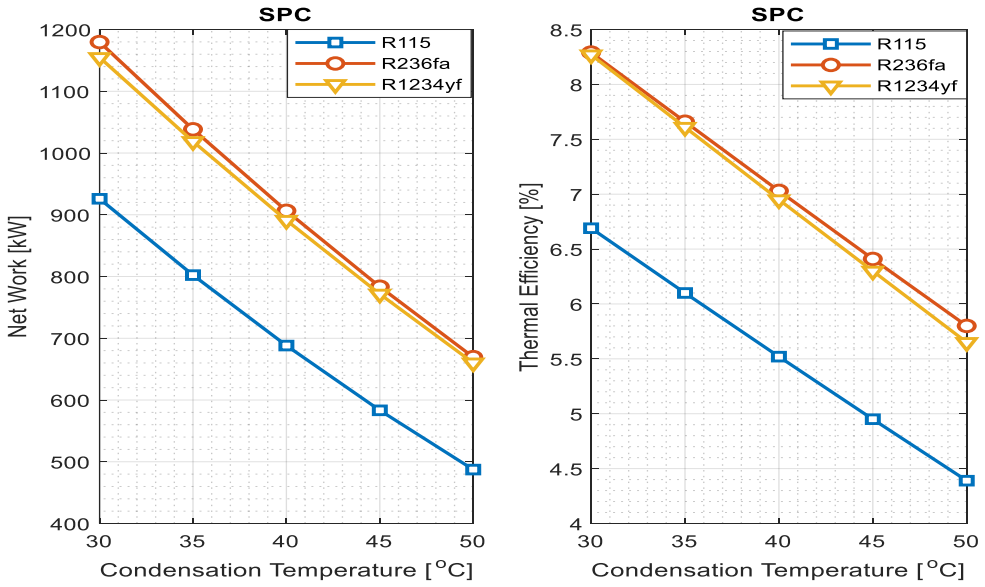

Fig. 4*. Sensitivities of net power and thermal efficiency to the condensation temperature for the supercritical ORC without a recuperator.*

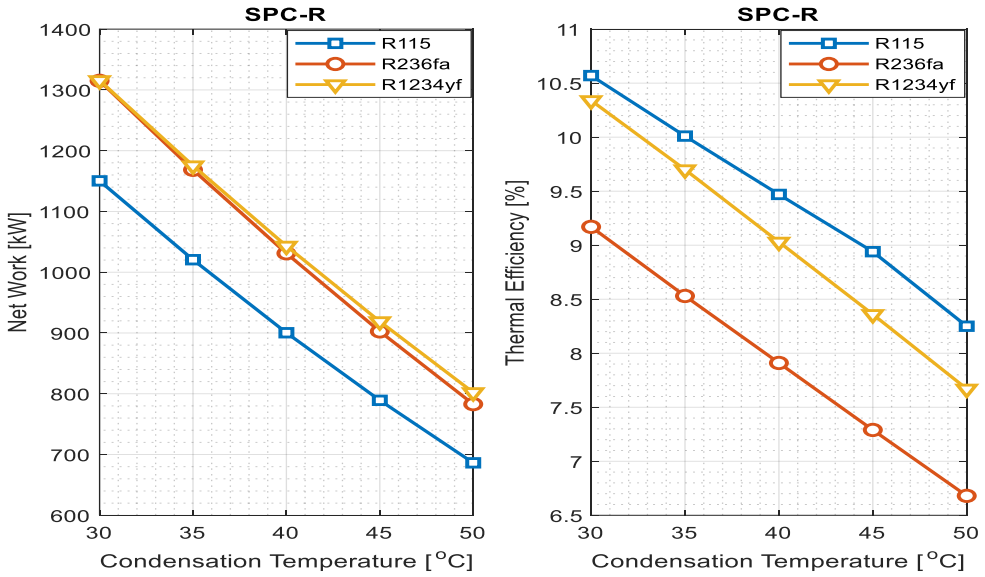

Fig. 5 - *Sensitivities of net power and thermal efficiency to the condensation temperature for the supercritical ORC with recuperator.*

4. Conclusions

Optimal geothermal power producible from an abandoned oil well in Nigeria has been compared in this study for different ORC configurations and working fluids. Four ORC configurations were assessed, designated as subcritical without a regenerator (SBC), subcritical with a regenerator (SBC-R), supercritical without a regenerator (SPC), and supercritical with a regenerator (SPC-R). The geological characteristics of an abandoned oil well in the Niger Delta region of Nigeria were employed to numerically simulate the ORC heat source parameters. Additionally, zero-dimensional ORC design and optimization models were implemented in MATLAB to satisfy the mass and energy balance equations defined by the First Law of Thermodynamics. This study is the first attempt at the technical quantification of electrical power production from an oil well in Nigeria, to the authors' best knowledge. Additionally, previous studies on this subject haven't given adequate consideration to the effects of design configurations and working fluids on ORC performance for the exploitation of geothermal energy from abandoned oil wells, which further highlights the contribution to knowledge intended by this study. The main results obtained from the study are:

- The most basic ORC configuration employed can produce between 272 kW and 875 kW of electrical power; about 273 kW with the working fluid R115, about 609 kW with R1234yf, and about 875 kW with R236fa;

- The introduction of a recuperator would increase ORC performance for all working fluids. For instance, a switch from the SBC to the SBC-R would increase net power by around 13% for R236fa, 33% for R1234yf, and 107% for R115, while thermal efficiency would increase by about 1 percentage point for R236fa, 3.3 percentage points for R1234yf, and 3.8 percentage points for R115;
- The use of a supercritical ORC configuration would increase net power irrespective of the choice of the working fluid. Specifically, results showed that a switch from the SBC to the SPC would increase the net power by about 3.6% for R236fa, 46% for R1234yf, and 152% for R115;
- Decreasing the condensation pressure would result in a linear increase in both the net power and thermal efficiency for all the working fluids. Also, the order of the performance of the working fluids is preserved throughout the range of condensation temperatures investigated; R236fa>R1234yf>R115 for both the net power output and the thermal efficiency.

Future studies should give attention to improvement opportunities available in each of the ORC components for the different cycle configurations, using the technical and economic methods defined by the Second Law of Thermodynamics.

Author Contribution

Data curation – Joseph Oyekale (JO); Formal analysis - JO; investigation – Oluwaseun Adetona (OA); Experimental Performance - JO; Data Collection - OA; Processing – JO and OA; Literature review - JO; Writing - JO; review and editing - OA.

Declaration of Competing Interest

The authors declared no conflicts of interest with respect to the research, authorship, and/or publication of this article.

Acknowledgements

This study received no funding. The authors appreciate the reviewers and editors for their contributions to the body of knowledge by allowing researchers like us publish our work

References

[1] He, Y., Wang, S., & Lai, K. K. (2010). Global economic activity and crude oil prices: A cointegration analysis. *Energy Economics*, *32*(4), 868–876. https://doi.org/10.1016/j.eneco.2009.12.005

[2] Lukawski, M. Z., Anderson, B. J., Augustine, C., Capuano, L. E., Beckers, K. F., Livesay, B., & Tester, J. W. (2014). Cost analysis of oil, gas, and geothermal well drilling. *Journal of Petroleum Science and Engineering*, *118*, 1–14. https://doi.org/10.1016/j.petrol.2014.03.012

[3] Owen, N. A., Inderwildi, O. R., & King, D. A. (2010). The status of conventional world oil reserves-Hype or cause for concern? *Energy Policy*, *38*(8), 4743–4749. https://doi.org/10.1016/j.enpol.2010.02.026

[4] Burdon, D., Barnard, S., Boyes, S. J., & Elliott, M. (2018). Oil and gas infrastructure decommissioning in marine protected areas: System complexity, analysis and challenges. *Marine Pollution Bulletin*, *135*(February), 739–758. https://doi.org/10.1016/j.marpolbul.2018.07.077

[5] Raimi, D., Krupnick, A. J., Shah, J.-S., & Thompson, A. (2021). Decommissioning Orphaned and Abandoned Oil and Gas Wells: New Estimates and Cost Drivers. *Environmental Science & Technology*, *55*(15), 10224–10230. https://doi.org/10.1021/acs.est.1c02234

[6] Alboiu, V., & Walker, T. R. (2019). Pollution, management, and mitigation of idle and orphaned oil and gas wells in Alberta, Canada. *Environmental Monitoring and Assessment*, *191*(10). https://doi.org/10.1007/s10661-019-7780-x

[7] D'Alesio, P., Caramanico, L., Angelucci, E., Scalzitti, L., Jamot, N., & Sorhabil, J. (2019, March 27). Well Ageing Studies for the Safe Extension of Wells Life. *Offshore Mediterranean Conference and Exhibition*.

[8] D'Alesio, P., Caramanico, L., Angelucci, E., & Scalzitti, L. (2019, October 13). Wells Life Extension Through a Risk-Based Well Ageing Study. *SPE Kuwait Oil & Gas Show and Conference*. https://doi.org/10.2118/198162-MS

[9] Nezamian, A., & Altmann, J. (2013, June 9). An Oil Field Structural Integrity Assessment for Re-Qualification and Life Extension. https://doi.org/10.1115/OMAE2013-10968

[10] Nian, Y. Le, & Cheng, W. L. (2018). Insights into geothermal utilization of abandoned oil and gas wells. *Renewable and Sustainable Energy Reviews*, *87*(November 2017), 44–60. https://doi.org/10.1016/j.rser.2018.02.004

[11] Liu, X., Falcone, G., & Alimonti, C. (2018). A systematic study of harnessing low-temperature geothermal energy from oil and gas reservoirs. *Energy*, *142*, 346–355. https://doi.org/10.1016/j.energy.2017.10.058

[12] Chmielowska, A., Tomaszewska, B., & Sowizdza, A. (2020). The Utilization of Abandoned Petroleum Wells in Geothermal Energy Sector. Worldwide Trends and Experience. *E3S Web of Conferences*, *154*. https://doi.org/10.1051/e3sconf/202015405004

[13] Duggal, R., Rayudu, R., Hinkley, J., Burnell, J., & Ward, S. (2021). Identifying issues in geothermal energy production from petroleum fields. *IEEE Region 10 Annual International Conference, Proceedings/TENCON*, *2021-Decem*, 254–259. https://doi.org/10.1109/TENCON54134.2021.9707342

[14] Oyekale, J., & Emagbetere, E. (2022). 19 - Pragmatic steps to the revitalization of abandoned oil and gas wells for geothermal applications. In Y. Noorollahi, M. N. Naseer, & M. M. B. T.-U. of T. P. of A. W. Siddiqi (Eds.), (pp. 389–403). Academic Press. https://doi.org/https://doi.org/10.1016/B978-0-323-90616-6.00019-1

[15] Kaplanoğlu, M. A., Baba, A., & Gokcen Akkurt, G. (2020). Use of abandoned oil wells in geothermal systems in Turkey. *Geomechanics and Geophysics for Geo-Energy and Geo-Resources*, *6*(1). https://doi.org/10.1007/s40948-019-00125-0

[16] Gong, B., Liang, H., Xin, S., & Li, K. (2011). Effect of Water Injection on Reservoir Temperature During Power Generation in Oil Fields. In *Thirty-sixth Workshop on*

Geothermal Reservoir Engineering Stanford University. Stanford, California.

[17] Mehmood, A., Yao, J., Fan, D., Bongole, K., Liu, J., & Zhang, X. (2019). Potential for heat production by retrofitting abandoned gas wells into geothermal wells. *PLoS ONE*, *14*(8), 1–19. https://doi.org/10.1371/journal.pone.0220128

[18] Naseer, M. N., Noorollahi, Y., Zaidi, A. A., Wahab, Y. A., Johan, M. R., & Badruddin, I. A. (2022). Abandoned wells multigeneration system: promising zero CO2 emission geothermal energy system. *International Journal of Energy and Environmental Engineering*, (0123456789). https://doi.org/10.1007/s40095-022-00496-3

[19] Gharibi, S., Mortezazadeh, E., Jalaledin, S., Aghcheh, H., & Vatani, A. (2018). Feasibility study of geothermal heat extraction from abandoned oil wells using a U-tube heat exchanger. *Energy*, *153*, 554–567. https://doi.org/10.1016/j.energy.2018.04.003

[20] Wight, N. M., & Bennett, N. S. (2015). Geothermal energy from abandoned oil and gas wells using water in combination with a closed wellbore. *Applied Thermal Engineering*, *89*, 908–915. https://doi.org/10.1016/j.applthermaleng.2015.06.030

[21] Milliken, M. (2007). Geothermal resources at naval petroleum Reserve-3 (NPR-3), Wyoming. *Thirty-Second Workshop on Geothermal Reservoir Engineering Stanford University, Stanford, California, January 22-24, 2007 SGP-TR-183*, *3*(Figure 1), 9.

[22] Sanyal, S. K., & Butler, S. J. (2010). Geothermal Power Capacity from Petroleum Wells – Some Case Histories of Assessment. *World Geothermal Congress*, (April), 25–29.

[23] Harris, B. E., Lightstone, M. F., & Reitsma, S. (2021). A numerical investigation into the use of directionally drilled wells for the extraction of geothermal energy from abandoned oil and gas wells. *Geothermics*, *90*(November 2020), 101994. https://doi.org/10.1016/j.geothermics.2020.101994

[24] Noorollahi, Y., Pourarshad, M., Jalilinasrabady, S., & Yousefi, H. (2015). Numerical simulation of power production from abandoned oil wells in Ahwaz oil field in southern Iran. *Geothermics*, *55*, 16–23. https://doi.org/10.1016/j.geothermics.2015.01.008

[25] Patihk, J., Warner-Lall, D., Alexander, D., Maharaj, R., & Boodlal, D. (2022). The optimization of a potential geothermal reservoir using abandoned wells: a case study for the forest reserve field in Trinidad. *Journal of Petroleum Exploration and Production Technology*, *12*(1), 239–255. https://doi.org/10.1007/s13202-021-01322-y

[26] Singh, H. K. (2020). Geothermal energy potential of Indian oilfields. *Geomechanics and Geophysics for Geo-Energy and Geo-Resources*, *6*(1), 1–9. https://doi.org/10.1007/s40948-020-00148-y

[27] Akinyetun, T. (2016). Nigeria and Oil Production : Lessons for Future. *International Journal of Multidisciplinary Research and Development*, *3*(5), 19–24.

[28] Hu, X., Banks, J., Wu, L., & Victor, W. (2020). Numerical modeling of a coaxial borehole heat exchanger to exploit geothermal energy from abandoned petroleum wells in Hinton , Alberta. *Renewable Energy*, *148*, 1110–1123. https://doi.org/10.1016/j.renene.2019.09.141

[29] Idialu, P., Ainodion, J., & Alabi, L. (2004, March 29). Restoration and Remediation of Abandoned Petroleum Drill Sites - A Nigerian Case Study. *SPE International Conference on Health, Safety, and Environment in Oil and Gas Exploration and Production*. https://doi.org/10.2118/86796-MS

[30] García-Pabón, J. J., Méndez-Méndez, D., Belman-Flores, J. M., Barroso-Maldonado, J. M., & Khosravi, A. (2021). A review of recent research on the use of r1234yf as an environmentally friendly fluid in the organic rankine cycle. *Sustainability (Switzerland)*, *13*(11). https://doi.org/10.3390/su13115864

[31] Lazzaretto, A., & Manente, G. (2014). A new criterion to optimize ORC design performance using efficiency correlations for axial and radial turbines. *International Journal of Thermodynamics*, *17*(3), 173–181. https://doi.org/10.5541/ijot.562

[32] Borsukiewicz-gozdur, A., & Nowak, W. (2010). Geothermal Power Station with Supercritical Organic Cycle Principles of operations of a power. *World Geothermal Congress*, (April), 25–29.

European Journal of Engineering and Applied Sciences

ISSN: 2651-3412 (Print) & 2667-8454 (Online)
Journal homepage: http://dergipark.gov.tr/EJEAS
Published by Çorlu Faculty of Engineering, Tekirdağ Namık Kemal University

European J. Eng. App. Sci. 6(1), 19-24, 2023

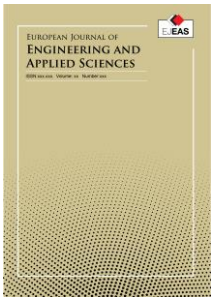

Research Article

Ampacity Decrease in a Three-phase Power Cable Fed by an Uncontrolled Rectifier and Finding a Lower Limit for the Power Cable Loss

Hakan Çanta [1], Reşat Mutlu [2]

[1]Unika Cable, Çerkezköy, Türkiye, 59500
[2]Electronics and Communication Engineering Department, Çorlu Engineering Faculty, Tekirdağ Namık Kemal University, Tekirdağ, Türkiye, 59850
[1] hakan@unika.com.tr, *[2]rmutlu@nku.edu.tr

Received: 23.06.2023 *Accepted: 25.07.2023* *DOI: 10.55581/ejeas.1293146*

***Abstract*—**Rectifiers are the most common nonlinear loads encountered in electrical power systems. Uncontrolled rectifiers are cheaper than synchronous rectifiers and more common than them because of this but the currents drawn by uncontrolled rectifiers contain harmonics. In addition, the amplitude of these harmonics depends on the value of the load power and the rectifier parameters. A 3-phase cable can be used to connect a three-phase rectifier to a 3-phase power system. In this study, the power losses of a 3-phase cable fed by a synchronous rectifier and an uncontrolled rectifier were compared. The electrical equivalent of a power cable is frequency dependent. The analysis performed in this study was made by making some assumptions about the frequency-dependent resistance of the cable and the rectifier currents. The analysis shows that when an uncontrolled rectifier is fed by a power cable, the cable always has more loss and heats up more for the same amount of RMS current.

Keywords*—Cable Modeling, Loss Calculation, Harmonic Analysis, Circuit Analysis, Rectifiers.*

Kontrolsüz Bir Redresörle Beslenen Üç Fazlı Bir Güç Kablosunda Amper Kapasitesinin Azalması ve Güç Kablosu Güç Kaybının Alt Değerinin Bulunması

Öz. Doğrultucular elektrik güç sistemlerinde en yaygın karşılaşılan nonlineer yüklerdir. Kontrolsüz doğrultucular senkron doğrultuculara göre daha ucuzdur ve bundan dolayı daha yaygındır ama kontrolsüz doğrultucuların çektikleri akımlar harmonik içermektedir. Ayrıca bu çekilen harmoniklerin genliği yükün gücünün değerine ve doğrultucu parametrelerine bağlıdır. Üç fazlı bir doğrultucuyu üç fazlı güç sistemine bağlamak için üç fazlı bir kablo kullanılabilir. Bu çalışmada senkron bir doğrultucu ve kontrolsüz bir doğrultucu tarafından beslenen üç fazlı bir kablodaki kayıplar karşılaştırılmıştır. Bir kablonun elektriksel eşdeğeri frekansa bağımlıdır. Bu çalışmada yapılan analiz kablonun frekansa bağımlı direnci ve doğrultucu akımları üzerine bazı kabuller yapılarak bulunmuştur. Yapılan analiz kontrolsüz doğrultucu kullanıldığında 3 fazlı kablonun her zaman daha fazla kayba sahip olduğunu ve daha fazla ısınacağını göstermektedir.

***Anahtar Kelimeler*—** *Kablo Modelleme, Kayıp Hesabı, Harmonik Analizi, Devre Analizi, Doğrultucular.*

* Corresponding author
E-mail: rmutlu@nku.edu.tr (R. Mutlu)

1. Introduction

Electrical resistance is a function of frequency [1]. Skin-depth results in extra power loss in a cable excited with AC currents [2, 3]. Three-phase cables are complex systems to model [4]. Such transmission line models can also be made with fractional-order circuit elements [5]. This results in higher attenuation in high frequencies [3, 5, 6]. Such a frequency modeling of the cables may require machine learning [6]. The effects of harmonics on underground power cables are examined by considering a real system and using experimental data and shown to result in an excessive temperature rise due to the power losses in the cable [7]. Aging processes such as water treeing, electrical treeing, and dielectric breakdown can be observed in polymeric insulators of cables [8] and the high-temperature operation of cables also contributes to their early aging [9-11]. Cable failures and degradations that may occur directly or indirectly in the cable due to harmonics should be prevented [11, 12]. Skin and proximity effects in the cable impedance are difficult to model [13]. Their accurate modeling is also important in motor drive applications [14]. Three-phase power cables are often used to feed power rectifiers in industry. An experimental model of such a rectifier can be found in [15]. Uncontrolled rectifiers are nonlinear circuits, which lack exact analytical solutions [16] and are hard to model. That's why simplified models are often used in their analysis [17]. Some rectifiers use A frequency domain model for uncontrolled rectifiers as presented in [18]. A rectifier model for active loads is given in [19]. Averaging can also be used to model uncontrolled rectifiers [20]. A matrix solution for their modeling is presented in the frequency domain in [21]. An equivalent circuit for a diode bridge that makes use of AC and DC side rectifier harmonics is given in [22]. The uncontrolled rectifiers draw non-sinusoidal currents and their current profile varies by the load power [16-22] and this can cause overheating in the power cables. In this study, a lower bound for the power loss of a three-phase power cable feeding a three-phase uncontrolled rectifier is given to find out whether the loss stays the same for the same amount of transferred power to the load and whether the loss stays within the standards such as the international electrotechnical commission IEC 60287 standard [12].

The paper is arranged as follows. In the second section, the simplified models of an uncontrolled rectifier and a synchronous rectifier are given. In the third section, a lower value of the loss of power cable for an uncontrolled rectifier is given. The paper is finished with the conclusion section.

2. The Synchronous Rectifier and Uncontrolled Rectifier Models

A three-phase synchronous rectifier is a power electronic circuit, which uses the three-phase H-bridge inverter topology shown in Figure 1.a. Such rectifiers make use of sophisticated switching control strategies to withdraw almost sinusoidal currents from a three-phase utility with almost a power factor of one [23-26]. Since the harmonics around switching frequencies have very low magnitudes [27], their phase currents can be expressed as

$$i_a(t) = I_m sin(\omega t) \quad (1)$$

$$i_b(t) = I_m sin(\omega t - 2\pi/3) \quad (2)$$

$$i_c(t) = I_m cos(\omega t - 4\pi/3) \quad (3)$$

where I_m is the maximum value of the phase currents and ω is angular frequency.

The three-phase phase voltages can be written as

$$v_a(t) = V_m sin(\omega t) \quad (4)$$

$$v_b(t) = V_m sin(\omega t - 2\pi/3) \quad (5)$$

$$v_c(t) = V_m sin(\omega t - 4\pi/3) \quad (6)$$

where V_m is the maximum value of the phase voltages.

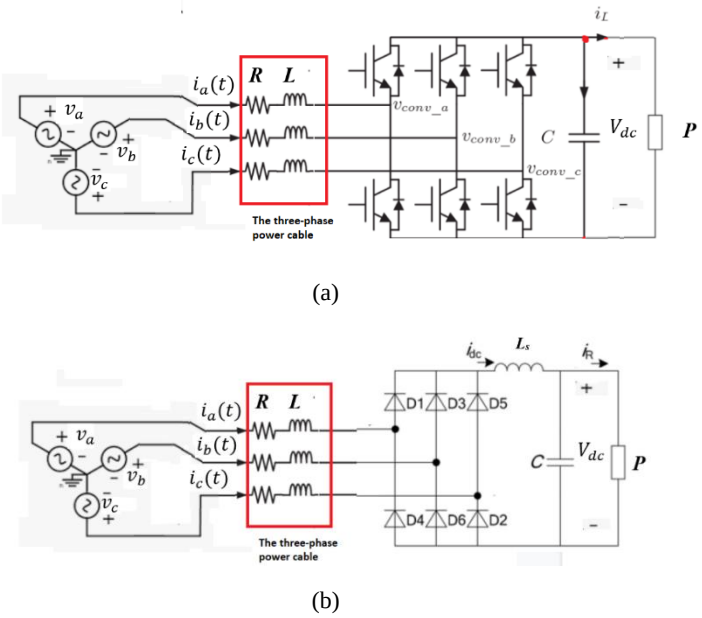

Fig. 1. *a) A three-phase synchronous rectifier circuit, and b) A three-phase uncontrolled rectifier circuit.*

An uncontrolled Hs-bridge rectifier is shown in Figure 1.b. It consists of six diodes. It has a DC bus inductor or a smoothing inductor (***L_s***) at the DC side. The inductor and the capacitor across the load behave as an *L-C* filter. It does not have any smoothing inductors at the AC inputs. Such a rectifier circuit draws non-sinusoidal currents and their current varies with respect to the load power [16-22].

A DC bus smoothing inductor is commonly used for filtering the AC ripple in the DC bus current. If its inductance value is high enough, the DC bus current at a high load can be assumed to be constant [28]. Due to the symmetric nature of the three-phase H-bridge rectifier and having an almost constant DC bus current, a phase current pulse is drawn from 120 degrees in both of the half-periods and there are also 30 degrees wide dead zones for symmetrically drawn pulses. Such a phase current can be expressed with Eq. (7) by ignoring the very little cable inductance. If there were a smoothing inductor used on each line to smoothen the phase currents the rectifier draws, a tapered phase current expression that takes the commutation of phases into account should have been used. Since the inductances

of the cables are quite less than that of such AC side smoothing inductors, Eq. (7) is sufficient to describe the phase current A.

At the maximum power with a smoothing inductor (L_s), whose inductance is sufficiently high, its Phase A current can be assumed to be of the form shown in Figure 2 and expressed as the following partial function:

$$i_a(t) = \begin{cases} 0, & 0 \le t < \frac{T}{12} \\ I_{dc}, & \frac{T}{12} \le t \le \frac{5T}{12} \\ 0, & \frac{5T}{12} < t < \frac{7T}{12} \\ -I_{dc}, & \frac{7T}{12} \le t \le \frac{11T}{12} \\ 0, & \frac{11T}{12} < t \le < T \end{cases} \quad (7)$$

where I_{dc} is the DC bus inductor current and $T = 2\pi/\omega$ is the electrical period.

The other phase currents are shifted by 120 degrees but they have also the same rms value:

$$i_b(t) = i_a(t - T/3) \quad (8)$$

$$i_c(t) = i_a\left(t - \frac{2T}{3}\right) = i_b\left(t - \frac{T}{3}\right) \quad (9)$$

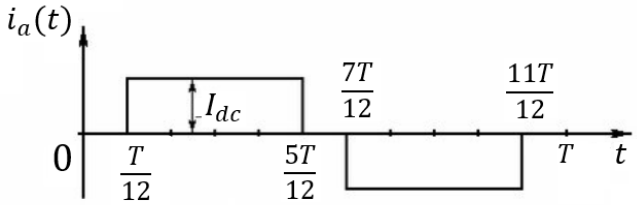

Fig. 2. *Phase A current of the uncontrolled rectifier.*

The DC bus inductor current can be assumed as

$$I_{dc} = \frac{P}{V_{dc}} \quad (10)$$

where P is the load power and V_{dc} is the DC bus voltage.

The DC bus voltage of the uncontrolled rectifier is approximately given as

$$V_{dc} = \frac{3\sqrt{3}V_m}{\pi} = \frac{3\sqrt{6}V_{rms}}{\pi} \quad (11)$$

The DC voltage of an uncontrolled three-phase H-Bridge rectifier can be around and less than the peak value of the line-to-line voltages, which is equal to 537 (380*sqrt(3)) Volt in Europe. Eq. (11) gives a value of 514 Volt, which is a little less than this value.

If the rectifier is loaded with the nominal power, the DC bus inductor current can be written as

$$I_{dc} = \frac{P_{nom}}{V_{dc}} \quad (12)$$

The rectifier circuit currents at low load power are hard to predict and simulations can be used for this purpose that will be studied in the future.

3. The Estimation of the Cable Power Losses for the Two Cases

A three-phase power cable topology is shown in Figure 3. It has copper wires as power conductors, an aluminum shield, and PVE used as insulation material. The losses of the power cables for the rectifiers are to be calculated in this section.

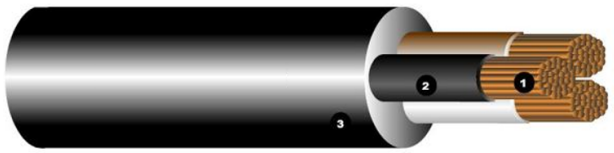

Fig. 3. *A three-phase power cable topology (Courtesy of Unika Cable).*

3.1. The Power Loss of a Three-Phase Cable under Sinusoidal Excitation or Fed by a Synchronous Rectifier

The nominal power which can be transferred through the power cable is given as

$$P_{nom} = 3V_{rms}I_{rms} = 3V_mI_m/2 \quad (13)$$

where I_{rms} is the rated rms phase current, and V_{rms} is the rated rms phase voltage.

The rms current of the power cable for Phase A is calculated as

$$I_{rms} = \sqrt{\frac{1}{T}\int_0^T (i_a(t))^2 dt} \quad (14)$$

For a sinusoidal current given in Eq. (1), the rms current is

$$I_{rms} = \frac{I_m}{\sqrt{2}} \quad (15)$$

Thus, the nominal transferred power by the power cable can also be given as

$$P_{nom} = 3V_{rms}I_{rms} \quad (16)$$

Since the phase currents of a synchronous rectifier are assumed to be sinusoidal, the power loss of the cable feeding the synchronous rectifier can be calculated as

$$P_{loss1} = 3R_{AC}I_{rms}^2 \quad (17)$$

where R_{AC} is the AC resistance of the cable at the utility frequency, $f = 1/T$.

The AC resistance of a three-phase cable [12] can be given as

$$R_{AC} = R_{DC}(1 + ys + yp) \tag{18}$$

where R_{DC} is the DC resistance of the cable, ys is the skin effect factor, and *yp* is the proximity effect factor.

More about the AC resistance of a cable can be found in [29].

Using the transferred power,

$$P_{loss1} = 3R_{AC}\left(\frac{P_{nom}}{3V_{rms}}\right)^2 = \frac{R_{AC}P_{nom}^2}{3V_{rms}^2} = \frac{0.333R_{AC}P_{nom}^2}{3V_{rms}^2} \tag{19}$$

The rectifier circuit currents at low load power are hard to predict and simulations can be used for this purpose that will be studied in the future.

3.2 The Lower Bound of Power Loss of the Three-Phase Cable Fed by an Uncontrolled Rectifier

The uncontrolled rectifier is assumed to be drawing a current with harmonics from Phase A as seen in Figure 2. The other phase currents are shifted by 120 and 240 degrees with respect to the current of Phase A. The power loss of a cable is frequency dependent due to the skin and proximity effects:

$$P_{loss2} = 3\sum_{k=1}^{\infty}\frac{R_k I_k^2}{2} \geq 3\sum_{k=1}^{\infty}\frac{R_{AC} I_k^2}{2} = 3R_{AC}\sum_{k=1}^{\infty}\frac{I_k^2}{2} \tag{20}$$

where P_{loss2} is the power loss of the three-phase cable feeding the uncontrolled rectifier and R_k=*R*(*kf*) is the phase resistance of the three-phase cable at the k^{th} harmonic.

R_k is an increasing function of frequency. The cable resistance at the fundamental frequency (R_{AC} or R_1) is less than that at the k^{th} harmonic frequency ($k \geq 2$) and the following is always true,

$$R_k \geq R_{AC} = R_1 \tag{21}$$

Therefore, a lower bound for the power loss can be found as

$$P_{loss} = 3\sum_{k=1}^{\infty}\frac{R_k I_k^2}{2} \geq 3\sum_{k=1}^{\infty}\frac{R_{AC} I_k^2}{2} = 3R_{AC}\sum_{k=1}^{\infty}\frac{I_k^2}{2} \tag{22}$$

Using Parseval's identity,

$$I_{rms}^2 = \sum_{k=1}^{\infty}\frac{I_k^2}{2} = \frac{1}{T}\int_0^T (i_a(t))^2 dt \tag{23}$$

Using Eq. (7), the lower bound for the cable power loss can be calculated as:

$$P_{lossmin} = 3R_{AC}I_{rms}^2 == \frac{3R_{AC}}{T}\int_0^T (i_a(t))^2 dt = \frac{3R_{AC}}{T}\frac{2T}{3}I_{dc}^2$$

$$P_{lossmin} = 2R_{AC}I_{dc}^2 = 2R_{AC}\left(\frac{P_{nom}}{V_{dc}}\right)^2 \tag{25}$$

$$P_{lossmin} = 2R_{AC}\left(\frac{P_{nom}}{\frac{3\sqrt{3}V_{rms}}{\pi}}\right)^2 = \frac{2\pi^2 R_{AC}}{27}\left(\frac{P_{nom}}{V_{rms}}\right)^2 \tag{26}$$

The lower bound of the power loss of the cable feeding the uncontrolled rectifier is found as:

$$P_{lossmin} = 0.731R_{AC}\left(\frac{P_{nom}}{V_{rms}}\right)^2 \tag{27}$$

Therefore, the following expression is always true:

$$P_{loss} > P_{lossmin} \tag{28}$$

Therefore, considering both of the cases examined, for the same value of the rms voltage, the following is always true:

$$P_{loss2} > P_{lossmin} > P_{loss1} \tag{29}$$

The power loss of the cable feeding the uncontrolled rectifier is always higher than that of a synchronous rectifier.

Ampacity is a made-up word for ampere capacity (current-carrying capacity) defined by National Electrical Codes [30], in some North American countries. Ampacity is defined as the maximum current, in amperes, that a conductor can carry continuously under the conditions of use without exceeding its temperature rating.

$$\frac{P_{loss2}}{P_{loss1}} > \frac{P_{lossmin}}{P_{loss1}} = 2.195 \tag{30}$$

This means to prevent overheating of the three-phase cable and not to decrease its life, the cable should be operated a lower current or transfer a lower power.

4. Conclusions

In this study, the losses occurring in a three-phase power cable feeding a synchronous and an uncontrolled rectifier have been examined. It is assumed that the rectifier has a DC side smoothing inductor and draws a square wave current with zero intervals. A lower bound value for the cable power loss feeding the uncontrolled rectifier is given. Considering (9) and (23), the power loss of the cable feeding the uncontrolled rectifier is at least 119.5% higher than that of the synchronous rectifier case. If the skin effect model of the cable is taken into account, the power loss of the cable feeding the uncontrolled rectifier would have been found to be higher. The finding here is of importance since it implies that the ampacity of the cable decreases, i.e., the cable overheats when the three-phase cable feeds an uncontrolled rectifier having non-sinusoidal currents for the same amount of the transferred power. This means that a

power cable should be operated to feed a lower transferred power in a steady state. Otherwise, its operation life would be less than the one given in its catalog. Also, considering that the uncontrolled rectifier load can be temporarily higher than the nominal power for a short amount of time, this would result in an even higher temperature in the cable and the worst impact on his life.

A more accurate analysis of such a 3-phase cable should be performed by taking into account the transfer function in the frequency domain of the cable and the harmonics of the current. As future work, to obtain a more accurate loss model, we suggest that the experimentally measured cable parameters and the complete circuit model of the uncontrolled rectifier must be used to estimate the power loss. More sophisticated cable models can be used for that purpose [31]. The current harmonics of the input currents of the uncontrolled rectifier can be obtained by simulations depending on the load power, and, then, the cable losses can be calculated using the harmonic magnitudes and experimentally found cable parameters such as the frequency-dependent electrical resistance.

Smoothing inductors at AC side of the uncontrolled rectifiers are commonly used in the factories for power quality improvement. Also, using a smoothing inductor for each side at the AC side of the uncontrolled rectifier may result in the less power cable loss since the phase currents can be smoothened. We also suggest this as future work.

Author Contribution

Formal analysis –Reşat Mutlu (RM); Investigation – RM; Hakan Çanta (HÇ), Processing – RM, HÇ; Literature review – RM, HÇ; Writing – RM, HÇ; Review and editing – RM, HÇ;

Declaration of Competing Interest

The authors declared no conflicts of interest with respect to the research, authorship, and/or publication of this article.

Acknowledgements

This study has been supported by the research and development center of Ünika Üniversal Kablo Sanayi ve Tic. A.Ş. Project number: UPN-2205.

References

[1] Lamb, H. (1883). XIII. On electrical motions in a spherical conductor. Philosophical Transactions of the Royal Society of London.174, 519–549.

[2] Beaty, H. W., & Fink, D. G. (2013). Standard handbook for electrical engineers. McGraw-Hill Education

[3] Johnson, H., Johnson, H. W., & Graham, M. (2003). High-Speed Signal propagation: Advanced Black Magic. Prentice Hall. pp. 58–78.

[4] Aloui, T., Amar, F. B., & Abdallah, H. H. (2011, March). Modeling of a three-phase underground power cable using the distributed parameters approach. In Eighth International Multi-Conference on Systems, Signals & Devices (pp. 1-6). IEEE.

[5] Limei Y., Yusong Z., Jianjun X., Weijian R., Qiong W., Zhigang S. (2014). Transmission lines modeling method based on fractional order calculus theory. Transactions of China Electrotechnical Society. 29(9), 260-268.

[6] Öztürk, P., Alisoy, H., & Mutlu, R. (2019). Yapay Sinir Ağları Kullanarak İkili ve Üçlü Büküm Makinaların Ürettiği CAT 6A U/FTP Kabloların Parametrelerinin Tahmini ve Tahmin Edilen Sonuçların Karşılaştırılması. European Journal of Engineering and Applied Sciences, 2(2), 41-51

[7] Sahin, Y. G., & Aras, F. (2007, April). Investigation of harmonic effects on underground power cables. In 2007 International Conference on Power Engineering, Energy and Electrical Drives (pp. 589-594). IEEE.

[8] Karhan, M., Çakır, M. F., & Uğur, M. (2021). A new approach to the analysis of water treeing using feature extraction of vented type water tree images. Journal of Electrical Engineering & Technology, 16, 1241-1252.

[9] Perka, B., & Piwowarski, K. (2021). A method for determining the impact of ambient temperature on an electrical cable during a fire. Energies, 14(21), 7260.

[10] Geng, P., Song, J., Tian, M., Lei, Z., & Du, Y. (2018). Influence of thermal aging on AC leakage current in XLPE insulation. Aip Advances, 8(2). 025115.

[11] Liu, Y., Wang, H., Zhang, H., & Du, B. (2022). Thermal Aging Evaluation of XLPE Power Cable by Using Multidimensional Characteristic Analysis of Leakage Current. Polymers, 14, 3147.

[12] IEC 60287-1-1 Electric cables-calculation of the current rating, part 1: current rating equations (100% load factor) and calculation of losses, section 1: general, 2006

[13] Chien, C. H., & Bucknall, R. W. (2009). Harmonic calculations of proximity effect on impedance characteristics in subsea power transmission cables. IEEE transactions on power delivery, 24(4), 2150-2158.

[14] Bolsens, B., De Brabandere, K., Van den Keybus, J., Driesen, J., & Belmans, R. (2003, June). Transmission line effects on motor feed cables: terminator design and analysis in the Laplace-domain. In IEEE International Electric Machines and Drives Conference, 2003. IEMDC'03. (Vol. 3, pp. 1866-1872). IEEE.

[15] Zhou, N., Wang, J., Wang, Q., & Wei, N. (2014). Measurement-based harmonic modeling of an electric vehicle charging station using a three-phase uncontrolled rectifier. IEEE Transactions on Smart Grid, 6(3), 1332-1340.

[16] Kassakian, J. G., Schlecht, M. F., Verghese, G. C. (1991). Principle of power electronics. Pearson College Div; Facsimile edition

[17] Herraiz, S., Sainz, L., Córcoles, F., & Pedra, J. (2005). A unified and simple model for uncontrolled rectifiers. Electric Power Systems Research, 74(3), 331–340.

[18] Chen, M., Qian, Z., Yuan, X., & Qiu, Z. (2006, June). A Frequency Domain Analytical Model of Uncontrolled Rectifiers. In 37th IEEE Power Electronics Specialists Conference (pp. 1-5).

[19] Rabinovici, R., Avital, M., & Dagan, K. J. (2012, November). An equivalent model for single and three phase power rectifiers with active loads. In 2012 IEEE 27th Convention of Electrical and Electronics Engineers in Israel (pp. 1-5). IEEE.

[20] Rahnama, M., Vahedi, A., Alikhani, A. M., Nahid-Mobarakeh, B., & Takorabet, N. (2019). Novel average value model for faulty three-phase diode rectifier bridges. Journal of Power Electronics, 19(1), 288-295.

[21] Sun, Y., Dai, C., Li, J., & Yong, J. (2016). Frequency-domain harmonic matrix model for three-phase diode-bridge rectifier. IET Generation, Transmission & Distribution, 10(7), 1605-1614.

[22] Unverdi, E., & Yildiz, A. B. (2013). Equivalent circuit model containing AC and DC side harmonics of rectifier circuits. In 4th International Conference on Power Engineering, Energy and Electrical Drives (pp. 582-586). IEEE.

[23] Torrey, D. A., & Al-Zamel, A. M. (1995). Single-phase active power filters for multiple nonlinear loads. IEEE Transactions on Power electronics, 10(3), 263-272.

[24] Saetieo, S., Devaraj, R., & Torrey, D. A. (1995). The design and implementation of a three-phase active power filter based on sliding mode control. IEEE transactions on Industry Applications, 31(5), 993-1000.

[25] Al-Zamil, A. M., & Torrey, D. A. (2001). A passive series, active shunt filter for high power applications. IEEE Transactions on Power Electronics, 16(1), 101-109.

[26] Tamyurek, B., & Torrey, D. A. (2010). A three-phase unity power factor single-stage AC–DC converter based on an interleaved flyback topology. IEEE transactions on Power Electronics, 26(1), 308-318.

[27] Mohan, N. (1993). A novel approach to minimize line-current harmonics in interfacing power electronics equipment with 3-phase utility systems. IEEE transactions on power delivery, 8(3), 1395-1401.

[28] Mohan, N., Undeland, T. M., & Robbins, W. P. (2003). Power electronics: converters, applications, and design. John Wiley & Sons.

[29] Riba, J. R. (2015). Analysis of formulas to calculate the AC resistance of different conductors' configurations. Electric Power Systems Research, 127, 93-100.

[30] Sergent, J. S., Coach, C. D., & Roux, R. J. (2011). National electrical code handbook. NFPA.

[31] El-Khatib, W. Z., Holbøll, J., Rasmussen, T. W., & Vogel, S. (2015). Comparison of cable models for time domain simulations. In 24th Proceedings of the Nordic Insulation Symposium (pp. 158-162).

European Journal of Engineering and Applied Sciences

ISSN: 2651-3412 (Print) & 2667-8454 (Online)
Journal homepage: http://dergipark.gov.tr/EJEAS
Published by Çorlu Faculty of Engineering, Tekirdağ Namık Kemal University

European J. Eng. App. Sci. 6(1), 25-31, 2023

Research Article

Comparison of Performance Analysis of CMOS-based VDCC and Differantial Amplifiers FGMOS-based VDCC Circuits and Its Filter Application

Büşra Hasılcı[1*], Fırat Kaçar[1]

[1] Department of Electrical and Electronics Engineering, Istanbul University-Cerrahpaşa, 34320 Istanbul, Turkey
[1]busra.hasilci@ogr.iuc.edu.tr, [2] fkacar@iuc.edu.tr

Received: 23.06.2023 Accepted: 25.07.2023 DOI: 10.55581/ejeas.1319156

Abstract: This paper presents a comparison and performance analysis of CMOS-based VDCC (Voltage Differencing Current Conveyor) circuits and differential amplifier FGMOS-based circuits. Differential amplifiers at the input stage of the VDCC circuit are designed using FGMOS instead of CMOS. Designing the differential amplifiers in the input stages of the VDCC circuit using FGMOS instead of CMOS amplifies the input signal of the circuit, providing a significant increase in linearity and voltage following properties. At the same time by using FGMOS transistors, the input stage of the circuit, which provides arithmetic calculations, is simplified. A three-input single output (TISO) type band-pass filter application is given to show the versatility of the VDCC circuit topology. The THD value of the CMOS-based VDCC filter circuit is found to be 15.99%. The THD value of the proposed differential amplifiers FGMOS-based VDCC filter circuit is found to be 1.03%. Theoretical analysis results confirm the simulation results. The presented CMOS and FGMOS-based band-pass filters are simulated using TSMC CMOS 0.18 µm technology with V_{DD}, a power supply voltage equal to 0.9 V. The proposed circuit topology will be an essential reference in the literature for researchers to design new linearly tunable filters.

Keywords: *Voltage Differencing Current Conveyor (VDCC), Floating Gate MOS (FGMOS), Voltage-Mode Band-Pass Filter.*

CMOS Tabanlı VDCC ve Fark Kuvvetlendiricisi FGMOS Tabanlı VDCC Devrelerinin Performans Analizinin Karşılaştırılması ve Filtre Uygulaması

Öz. Bu makale, CMOS tabanlı VDCC (Voltage Differencing Current Conveyor) devreleri ile fark kuvvetlendiricisi FGMOS tabanlı VDCC devrelerinin karşılaştırmasını ve performans analizini sunar. VDCC devresinin giriş aşamasındaki fark kuvvetlendiricileri, CMOS yerine FGMOS kullanılarak tasarlanır. VDCC devresinin giriş katlarındaki fark kuvvetlendiricilerinin CMOS yerine FGMOS kullanılarak tasarlanması, devrenin giriş sinyalini yükselterek doğrusallık ve voltaj takip etme özelliklerinde önemli bir artış sağlar. Aynı zamanda FGMOS transistörler kullanılarak devrenin aritmetik hesaplamaları sağlayan giriş aşaması basitleştirilir. VDCC devre topolojisinin çok yönlülüğünü göstermek için üç girişli tek çıkışlı (TISO) tip bant geçiren filtre uygulaması verilir. CMOS tabanlı VDCC filtre devresinin THD değeri %15.99 olarak bulunur. Önerilen fark kuvvetlendiricisi FGMOS tabanlı VDCC filtre devresinin THD değeri %1.03 olarak bulunur. Teorik analiz sonuçları, simülasyon sonuçlarını doğrulamaktadır. Sunulan CMOS ve FGMOS tabanlı bant geçiren filtreler, 0.9 V'a eşit bir güç kaynağı voltajı olan V_{DD} ile TSMC CMOS 0,18 µm teknolojisi kullanılarak simüle edilir. Önerilen devre topolojisi, araştırmacıların doğrusal olarak ayarlanabilir yeni filtreler tasarlamaları için literatürde önemli bir referans olacaktır.

Anahtar Kelimeler:*Gerilim Farkı Akım Taşıyıcı (VDCC), Yüzen Geçit MOS (FGMOS) Transistor, Voltaj Modlu Band-Geçiren Filtre.*

* Corresponding author
E-mail address: busra.hasilci@ogr.iuc.edu.tr (B.Hasilci)

1. Introduction

Voltage differencing current conveyors (VDCC) are a versatile active building block used in analog signal processing circuit applications. A very substantial advantage of using VDCCs in analog circuit design is that it is able electronic tunability. FGMOS is a device where the second gate, called a floating gate, is electrically isolated and capacitively connected to the input gates[1-9]. In this work presents a comparison and performance analysis of CMOS-based VDCC (Voltage Differencing Current Conveyor) circuits and differential amplifiers FGMOS-based circuitsThe design of the differential amplifiers in the input stage of the VDCC circuit using FGMOS in the place of CMOS has substantially increased the linearity range of the circuit. THD value of the CMOS based VDCC filter circuit is found to be 15.99% and the THD value of the proposed differential amplifiers FGMOS based VDCC circuit is found to be 1.03%. Theoretical analysis results confirm the simulation results. The presented CMOS and FGMOS-based band-pass filters are simulated using TSMC CMOS 0.18 μm technology with VDD, a power supply voltage equal to 0.9 V.

The use of FGMOS transistors instead of the conventional CMOS structure for the differential amplifiers in the input stage provides significant advantages. A control voltage at one of the inputs of the multi-input FGMOS provides a wide range of tunability to the circuit. Circuit designs with FGMOS allow controllability of the threshold voltage (Vth). Due to the properties of FGMOS, the linearity range increases and simplifies the input stage that provides the arithmetic calculations of the circuit. This specialty allows operation at power supply voltage levels lower than the intended operating limit.

In addition to all these features, the FGMOS VDCC consumes fewer power than required in a circuit designed with conventional MOSFET. Literature researches show that a great number of the analog circuits using VDCC as an active element have been found, for instance, capacitance multiplier [12-13], inductance simulator [10-11], versatile passive element simulator [14- 15], triangular and square wave generator [16], sinusoidal oscillator [6, 13, 17-20], first order allpass filter [21], ladder filter [22] etc. But differential amplifiers FGMOS-based VDCC has not been found before in the literature. The versatility of the proposed differential amplifiers FGMOS-based is demonstrated on a filter circuit example. The proposed filter in the reference [23], The three-inputs single-output (TISO) consists of 2 capacitances and 1 resistor. In this study, only band pass filter application is made to show that FGMOS increases linearity in a filter application.The unique aspect of this study is that there was no differential amplifiers FGMOS-based VDCC circuit design in the previous studies. The rest of the paper is organised as follows: Section 2 describes proposed circuit. Brief introduction of FGMOS and differential amplifier FGMOS based VDCC circuit is given in section 3. Simulation results are discussed in section 4. Finally, conclusions are present in section 5.

2. Proposed Circuit

The circuit symbol of the proposed in recent years active element, VDCC, is shown in Figure 1, where P and N are input terminals and Z, X, W_P and W_N are output terminals. Except the X terminal all of the terminals exhibit high impedance.

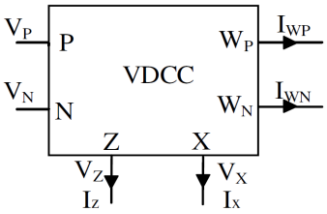

Fig. 1. *Circuit symbol of the VDCC.*

$$\begin{bmatrix} I_p \\ I_N \\ I_Z \\ V_Z \\ I_{W_p} \\ I_{W_N} \end{bmatrix} = \begin{bmatrix} 0 & 0 & 0 & 0 \\ 0 & 0 & 0 & 0 \\ \alpha g_m & -\alpha g_m & 0 & 0 \\ 0 & 0 & \beta & 0 \\ 0 & 0 & 0 & \gamma_{W_p} \\ 0 & 0 & 0 & -\gamma_{W_N} \end{bmatrix} \begin{bmatrix} V_p \\ V_N \\ V_X \\ I_X \end{bmatrix} \quad (1)$$

In equation 1, α, β and γ are the non-ideal voltage and current gains of the VDCC and ideally equal to one. gm is transconductance gain of the VDCC and is defined as:

$$g_m = \sqrt{I_{B1}\ \mu_n\ C_{ox}\ \frac{W}{L}} \quad (2)$$

In Equation (2), μ_n is the carrier mobility for NMOS transistors, C_{ox} is the gate oxide capacitance per-unit area, W is the effective channel width, L is the effective channel length, and I_{B1} is the bias current to control, and is used to control the gm.

The filter topology in Figure 2 is created using only the VDCC active element. It can be used as the three-input single-output (TISO) voltage mode filter in Figure 3 [23]. The circuit analysis gives the following for the output voltage, which can be expressed in Equation (3).

$$V_{OUT} = \frac{V_2\, s^2 C_1\, C_2 + V_1\, s\, C_2\, g_m + V_3\, g_m\, G}{s^2\, C_1\, C_2 + s C_2\, g_m + g_m\, G} \quad (3)$$

$$\begin{aligned} &(i)\ LP: V_1 = V_2 = 0, V_3 = V_{IN} \\ &(ii)\ BP: V_2 = V_3 = 0, V_1 = V_{IN} \\ &(iii)\ HP: V_1 = V_3 = 0, V_2 = V_{IN} \\ &(iv)\ BS: V_1 = 0, V_2 = V_3 = V_{IN} \\ &(v)\ AP: V_2 = V_3 = -V_1 = V_{IN} \end{aligned} \quad (4)$$

The circuit of quality factor (Q) and pole frequency (w_0) can be given as follows:

$$Q = \sqrt{\frac{G\, C_1}{g_m\, C_2}} \quad (5)$$

$$w_0 = \sqrt{\frac{g_m\, G}{C_1\, C_2}} \quad (6)$$

Figure 2 shows CMOS implementation of the VDCC. Figure 3 shows TISO biquad filter. The terminals of the TISO biquad

filter in Figure 3 are shown in Figure 1 and Figure 2. Three-inputs single-output (TISO) filter which can make real all five types of biquadratic functions in voltage mode that is low-pass, high-pass, band-pass, band-stop, and all-pass filter with single VDCC. In this work, only the band-pass filter application is included to show the accuracy of the proposed circuit. For the TISO filter, pole frequency can be tuned electronically with changing bias current. In addition, VDCC-based biquad filter circuit with a minimum number of grounded passive elements have been studied in the present paper. A voltage mode biquad filter which involves a single VDCC and a few passive elements has been presented. Therefore, this filter circuit is used for the application. The design of the differential amplifiers at the input stage of the VDCC active element of the TISO filter circuit using FGMOS has increased the linearity significantly, as can be seen in Figure 5. The performances of the VDCC-based TISO filter are illustrated by SPICE simulations. The theoretical analysis of the filter agreed well with the SPICE simulations. Table 1 shows the aspect ratios of the transistors for the VDCC in Figure 2.

In this study, the two differential amplifiers in the input stage of the VDCC circuit are designed using FGMOS instead of CMOS. The design of the differential amplifiers in the input stages of the VDCC circuit topology using FGMOS instead of CMOS provides a significant increase in linearity and voltage following properties by amplifying the input signal of the circuit.

In this section, floating gate MOSFET (FGMOS) and differential amplifier FGMOS-based VDCC circuits have been briefly introduced with their schematic representation. This section also explains the implementation of FGMOS and differential amplifier FGMOS-based VDCC circuit into the final design.

3. FGMOS and Differential amplifier FGMOS-based VDCC circuit

In this section, floating gate MOSFET (FGMOS) and differential amplifier FGMOS-based VDCC circuits have been briefly introduced with their schematic representation. This section also explains the implementation of FGMOS and differential amplifier FGMOS-based VDCC circuit into the final design.

3.1. Floating Gate MOSFET (FGMOS)

Floating Gate MOS transistors are widely used in analog and digital world as EPROM, EEPROM, flash memories, and neuronal computational element in neural network. Especially FGMOS used in low-voltage, low-power analog design and analog storage elements is gaining popularity day by day. A typical multi input floating gate transistor is shown in Figure 4. It is a conventional MOSFET in which the gate is capacitively coupled to the input using another poly-silicon layer. The equation that models the behaviour of floating gate voltage (VFG) of FGMOS is given by equation (7).

$$V_{FG}\text{-}\Sigma_{i=1}^{N}\frac{C_i}{C_T}V_{i+}\frac{C_{gs}}{C_T}V_{S+}\frac{C_{gd}}{C_T}V_{D+}\frac{Q_{FG}}{C_T} \quad (7)$$

Where C_T-C_{GS}+C_{GD}+$\Sigma_{i=1}^{N}C_i$ and Q_{FG} explain the amount of charges that is being trapped in FG during fabrication. FGMOS provides impressive features with low-voltage, low-power context. In application of linear and nonlinear functions provides flexibility to designers. Also, since FGMOS is multi-input, it allows adding extra inputs according to the needs of the designer. In this way, tunability feature is earned to the circuit.

4. Simulation Results

Finally, a CMOS realization of a VDCC circuit is shown in Figure 3. The supply voltages and biasing currents are given by V_{DD} = −V_{SS} = 0.9 V, I_{B1} = 50 µA, and I_{B2} = 100 µA, respectively. The aspect ratios of the transistors are given in Table 1. The MOS transistors are simulated using TSMC CMOS 0.18 µm process model parameters. In the CMOS and FGMOS based designs of the voltage mode filter shown in Figure 3, R_1 = 2 kΩ and C_1 = C_2 = 50 pF. A typical multi input floating gate transistor is shown in Figure 4.

Figure 5 shows the linearity comparison of VDCC circuit topologies. The design of the differential amplifiers in the input stages of the VDCC circuit using FGMOS instead of CMOS provided a significant increase in the linearity and voltage following properties of the circuit.

Figure 6 shows the I_X-I_Z DC characteristics of CMOS based VDCC and differential amplifiers FGMOS-based VDCC circuits. Differential amplifiers FGMOS-based VDCC circuit's I_X-I_Z DC characteristic graph produced a more symmetrical result for the -100µA to 100µA range compared to the CMOS-based VDCC circuit.

Figure 7 shows the I_{wn}/I_x and I_{wp}/I_x DC characteristics of CMOS-based VDCC and differential amplifiers FGMOS-based VDCC circuits. Differential amplifiers FGMOS-based VDCC circuit's Iwn/Ix and Iwp/Ix DC characteristic graphs produced more symmetrical results for -100µA to 100µA range compared to CMOS-based VDCC circuit.

Figure 8 shows the I_X/I_Z magnitude AC characteristics of CMOS and differential amplifier FGMOS-based VDCC circuits. The fact that the I_X/I_Z ratio is equal to 1 in the differential amplifier FGMOS-based VDCC circuit shows that the current at the X terminal is transferred to the Z terminal exactly.

Figure 9 shows the I_{WN}/I_X, I_{WP}/I_X magnitude AC characteristics of CMOS and differential amplifiers FGMOS-based VDCC circuits. The fact that the I_{WN}/I_X, I_{WP}/I_X ratios are equal to 1 in the differential amplifiers FGMOS-based VDCC circuit shows that the current at the I_{WN} and I_{WP} terminals are transferred to the X terminal exactly.

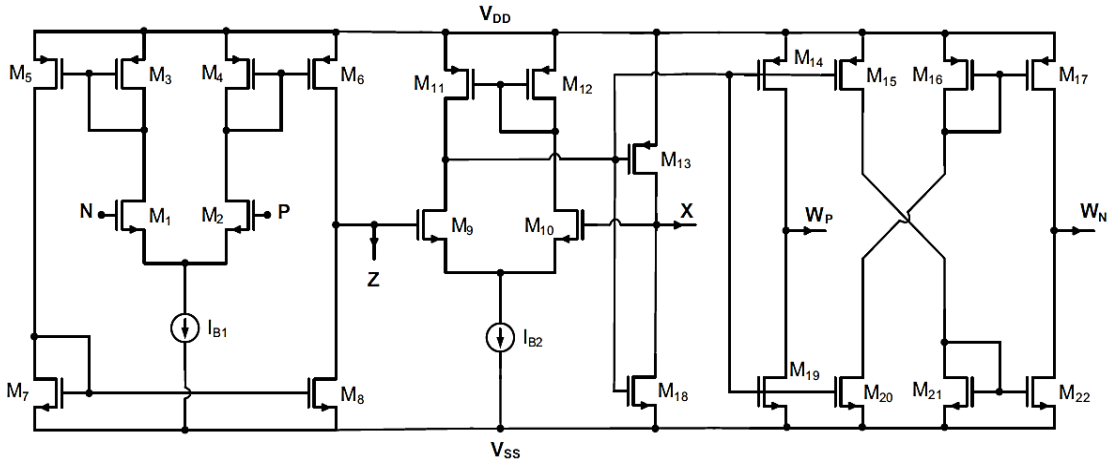

***Fig. 2**. CMOS implementation of the VDCC [23].*

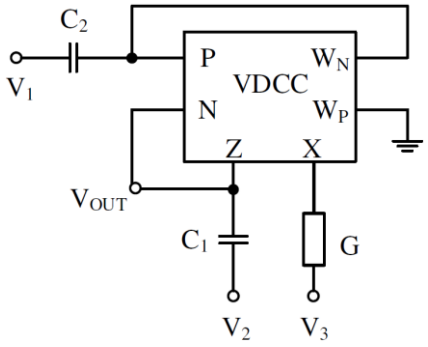

***Fig. 3**. TISO biquad filter [24].*

Table 1 Transistors aspect ratios for the VDCC of Figure. 2.

Transistors	W/L(μm)
M_1-M_4	3.6/1.8
M_5-M_6	7.2/1.8
M_7-M_8	2.4/1.8
M_9-M_{10}	3.06/0.72
M_{11}-M_{12}	9/0.72
M_{13}-M_{17}	14.4/0.72
M_{18}-M_{22}	0.72/0.72

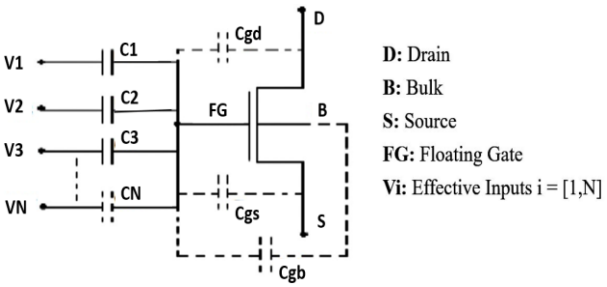

***Fig. 4**. Equivalent schematic of N-input n-channel FGMOS [24].*

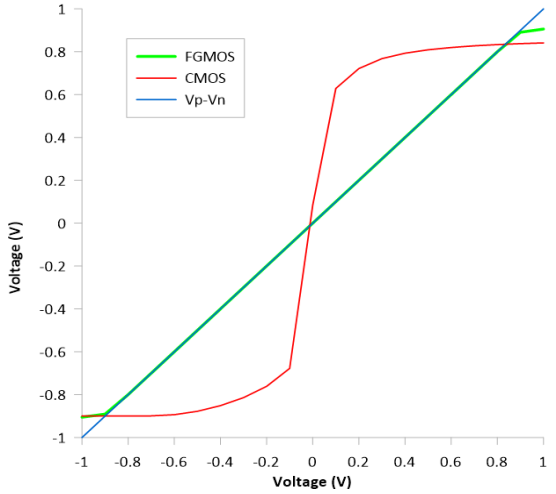

***Fig. 5**.Comparison of linearity VDCC circuit topologies.*

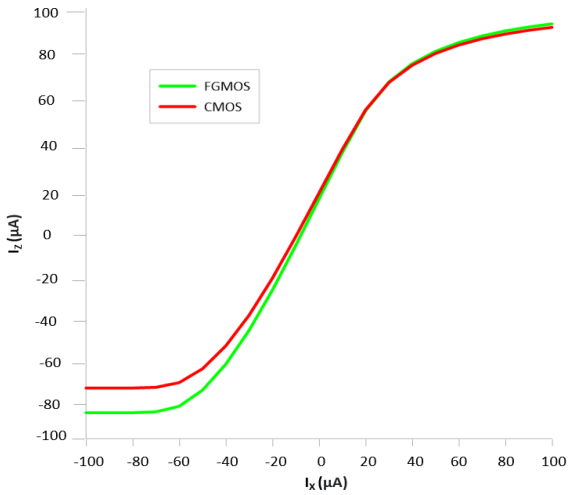

***Fig. 6**. I_X-I_Z DC characteristics of CMOS and differential amplifiers FGMOS-based VDCC circuits.*

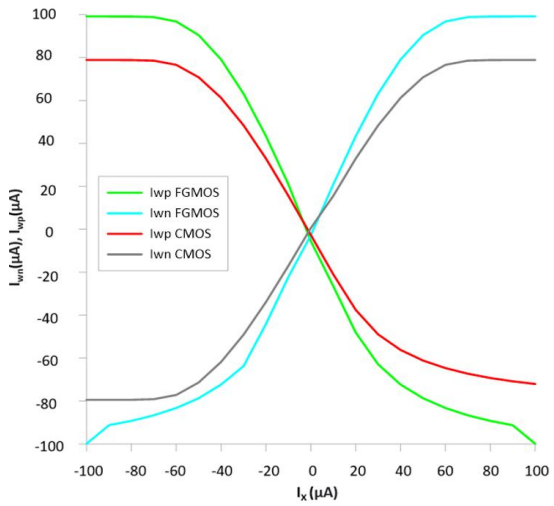

Fig. 7. *I_{wn}/I_x and I_{wp}/I_x DC characteristics of CMOS and differential amplifier FGMOS based VDCC circuits.*

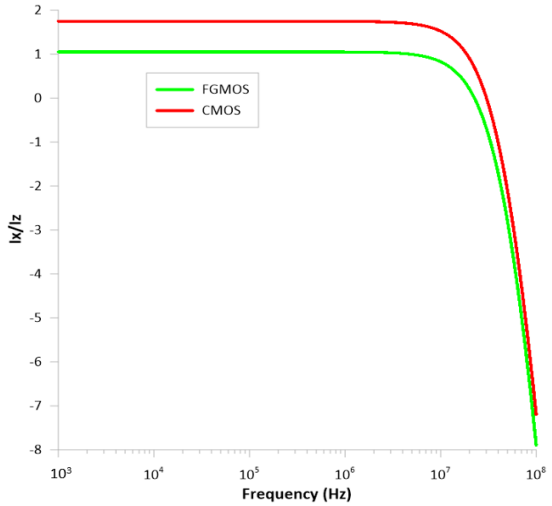

Fig. 8. *CMOS and FGMOS based VDCC AC Characteristics I_{Rx}/I_{RZ} magnitude.*

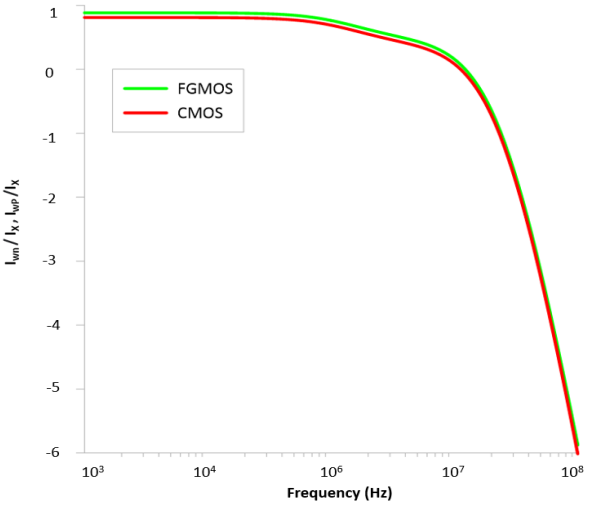

Fig. 9. *CMOS and FGMOS-based VDCC AC Characteristics I_{WN}/I_X, I_{WP}/I_X magnitude.*

Figure 10 shows magnitude of CMOS based VDCC band-pass filter and differential amplifiers FGMOS-based VDCC band-pass filter. The simulation result of the CMOS and FGMOS-based two filter circuits shown in the figure is found to be compatible with the characteristic of the band-pass filter circuit.

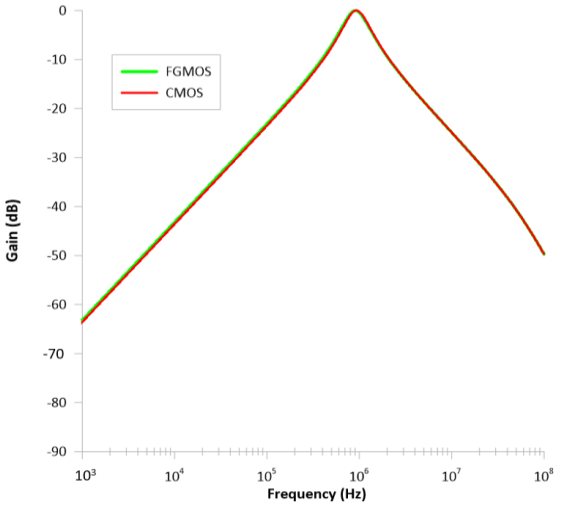

Fig. 10. *Magnitude of CMOS based VDCC band-pass filter and differential amplifiers FGMOS-based VDCC band-pass filter.*

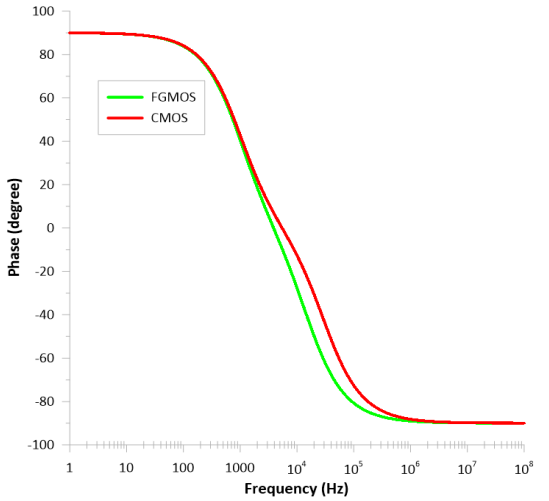

Fig. 11.*Phase of CMOS based VDCC band-pass filter and differential amplifiers FGMOS-based VDCC band-pass filter.*

Figure 11 shows phase of CMOS based VDCC band-pass filter and differential amplifiers FGMOS-based VDCC band-pass filter. The phase of CMOS-based VDCC band-pass filter and differential amplifiers FGMOS-based VDCC band-pass filter circuits is found in accordance with the band-pass filter characteristic and is between -90 degree and 90 degree.

Figure 12 shows the THD analysis of the CMOS based-VDCC and differential amplifier FGMOS-based VDCC band-pass filter. V_P is a pure sine signal applied to the input. V_Z refers to the output of the band-pass filter. The output voltage of the CMOS based-VDCC filter circuit is between +0.7 V and -0.7 V. Differential amplifier FGMOS-based VDCC band-pass filter output voltage is between +0.9 V and -0.9 V. As can be seen from the Figure 12, the output voltage V_P of the proposed circuit is found to be closer to the pure sine voltage.

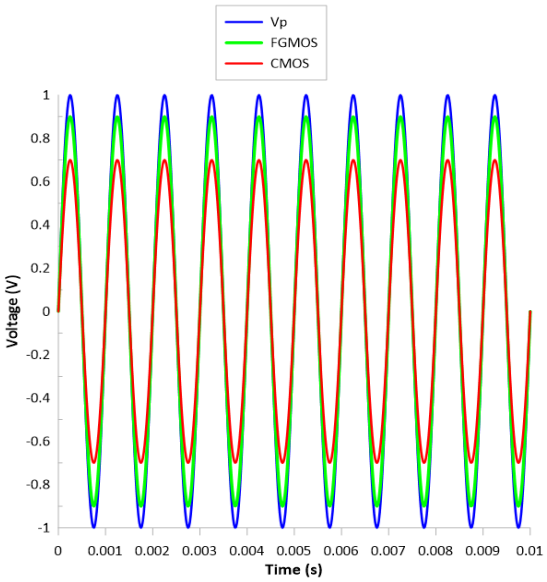

Fig. 12*.THD analysis of CMOS VDCC band-pass filter and differential amplifier FGMOS- based VDCC band-pass filter.*

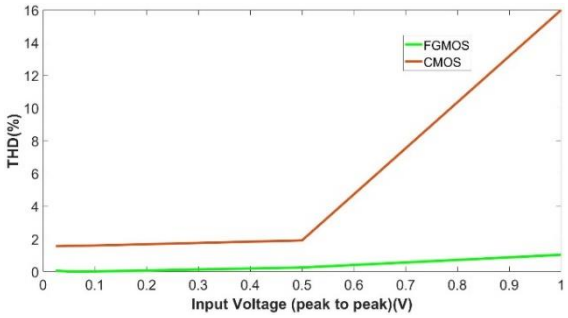

Fig. 13*. THD value of CMOS VDCC BP filter and differential amplifiers FGMOS-based VDCC band-pass filter.*

Figure 13 shows the THD analysis of the CMOS VDCC band-pass filter and differential amplifiers FGMOS-based VDCC band-pass filter. THD indicates the percentage of distortion from the fundamental waveform. THD is used to determine harmonics in voltage and current [25]. Voltage THD is expressed as the ratio of the sum of all voltage harmonic components apart from the fundamental voltage component to the fundamental voltage component [26]. According to the IEEE 519 standard, the maximum acceptable THD value for low-voltage applications is 5%, and also maximum acceptable value for individual voltage harmonics is 3% [27-30].

The THD value of the CMOS VDCC band-pass filter circuit was 15.99%, and the THD value of the differential amplifier FGMOS-based VDCC band-pass filter circuit was found to be 1.03%. The fact that the THD value in the band-pass filter application of the proposed circuit is lower indicates that the linearity is substantially increased.

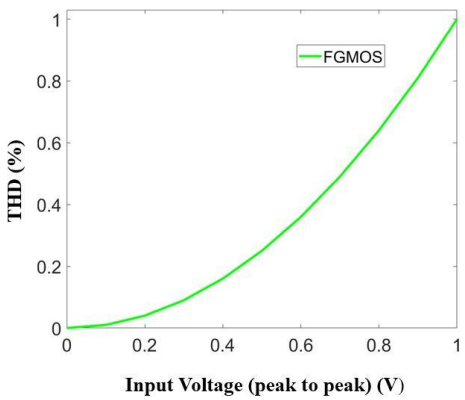

Fig. 14*.THD value of differential amplifiers FGMOS-based VDCC band-pass filter.*

Figure 14 shows the THD analysis of the differential amplifier FGMOS-based VDCC band-pass filter. THD value of the FGMOS-based VDCC band-pass filter circuit was found to be 1.03%.

5. Conclusion

This paper presents a comparison and performance analysis of CMOS-based VCDD (Voltage Differencing Current Conveyor) circuits and differential amplifiers FGMOS-based circuits. The design of the differential amplifiers in the input stage of the VDCC circuit using FGMOS instead of CMOS has significantly increased the linearity range of the VCDD active element. THD value of the CMOS based VCDD filter circuit is found to be 15.99%, and the THD value of the proposed differential amplifier FGMOS-based VDCC circuit is found to be 1.03%. The presented CMOS and FGMOS-based band-pass filters are simulated using TSMC CMOS 0.18 µm technology with a power supply voltage, V_{DD}, equal to 0.9V. As a result, the use of FGMOS transistors at the input stage of the VDCC circuit amplifies the input signal of the circuit, providing a significant increase in linearity and voltage following properties. The proposed FGMOS-based circuit topology will be an important reference in the literature for researchers to design new linearly tunable filters.

Author Contributions

Format analysis – Büşra Hasılcı (BH) - Fırat Kaçar (FK); Simulation Performance - BH, Processing - BH, FK; Literature review – BH, FK; Writing - BH; Review and editing - BH, FK.

Declaration of Competing Interest

The authors declared no conflicts of interest with respect to the research to the research, authorship, and/or publication of this article.

References

[1] Villegas, E.R., *Low power and low voltage circuit design with the FGMOS transistor*, In: The Institution of Engineering and Technology, pp. 7-40, 2006.

[2] Martin, M. N., Roth, D. R., Garrison-Darrin, A., McNulty, P. J., & Andreou, A. G. (2001). FGMOS dosimetry: Design and implementation. *IEEE Transactions on Nuclear Science*, *48*(6), 2050-2055.

[3] Yin, L., Embabi, S. H. K., & Sanchez-Sinencio, E. (1997).

A floating-gate mosfet D/A converter. In *1997 IEEE International Symposium on Circuits and Systems (ISCAS)*, pp. 409-412). IEEE.

[4] Manhas, P. S., Sharma, S., Pal, K., Mangotra, L. K., & Jamwal, K. K. S. (2008). High performance FGMOS-based low voltage current mirror, 46, 355-358.

[5] Razavi, B., Design of analog integrated circuits, In: McGraw Hill, Second Edition, pp.1-124, 2001.

[6] Rajput, S. S., & Jamuar, S. S. (2000). A high performance current mirror for low voltage designs, *IEEE APCCAS 2000. 2000 IEEE Asia-Pacific Conference on Circuits and Systems. Electronic Communication Systems.(Cat. No. 00EX394)* (pp. 170-173). IEEE.

[7] Sharma, S., Rajput, S. S., Magotra, L. K., & Jamuar, S. S. (2002). FGMOS based wide range low voltage current mirror and its applications. *In Asia-pacific conference on circuits and systems*, (pp. 331-334), IEEE.

[8] Gupta, R., Sharma, S., & Jamuar, S. S. (2010). A low voltage current mirror based on quasi-floating gate MOSFETs. *2010 Institute of Electrical and Electronics Engineers Asia Pacific Conference on Circuits and Systems,* (pp. 580-583), IEEE.

[9] Anand, A., Mandal, S. K., Dash, A., & Patro, B. S. (2013). FGMOS based low-voltage low-power high output impedance regulated cascode current mirror. *International Journal of VLSI Design & Communication Systems*, *4*(2), 39-41.

[10] Gupta, S., Sandhu, M., Gupta, M., & Arora, T. S. (2019). A new electronically tunable CM/VM oscillator using all grounded components. *Applications of Artificial Intelligence Techniques in Engineering: SIGMA 2018, 2*, 141-151, Springer Singapore.

[11] Horng, J. W. (2008). High input impedance voltage-mode universal biquadratic filter with three inputs using DDCCs. *Circuits, Systems & Signal Processing*, *27*, 553-562.

[12] Keskin, A. Ü. (2006). Multi-function biquad using single CDBA. *Electrical Engineering*, 88, 353-356.

[13] Tangsrirat, W., Tanjaroen, W., & Pukkalanun, T. (2009). Current-mode multiphase sinusoidal oscillator using CDTA-based allpass sections. *AEU-International Journal of Electronics and Communications*, *63*(7), 616-622.

[14] Horng, J. W. (2002). Voltage-mode universal biquadratic filter with one input and five outputs using OTAs. *International Journal of Electronics*, *89*(9), 729-737.

[15] Lee, C. N. (2010). Multiple-mode OTA-C universal biquad filters. *Circuits, Systems and Signal Processing*, *29*, 263-274.

[16] Shah, N. A., Rather, M. F., & Iqbal, S. Z. (2003). Three input and one output voltage-mode universal filter, *IJPAP 41(7), 556-558.*

[17] Chaturvedi, B., Mohan, J., Kumar, A., & Pal, K. (2020). Current-mode first-order universal filter and its voltage-mode transformation. *Journal of Circuits, Systems and Computers*, *29*(09), 2050149,

[18] Kaçar, F., & Yeşil, A. (2010). Voltage mode universal filters employing single FDCCII. *Analog Integrated Circuits and Signal Processing*, *63*, 137-142.

[19] Kaçar, F., Metin, B., Kuntman, H., & Cicekoglu, O. (2010). A new high-performance CMOS fully differential second-generation current conveyor with application example of biquad filter realisation. *International Journal of Electronics,* 97(5), 499-510,

[20] Kaçar, F., & Yeşil, A. (2012). FDCCII-based electronically tunable voltage-mode biquad filter. *International Journal of Circuit Theory and Applications*, *40*(4), 377-383.

[21] Kacar, F., Yesil, A., & Noori, A. (2012). New CMOS realization of voltage differencing buffered amplifier and its biquad filter applications. *Radioengineering*, *21*(1), 333-339.

[22] Biolek, D., Senani, R., Biolkova, V., & Kolka, Z. (2008). Active elements for analog signal processing: classification, review, and new proposals. *Radioengineering*, *17*(4), 15-32.

[23] Kaçar, F., Yeşil, A., Minaei, S., & Kuntman, H. (2014). Positive/negative lossy/lossless grounded inductance simulators employing single VDCC and only two passive elements. *AEU-International Journal of Electronics and Communications*, *68*(1), 73-78,

[24] Kaçar, F., Yeşil, A., & Gürkan, K. (2015). Design and experiment of VDCC-based voltage mode universal filter. *Indian Journal of Pure & Applied Physics*, 53(5), 341-349.

[25] Anand, A., Mandal, S. K., Dash, A., & Patro, B. S. (2013). FGMOS based low-voltage low-power high output impedance regulated cascode current mirror. *International Journal of VLSI Design & Communication Systems*, 4(2), 39-50,

[26] Patidar, R. D., & Singh, S. P. (2009). Harmonics estimation and modeling of residential and commercial loads. *2009 International Conference on Power Systems* (pp. 1-6). IEEE.

[27] Sivaraman, P., & Sharmeela, C. Power system harmonics, In: Power Quality in Modern Power Systems, Academic Press, pp. 61-103, 2021.

[28] Prabaharan, N., & Palanisamy, K. (2017). A comprehensive review on reduced switch multilevel inverter topologies, modulation techniques, and applications. *Renewable and Sustainable Energy Reviews,* 76, 1248-1282,

[29] https://www.ieee.org/ (Access Date: 03.05.2023)

[30] IEEE. (2022). Standard for Harmonic Control in Electric Power Systems, *IEEE Std 519-2022 (Revision of IEEE Std 519-2014)*, 1-31.

European Journal of Engineering and Applied Sciences

ISSN: 2651-3412 (Print) & 2667-8454 (Online)
Journal homepage: http://dergipark.gov.tr/EJEAS
Published by Çorlu Faculty of Engineering, Tekirdağ Namık Kemal University

European J. Eng. App. Sci. 6(1), 32-40, 2023

Research Article

The Efficiency of Transfer Learning and Data Augmentation in Lemon Leaf Image Classification

Ahmet Saygılı[1, *]

[1] **Department of Computer Engineering, Çorlu Engineering Faculty, Tekirdağ Namık Kemal University, Tekirdağ, Turkey, 59860**
[1]**asaygili@nku.edu.tr**

Received: 30.06.2023 *Accepted: 25.07.2023* *DOI: 10.55581/ejeas.1321042*

Abstract: Leaf diseases in trees and plants are important factors that directly affect the yield of agricultural products. This problem may cause a decrease in the production capacity and profitability of farmers. For this reason, computer-aided detection and classification systems are needed to accurately detect plant diseases. In recent years, learning algorithms and image-processing techniques have been used effectively in the agricultural sector. In this study, the efficiency of transfer learning and data augmentation methods on a dataset consisting of lemon leaf images is examined and the classification of diseased and healthy lemon leaf images is performed. In our study, VGG16, ResNet50, and DenseNet201 transfer learning methods were applied both with and without data increment, and the effect of data augmentation on performance was evaluated. Among the deep transfer learning methods used, DenseNet201 gave the highest accuracy rate with 98.29%. This study shows that transfer learning methods can effectively distinguish between diseased and healthy lemon leaves. It has also been observed that data augmentation does not always provide performance improvement. In future studies, it is predicted that it will be appropriate to evaluate the effect of data augmentation more effectively by applying deep transfer learning methods to plants with different class numbers.

Keywords: *Data Augmentation, Image Processing, Lemon Leaf Diseases, Transfer Learning*

Limon Yaprağı Görüntü Sınıflandırmasında Transfer Öğrenme ve Veri Artırımın Etkinliği

Öz. Ağaç ve bitkilerde yaprak hastalıkları, tarımsal ürünlerin verimini doğrudan etkileyen önemli faktörlerdir. Bu sorun, çiftçilerin üretim kapasitelerinin ve karlılık düzeylerinin düşmesine neden olabilmektedir. Bu nedenle bitki hastalıklarını doğru bir şekilde tespit edebilmek için bilgisayar destekli tespit ve sınıflandırma sistemlerine ihtiyaç duyulmaktadır. Son yıllarda öğrenme algoritmaları ve görüntü işleme teknikleri tarım sektöründe etkin bir şekilde kullanılmaktadır. Bu çalışmada, limon yaprağı görüntülerinden oluşan bir veri kümesi üzerinde transfer öğrenme ve veri artırma yöntemlerinin etkinliği incelenerek hastalıklı ve sağlıklı limon yaprağı görüntüleri sınıflandırılması işlemi yapılmaktadır. Çalışmamızda VGG16, ResNet50 ve DenseNet201 transfer öğrenme yöntemleri hem veri artırımlı hem de artırımsız olarak uygulanmış ve veri artırmanın performansa etkisi değerlendirilmiştir. Kullanılan derin transfer öğrenme yöntemleri arasında en yüksek doğruluk oranını %98,29 ile DenseNet201 vermiştir. Gerçekleştirilen bu çalışma, transfer öğrenme yöntemlerinin hastalıklı ve sağlıklı limon yapraklarını etkili bir şekilde ayırt edebildiğini göstermektedir. Veri artırmanın her zaman performans iyileşmesi sağlamadığı da gözlemlenmiştir. Gelecekteki çalışmalarda derin transfer öğrenme yöntemleri farklı sınıf sayılarına sahip bitkilerde uygulanarak veri artırmanın etkisinin daha etkili bir şekilde değerlendirilmesinin uygun olacağı öngörülmektedir.

* **Corresponding author:**
E-mail address: asaygili@nku.edu.tr (A.Saygılı)

Anahtar Kelimeler: *Veri Artırımı, Görüntü İşleme, Limon Yaprağı Hastalıkları, Transfer Öğrenme*

1. Introduction

Plants protect the ozone layer because they provide food for all terrestrial living organisms and are responsible for filtering out the sun's harmful UV radiation [1]. The Food and Agriculture Organization of the United Nations (FAO) recommends that agricultural production should increase by 70% by 2050 to meet the world's food needs [2]. However, agriculture has been an important source of economic growth for countries. The farmer selects the required product according to the soil type, weather conditions, and economic value of the place. Alternative methods are sought to increase food production due to increasing population and climate changes [3]. Information technologies have a great contribution in this sense. Machine learning and deep learning methods and automatic disease detection systems are mechanisms created for this purpose. Diseases in the leaves of trees and plants are factors that directly affect the yield of agricultural products [4]. This is an important problem that may lead to a decrease in the production capacity and profitability of farmers. The detection of diseases of plants is determined as a result of the visual examinations of the farmers. An error in these determinations can lead to negative results. For this reason, computer-aided detection and classification systems are needed to accurately detect plant diseases. Learning algorithms and image processing methods, which have been actively used in almost all fields in recent years, can also be used effectively in this field. There are many studies done in this area.

Today, deep learning techniques are successfully applied in many areas in the field of image classification. However, the use of these techniques often requires large datasets and may encounter performance problems when we do not have sufficient training data. Transfer learning methods solve or at least alleviate such problems with data augmentation techniques. In this article, we will examine the effectiveness of transfer learning and data augmentation methods on an image dataset consisting of lemon leaves. Transfer learning is the reuse of a previously trained model to solve the task on the target dataset. Data augmentation is a technique that allows the creation of new samples by applying various transformations to the existing data set. In this study, transfer learning methods were used to distinguish the diseased and healthy images of lemon leaves from each other. Transfer learning methods were applied with and without data augmentation, and the effect of data augmentation on success was tried to be evaluated. Models were created using deep transfer learning methods VGG16, ResNet50, and DenseNet201. Therefore, our contribution to this article;

- Models were created with transfer learning methods to classify the disease from lemon leaves.
- The effects of data augmentation on classification success were analyzed.
- DenseNet201, one of the CNN models based on transfer learning, gave a very high accuracy rate for plant leaf disease classification.
- A study has been presented that can be used for early diagnosis of lemon leaf diseases.

The details of our article are explained in the following sections. Chapter 2 shows a brief literature review of different disease detection patterns from plant leaves. Chapter 3 describes the material and method. Then, experimental results and analysis are presented in section 4. Finally, section 5 presents the results of the study and future work.

2. Literature Review

There are many studies in the literature using the leaves of plants. The first of these is the study of Subramanian et al. [5]. In this study, Subramanian et al. suggest the use of Deep Learning models based on Transfer Learning for the classification of lemon leaf diseases. According to the results obtained in the study, it is stated that the use of Deep Learning models based on transfer learning can be an effective and cost-effective method in the classification of lemon leaf diseases. Among the models used, Xception gave the highest accuracy rate with 94.34%. Banni et al. [6] proposed a model using GLCM algorithms to detect citrus leaf disease. The accuracy rate obtained in the study is around 85.71%. In the study of Sardogan et al. [7], a method is proposed to detect and classify tomato leaf diseases using Convolutional Neural Network (CNN) and Learning Vector Quantification (LVQ) algorithms. Tomato leaves are divided into four different classes: bacterial spot, late blight, Septoria leaf spot, and yellow curly leaf diseases. The average success rate for all leaf varieties was 86%.

Rastogi et al. [8] propose a method for the automatic detection and grading of leaf diseases in agriculture using digital image processing and machine vision technology. They evaluated the proposed system in two stages. In the first stage, plant recognition is carried out according to the characteristics of the leaf, which includes pre-processing of leaf images, feature extraction, and Neural Network-based training and classification for leaf recognition. In the second stage, segmentation of the diseased area on the leaf with the K-Means method, feature extraction of the defective part, and classification of the disease with the ANN method is performed. In the study of Padol et al. [9], a grape leaf disease detection system with an SVM classification method is suggested. In the study, first of all, the diseased area is segmented with K-means. Color and texture properties are then extracted. Finally, the SVM classification technique is used to detect the type of leaf disease. The accuracy rate of the proposed system was 88.89%. Ahmed et al. In their study [10], they present a system for detecting three common diseases (leaf spot, bacterial leaf blight, and brown spot diseases) in rice plants using machine learning techniques. After the preprocessing step, the dataset is classified by several different machine learning algorithms including KNN, J48, Naive Bayes, and Logistic Regression. When the decision tree algorithm was applied to the test data set after 10 times cross-validation, an accuracy rate of over 97% was obtained.

Agarwal et al. [11] propose a deep learning-based approach to

detect and classify tomato leaf diseases using Convolutional Neural Network (CNN). Experimental results show that the proposed model outperforms pre-trained models such as VGG16, InceptionV3, and MobileNet, with a classification accuracy ranging from 76% to 100% for different classes and an average accuracy of 91.2% for 9 diseases and 1 healthy. Irmak and Saygılı [12] discuss the use of convolutional neural networks (CNNs) for the automatic classification of major tomato leaf diseases that significantly affect tomato efficiency. In the study, a CNN model is proposed for the classification of tomato leaves. As a result of the study, a test accuracy of 97.05% was obtained. Kurmi et al. [13] performed disease detection on 3 different plants (bell pepper, potato, and tomato) using the PlantVillage dataset. Success rates with CNN are 95.80%, 94.10 and 92.60, respectively. Chen et al. [14] aimed to detect disease from potato leaves using the same data set. They also achieved a success rate of 97.73% in the study where they used the MobileNet V2 method. Elfatimi et al. [15] detected disease from bean leaves in their study on the data set they obtained from the Kaggle platform. The success rate obtained by using the MobileNet method in the study is 97.00%.

3. Material and Methods

The dataset used in our study is a dataset consisting of diseased and healthy plant images on the Kaggle platform [16]. In this data set, as seen in Figure 1, there are diseased and healthy leaf images of different plants. In our study, diseased and healthy image data of lemon images were used. The lemon dataset contains 159 images of healthy leaves and 77 images depicting diseased leaves.

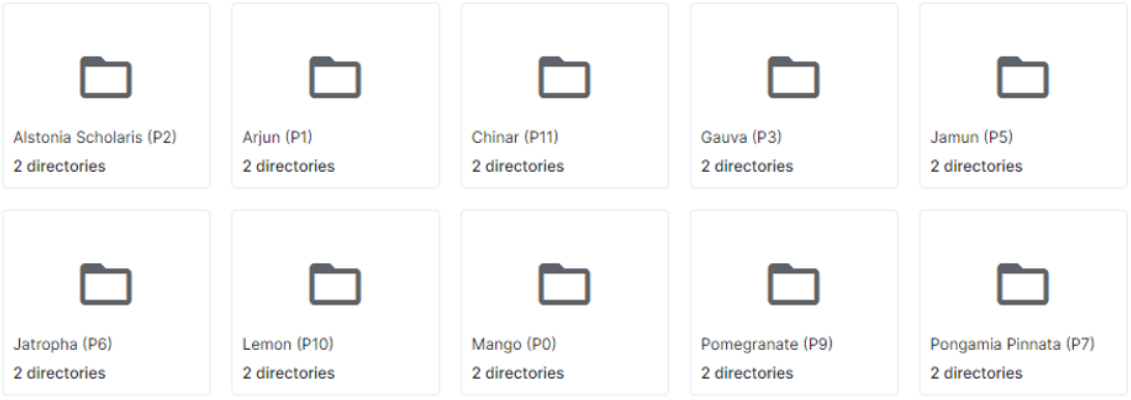

Fig. 1. *Plant species included in the data set*

Examples of diseased and healthy images in the data set are shown in Figure 2. It can also be seen with the naked eye that there are various differentiations on the diseased leaves.

In our study, the classification process was carried out on the lemon dataset by using the transfer learning methods VGG16, ResNet50, and DenseNet201. The VGG16 method is a convolutional neural network (CNN) model used in the field of deep learning [17].

VGG16 is a CNN model with 16 layers, as seen in Figure 3. One of the most important features of VGG16 is that it has a very simple architecture. The model consists of successive layers and mostly uses small 3x3 filters. VGG16 contains 13 convolutional layers, followed by 3 fully connected layers. Fully connected layers perform the classification. VGG16 is trained on the ImageNet dataset. ImageNet is a dataset of millions of images and includes many different classes of objects. During the training of VGG16, it was aimed to extract the features of these images. VGG16 is often used in image classification tasks. It performs particularly well in tasks such as object recognition and classification. It can also be used with transfer learning methods, i.e. it can be adapted to a different dataset by taking the previously trained network of VGG16 and retraining its last layers for another task. It was used in this way in our study as well.

ResNet50 is short for Residual Network and is a type of convolutional neural network (CNN) introduced by He Kaiming et al. in 2015 [18]. As shown in Figure 4, ResNet50 is a 50-layer convolutional neural network (48 convolutional layers, a MaxPool layer, and an average pool layer). The key difference of ResNet50 from other models is an innovative way to add more convolution layers to a CNN without falling into the vanishing gradient problem, using a concept called short-cut connections. A shortcut link bypasses some layers and turns a normal network into a residual one. In this way, ResNet50 can maintain its performance during training while creating a deeper network. In addition, ResNet50 can perform better than other models, although it has fewer parameters.

DenseNet201 [19], shown in Figure 5, is a 201-layer convolutional neural network (CNN). The most important difference of DenseNet201 from other models is an artificial neural network called Dense Convolutional Network (DenseNet), which connects each layer to a feed-oriented mode. The main idea behind DenseNet is the dense connectivity model, where each layer receives input from all previous layers and passes its feature maps to all subsequent layers. This dense connectivity facilitates feature reuse and improves the flow of information across the network. DenseNet-201 specifically refers to the DenseNet variant with 201 layers, including convolutional, pooling, heap normalization, and fully connected layers.

The number of layers and parameters of these three transfer learning methods are shown in Table 1.

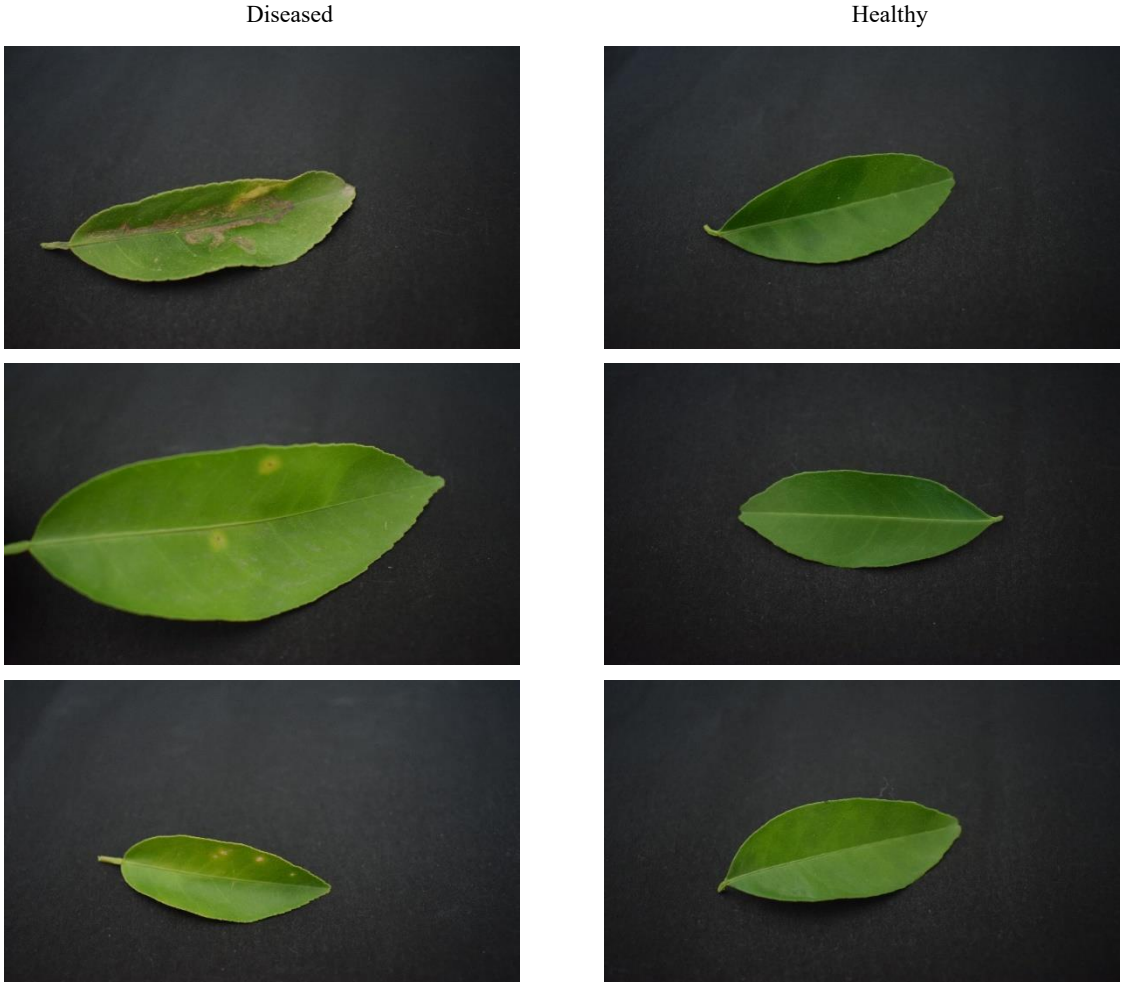

Fig. 2. *Diseased and healthy images in the lemon dataset*

Table 1 Layer and parameter numbers of the methods

Model	VGG16	ResNet-50	DenseNet201
Number of Layers	16	50	201
Number of Parameters (in million)	138	23	20

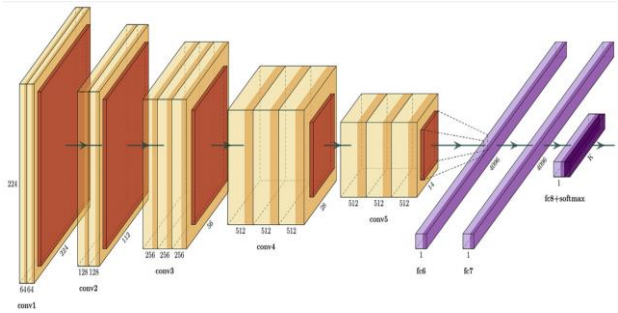

Fig. 3. *VGG16 layers [20]*

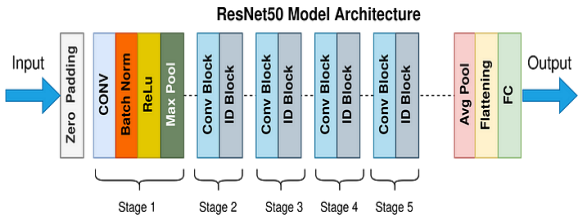

Fig. 4. *ResNet50 layers [21]*

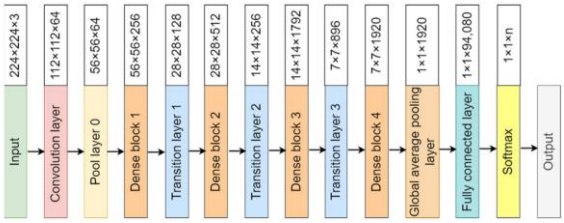

Fig. 5. *DenseNet201 layers [22]*

Since the effect of augmentation on success was investigated in the study, the effect of augmentation on success was examined by applying Reflection, Translation, Scale, and Rotation. In our study, the steps performed in the augmentation process on the MATLAB platform are seen in the code snippet

below.

Table 2 Image Augmentation Code:

```
pixelRange = [-30 30];
scaleRange = [0.9 1.1];
rotationRange = [0 360];
imageAugmenter = imageDataAugmenter( ...
RandXReflection', true, ...
'RandXTranslation',pixelRange, ...
'RandYTranslation',pixelRange, ...
'RandXScale',scaleRange, ...
'RandYScale',scaleRange, ...
'RandRotation', rotationRange)
```

- pixelRange = [-30 30]; This sets the spacing for random scrolling in the x and y directions. The image will be randomly shifted between -30 and 30 pixels in both directions.
- scaleRange = [0.9 1.1]; This sets the random scaling range in the x and y directions. The image will be scaled randomly between 90% and 110% of its original size.
- rotationRange = [0 360]; This sets the interval for random spins. The image will be randomly rotated between 0 and 360 degrees.
- 'RandXReflection', true, This means the image can be randomly mirrored (flipped) along the x-axis.
- 'RandXTranslation',pixelRange, This sets the range to the previously defined 'pixelRange' for random scrolling in the x direction.
- 'RandYTranslation',pixelRange, This sets the range to the previously defined 'pixelRange' for random scrolling in the y direction.
- 'RandXScale',scaleRange, This sets the random scaling range in the x direction to the previously defined `scaleRange`.
- 'RandYScale',scaleRange, This sets the random scaling range in the y direction to the previously defined `scaleRange`.
- 'randRotation', rotateRange); This sets the range to the predefined 'rotationRange' for random spins.

In summary, as a result of the code snippet given above, it will create an "imageDataAugmenter" object that can be randomly flipped, scaled, rotated, and mirrored. This is an efficient method used to augment the image dataset in deep learning applications.

4. Experimental Results

In our study, Accuracy, Sensitivity, Specificity, and F1 Score metrics were used for performance measurement. These metrics are calculated in Formulas (1), (2), (3), and (4). In the formulas, TP refers to correctly predicted positives, TN refers to correctly predicted negatives, FP refers to incorrectly predicted positives, and FN refers to incorrectly predicted negatives.

$$\text{Accuracy} = \frac{\text{TP} + \text{TN}}{(\text{TP} + \text{TN} + \text{FP} + \text{FN})} * 100 \quad (1)$$

$$\text{Sensitivity} = \frac{\text{TP}}{(\text{TP} + \text{FN})} * 100 \quad (2)$$

$$\text{Specificity} = \frac{\text{TN}}{(\text{TN} + \text{FP})} * 100 \quad (3)$$

$$\text{F1 Score} = \frac{2\text{TP}}{(2\text{TP} + \text{FP} + \text{FN})} \quad (4)$$

Accuracy, sensitivity, specificity, and F1 score are commonly used performance measures to evaluate the effectiveness of classification models. Accuracy measures the overall accuracy of the model's predictions by calculating the ratio of correctly classified samples to the total number of samples in the dataset. Provides an overview of the model's performance. Accuracy is useful when the dataset is balanced. However, it can be misleading when the dataset is unbalanced, as the model can achieve high accuracy by only predicting the majority class. Sensitivity measures the model's ability to accurately identify positive samples. Calculates the ratio of true positive estimates to the total number of true positive samples. Precision is especially important when the cost of false negatives is high. For example, in medical diagnosis, it is crucial to accurately identify individuals with a disease to provide timely treatment. Specificity measures the model's ability to accurately identify negative samples. Calculates the ratio of true negative estimates to the total number of true negative samples.

Specificity is important when the cost of false positives is high. For example, in airport security, accurate identification of innocuous objects as negative can help prevent unnecessary delays and inconvenience for passengers. The F1 score is a harmonic mean of precision and recall (precision). It provides a single measurement that balances both measurements. It is particularly useful when there is an imbalance between classes in the dataset. The F1 score ranges from 0 to 1; where 1 indicates the best possible model performance. Together, these metrics provide a comprehensive assessment of the model's performance (F1 score), taking into account different aspects such as overall accuracy, ability to identify positive patterns (sensitivity), ability to identify negative patterns (specificity), and a balanced measure of precision and recall.

In our study, the 5-fold cross-validation test, the details of which are shown in Figure 6, was applied in the classification process. The results of the metrics obtained in each fold of the cross-validation test are given in Table 3 for VGG16, Table 4 for ResNet50, and Table 5 for DenseNet201.

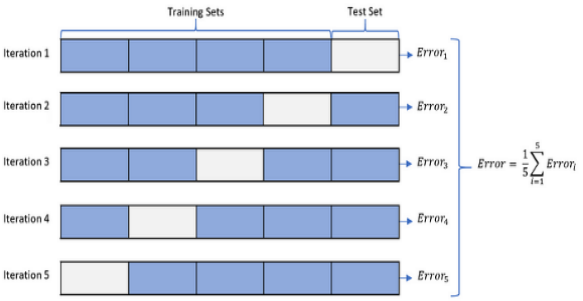

Fig. 6. 5-Fold Cross Validation Schema

Looking at the results obtained in Tables 3, 4, and 5, it is seen that different values can be obtained in the same method for each fold. The reason for this is that the randomly determined training and test subsamples in each fold are different. For this reason, in such studies, it is important for the reliability and accuracy of the results to be cross-validated, such as 5-fold or 10-fold, instead of separating the data as 30%-70% test and training data.

Table 6 shows the results of the transfer learning methods used in our study, with and without data augmentation. When the results in the table are evaluated, it does not seem possible to say that data augmentation should be applied or it should not be applied. Because when we look at the Accuracy rates, it is seen that the success of the three methods applied decreases when the data is increased. When the sensitivity values are examined, it is seen that the success rate of 74.99% in the VGG16 method increased to 86.87% after the data increase. In ResNet50 and DenseNet201, it is observed that data increase decreases the Sensitivity value. Looking at the F1 Score metric, which produces more realistic results in unbalanced data sets, it is observed that data augmentation in VGG16 and ResNet50 methods increases success. In DenseNet201, on the other hand, the success decreased as a result of the data increase.

Data augmentation does not always guarantee an increase in success in transfer learning methods. While data augmentation is a powerful technique that can help improve generalization and performance in many situations, its effectiveness depends on several factors and there are cases where it may not lead to a significant improvement. In certain situations, aggressive data augmentation can lead to overfitting, especially when the target task has relatively small amounts of data. Overfitting occurs when the model learns to memorize augmented examples rather than understanding underlying patterns. Highly complex models may have sufficient capacity to learn from limited original data without requiring extensive data augmentation. In such cases, augmentation may not yield significant benefits. If the target task data is unbalanced, data augmentation may not be able to deal with this problem effectively and may even exacerbate the class instability problem.

Since the numbers of diseased and healthy images in the data set do not show a balanced distribution, it is thought that it is more accurate to evaluate according to the F1 Score among the metrics. As can be seen from Table 6, the most successful F1 Score of 0.98 was obtained with the DenseNet201 method. The lowest results in F1 score values were obtained in the VGG16 method.

Table 8 shows the time complexity of the 3 different methods used in the study. As seen in the table, ResNet50 was the method that performed the transactions in the shortest time. One of the most important reasons for this is the number of layers and parameters given in Table 1. ResNet50 was the fastest method with 23 million parameters and 50 layers.

Table 3 VGG16 Performance Measurement Results

	VGG16 no Augmentation				**VGG16 with Augmentation**			
	Acc.	Sen.	Spe.	F1	Acc.	Sen.	Spe.	F1
Fold1	44,68	21,88	93,33	0,35	55,32	75,00	13,33	0,70
Fold2	91,49	93,75	86,67	0,94	72,34	81,25	53,33	0,80
Fold3	91,49	87,50	100,00	0,93	68,09	100,00	0,00	0,81
Fold4	100,00	100,00	100,00	1,00	82,98	90,63	66,67	0,88
Fold5	80,85	71,87	100,00	0,84	82,98	87,50	73,33	0,88
Mean	81,70	75,00	96,00	0,81	72,34	86,88	41,33	0,81

Table 4 ResNet50 Performance Measurement Results

	ResNet50 no Augmentation				**ResNet50 with Augmentation**			
	Acc.	Sen.	Spe.	F1	Acc.	Sen.	Spe.	F1
Fold1	91,48	96,87	80,00	0,93	89,36	96,87	73,33	73,3333
Fold2	93,61	100,00	80,00	0,95	93,61	100,00	86,66	86,6667
Fold3	91,48	100,00	73,33	0,94	100,00	100,00	100,00	100,00
Fold4	93,61	90,62	100,00	0,95	100,00	100,00	100,00	100,00
Fold5	93,61	100,00	80,00	0,95	100,00	100,00	100,00	100,00
Mean	92,76	97,50	82,66	0,94	96,59	99,37	92,00	92,00

Table 5 DenseNet201 Performance Measurement Results

	DenseNet201 no Augmentation				**DenseNet201 with Augmentation**			
	Acc.	Sen.	Spe.	F1	Acc.	Sen.	Spe.	F1
Fold1	93,61	100,00	80,00	0,95	89,36	96,87	73,33	0,92
Fold2	97,87	100,00	93,33	0,98	89,36	100,00	66,66	0,92
Fold3	100,00	100,00	100,00	1,00	95,74	100,00	86,66	0,96
Fold4	100,00	100,00	100,00	1,00	87,23	96,87	66,66	0,91
Fold5	100,00	100,00	100,00	1,00	95,74	100,00	86,66	0,96
Mean	98,29	100,00	94,66	0,98	91,48	98,75	76,00	0,94

Table 6 Performance Measurement Results of All Methods

Method	**Augmentation**	**Accuracy**	**Sensitivity**	**Specificity**	**F1 Score**
VGG16	No	81,70	74,99	96,00	0,81
VGG16	Yes	72,34	86,87	41,33	0,81
ResNet50	No	96,59	99,37	92,00	0,92
ResNet50	Yes	92,76	97,50	82,66	0,94
DenseNet201	No	98,29	100,00	94,66	0,98
DenseNet201	Yes	91,48	98,75	76,00	0,94

Table 7 Comparing similar studies in the literature

Study	**Image Type**	**Method(s)**	**Accuracy Rate (%)**
[5]	Lemon	Xception	94.34
[6]	Citrus	GLCM	85.71
[7]	Tomato	Convolutional Neural Network (CNN) and Learning Vector Quantification (LVQ) algorithms	86.00
[9]	Grape	K-means SVM	88.89
[10]	Rice	KNN, J48, Naive Bayes, and Logistic Regression	97.00
[11]	Tomato	VGG16, InceptionV3, and MobileNet,	91.2
[12]	Tomato	CNN	97.05
This Study	Lemon	VGG16, ResNet50, and DenseNet201	98.29

Table 8 Time complexity of the methods

Method	Fold 1	Fold 2	Fold 3	Fold 4	Fold 5
VGG16	28 Min 56 Sec	26 Min 55 Sec	27 Min 6 Sec	27 Min 31 Sec	26 Min 56 Sec
ResNet50	19 Min 14 Sec	17 Min 42 Sec	17 Min 28 Sec	17 Min 29 Sec	17 Min 30 Sec
DenseNet201	34 Min 3 Sec	26 Min 47 Sec	27 Min 45 Sec	31 Min 43 Sec	30 Min 37 Sec

5. Conclusion and Discussion

In our study, the classification process was carried out with three different deep transfer learning methods (VGG16, ResNet50, and DenseNet201) using lemon leaf images. While performing these processes, the results were also evaluated by increasing the data. The results obtained in the lemon leaf data set did not reveal a clear finding for data augmentation. While some methods have more successful results with data augmentation, more successful results have been obtained in some methods without data augmentation. In the deep transfer learning methods used, the highest accuracy rate was obtained with the DenseNet201 method, with an accuracy rate of 98.29% and an F1 Score of 0.98. Among the three methods used, the lowest measurement metrics were obtained with the VGG16 method. As a result of the study, it has been seen that transfer learning methods can distinguish diseased and healthy lemon leaves at a high rate. It is also one of the points obtained as a result that data augmentation does not always increase success.

When Table 7 is examined, it is seen that the leaves of different types of plants are classified in the studies carried out in the literature. In Table 7, it is seen that deep learning and transfer learning methods are frequently preferred, however, classical methods continue to be used. When the success rates in Table 7 are examined, it is seen that our study ranks first among the studies compared.

In future studies, the status of data augmentation can be evaluated by applying more transfer learning methods to different image data. Again, since the binary classification process was performed in this study, it was concluded that it would be appropriate to evaluate the situation of data augmentation in classification probes belonging to more than two classes in future studies.

Author Contribution

Data curation – Ahmet Saygılı (AS); Formal analysis - AS; Investigation - AS; Experimental performance - AS; Data collection - AS; Processing - AS; Literature review - AS; Writing - AS; Review and editing - AS.

Declaration of Competing Interest

The authors declared no conflicts of interest with respect to the research, authorship, and/or publication of this article.

References

[1] Ahmad, I., Hamid, M., Yousaf, S., Shah, S. T., Ahmad, M. O. (2020). Optimizing pretrained convolutional neural networks for tomato leaf disease detection, *Complexity*, vol. 2020, 1-6.

[2] FAO. "A Third More Mouths to Feed, FAO, Roma, Italy." http://www.fao.org/news/story/en/item/35571/icode/, Access Date: 02.06.2023.

[3] Sujatha, R., Chatterjee, J. M., Jhanjhi, N., Brohi, S. N. (2021). Performance of deep learning vs machine learning in plant leaf disease detection, *Microprocessors and Microsystems*, vol. 80, p. 103615.

[4] Liliane, T. N. & Charles, M. S. (2020). Factors affecting yield of crops, *Agronomy-climate change & food security*, p. 9, 2020.

[5] Subramanian, B., Jayashree, S., Kiruthika, S., Miruthula, S. (2019), Lemon leaf disease detection and classification using SVM and CNN, *International Journal of Recent Technology and Engineering*, vol. 8, no. 4, pp. 11485-11488.

[6] Banni, R. & Sksvmacet, L. (2018), Citrus leaf disease detection using image processing approaches, *International Journal of Pure and Applied Mathematics*, vol. 120, no. 6, pp. 727-735.

[7] Sardogan, M., Tuncer, A., Ozen, Y. (2018) Plant leaf disease detection and classification based on CNN with LVQ algorithm, in 2018 3rd international conference on computer science and engineering (UBMK), 2018: IEEE, pp. 382-385.

[8] Rastogi, A., Arora, R., Sharma, S. Leaf disease detection and grading using computer vision technology & fuzzy logic, in 2015 2nd international conference on signal processing and integrated networks (SPIN), 2015: IEEE, pp. 500-505.

[9] Padol, P. B. & Yadav, A. A., SVM classifier based grape leaf disease detection, in 2016 Conference on advances in signal processing (CASP), 2016: IEEE, pp. 175-179.

[10] Ahmed, K., Shahidi, T. R., Alam, S. M. I., Momen, S. Rice leaf disease detection using machine learning techniques, in 2019 International Conference on Sustainable Technologies for Industry 4.0 (STI), 2019: IEEE, pp. 1-5.

[11] Agarwal, M., Singh, A., Arjaria, S., Sinha, A., Gupta, S. (2020) ToLeD: Tomato leaf disease detection using convolution neural network, *Procedia Computer Science*, vol. 167, pp. 293-301.

[12] Irmak, G., Saygili, A. (2020). Tomato leaf disease detection and classification using convolutional neural networks," in 2020 Innovations in Intelligent Systems and Applications Conference (ASYU), 2020: IEEE, pp. 1-5.

[13] Kurmi, Y., Saxena, P., Kirar, B. S., Gangwar, S., Chaurasia, V., Goel, A. (2022), Deep CNN model for crops' diseases detection using leaf images, *Multidimensional Systems and Signal Processing*, vol. 33, no. 3, pp. 981-1000.

[14] Chen, W., Chen, J., Zeb, A., Yang, S., Zhang, D. (2022). Mobile convolution neural network for the recognition of potato leaf disease images, *Multimedia Tools and Applications*, vol. 81, no. 15, pp. 20797-20816.

[15] Elfatimi, E., Eryigit, R., Elfatimi, L. (2022). Beans leaf diseases classification using MobileNet models, *IEEE Access*, vol. 10, pp. 9471-9482, 2022.

[16] Anonymous. Healthy vs. Diseased Leaf Image Dataset (Public Domain). https://www.kaggle.com/datasets/amandam1/healthy-vs-diseased-leaf-image-dataset, Access Date: 05.05.2023.

[17] Simonyan, K. &. Zisserman, A. (2014). Very deep convolutional networks for large-scale image recognition, arXiv preprint arXiv:1409.1556.

[18] He, K., Zhang, X., Ren, S., Sun, J. (2016). Deep residual learning for image recognition, in Proceedings of the IEEE conference on computer vision and pattern recognition, pp. 770-778.

[19] Huang, G., Liu, Z., Van Der Maaten, L., Weinberger, K. Q. (2017). Densely connected convolutional networks," in Proceedings of the IEEE conference on computer vision and pattern recognition, pp. 4700-4708.

[20] Sahinbas, K. &. Catak, F. O. (2021). Transfer learning-based convolutional neural network for COVID-19 detection with X-ray images," in Data science for COVID-19: Elsevier, pp. 451-466.

[21] S. Mukherjee. "ResNet50." https://towardsdatascience.com/the-annotated-resnet-50-a6c536034758, Access Date: 05.06.2023.

[22] Sharma, N., Saba, L., Khanna, N. N., Kalra, M. K., Fouda, M. M., Suri, J. S. (2022). Segmentation-Based Classification Deep Learning Model Embedded with Explainable AI for COVID-19 Detection in Chest X-ray Scans, *Diagnostics*, vol. 12, no. 9, p. 2132, 2022.

European Journal of Engineering and Applied Sciences

ISSN: 2651-3412 (Print) & 2667-8454 (Online)
Journal homepage: http://dergipark.gov.tr/EJEAS
Published by Çorlu Faculty of Engineering, Tekirdağ Namık Kemal University

European J. Eng. App. Sci. 6(1), 41-49, 2023

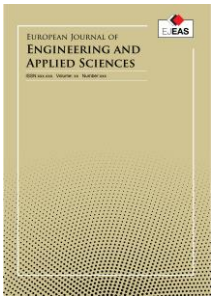

Research Article

Presenting Water Quality Characteristics of Lake Salda, Turkey

Asude Hanedar[1,*], Ayşegül Tanık[2]

[1]Department of Environmental Engineering, Çorlu Faculty of Engineering, Namık Kemal University, Çorlu- Tekirdağ, Turkey, 59860
[2]Department of Environmental Engineering, Faculty of Civil Engineering, Istanbul Technical University, Maslak,Istanbul-Türkiye, 34469

*[1]ahanedar@nku.edu.tr , [2]tanika@itu.edu.tr

Received: 11.02.2023 Accepted: 18.05.2023 DOI: 10.55581/ejeas.1250016

Abstract: Inland water bodies, either flowing or non-flowing all around the world, are under the adverse effect of both the climate change and anthropogenic activities. The water surface areas of lakes and wetlands diminish over time and thus, this global reality brings together the deterioration of water quality especially if such water bodies confront with a variety of human activities exerting pollutants. An example of such a vulnerable ecosystem is the Lake Salda located in the southwestern part of Turkey. This lake has gained the attention of international public due to its similarities with Mars. Over a long period of time, many researches have been conducted in this lake by different disciplines and scientists to better understand its unique features. In this study, water samples from the three selected stations on the lake at three different depths were collected and analyzed on physico-chemical parameters, organic matter content, nutrients, metals and semi metals according to national legislation and Water Framework Directive (WFD) of EU. The results are tabulated and analyzed in detail considering the potential pollution sources arising from the lake's basin. The pollutants are linked with the experimental measurements, and those parameters that exceeded the Environmental Quality Standards (EQS) are underlined. It is for sure that the lake necessitates utmost care and attention according to the results achieved.

Keywords: *Environmental Quality Standards, Lake Salda, Water Quality, Water Quality*

Su Kalitesi Durum Değerlendirmesi- Salda Gölü, Türkiye

Öz. Tüm dünyada iç su kütleleri hem iklim değişikliğinin hem de antropojenik faaliyetlerin olumsuz etkisi altındadır. Göllerin ve sulak alanların su yüzey alanları zamanla azalır ve bu küresel gerçeklik, özellikle su kütleleri çeşitli insan faaliyetleriyle karşı karşıya kalırsa, su kalitesinin bozulmasını beraberinde getirir. Bu tür hassas bir ekosisteme örnek, Türkiye'nin güneybatısında yer alan Salda Gölü'dür. Salda Gölü, Mars ile olan benzerlikleri nedeniyle uluslararası kamuoyunun ilgisini çekmiş, gölün spesifik özelliklerini daha iyi anlamak için farklı disiplinler ve bilim adamları tarafından birçok araştırma yapılmış ve su kalitesi zaman içinde belirli parametrelerle ortaya konmuştur. Çalışma kapsamında gölde seçilen üç istasyondan üç farklı derinlikte toplanan su örneklerinde hem ulusal mevzuatta hem de AB'nin Su Çerçeve Direktifinde (SÇD) belirtilen fiziko-kimyasal parametreler, organik madde içeriği, besinler, metaller ve yarı metallerin analiz sonuçları sunulmuş, Çevresel Kalite Standartlarını (ÇKS) aşan parametrelere dikkat çekilerek potansiyel kirlilik kaynakları ile birlikte sonuçlar değerlendirilmiştir. Elde edilen sonuçlarla göre gölün azami dikkat ve özen gerektirdiği bir kez daha ortaya konmuştur.

Anahtar Kelimeler: *Çevre Kalite Standardı, Salda Gölü, Su Kalitesi, Su Kirliliği*

* Corresponding author
E-mail: ahanedar@nku.edu.tr (A. Hanedar)

1. Introduction

Lake Salda, a local site in Turkey as different from the worldwide recognized areas, bears unique beauty. The lake has attracted a significant number of tourists in the recent years due to the interest of international media as it has some common properties with Mars [1]. The lake has been cited among the major soda lakes of the world [2]. As known, soda lakes occur worldwide and they seem to be associated with active tectonic and volcanic zones. There are 66 soda lakes in the world; among which 24 of them exist in the Asia continent [3].

The water clarity of Lake Salda has been compared with the Maldives and its surface properties with Mars [4]. It has been revealed that the magnesium-rich white rocks found within the lake are also found in Mars as referred by the work of [5]. The most relevant analogy to the Jezero Crater carbonates may be provided by Lake Salda, around which hydro-magnesite strandline terraces lie, including a hydro magnesite-cemented fan delta with beach deposits of hydro magnesite, including stromatolites, and pebbles of lizardite [6, 7]. As known, Jerezo Crater is the landing site of the NASA Mars 2020 rover (Figure 1). Figure 1 shows the image of Lake Salda belonging to June 8, 2020 as observed by the Operational Land Imager (OLI) on Landsat 8. The lake contains alluvial fans full of rock deposits eroded and washed down from the surrounding bedrock.

Lakes are one of the most important components of natural resources. Due to its unique features, Lake Salda has recently attracted the attention of both national and international scientists and some studies have so far been carried out on the lake to explore its main physical, chemical and biological characteristics beyond its interesting geological formation and hydrological behavior. The origin and recharging properties of groundwater and surface water has been investigated by using environmental isotopic, radiocarbon and physicochemical characteristics [8, 9]. In a study conducted on its groundwater characterization, high arsenic concentrations were found and Magnesium Hazard (MH) values were also determined to be an important problem in use as irrigation water [10]. In another recent study, the scientists conducted biotic and abiotic imprints on Mg-rich stromalites [11]. Such researches aim to provide new insights of the formation pathway of Mg-rich carbonates not only for local geological records; but also, for planetary bodies like Mars.

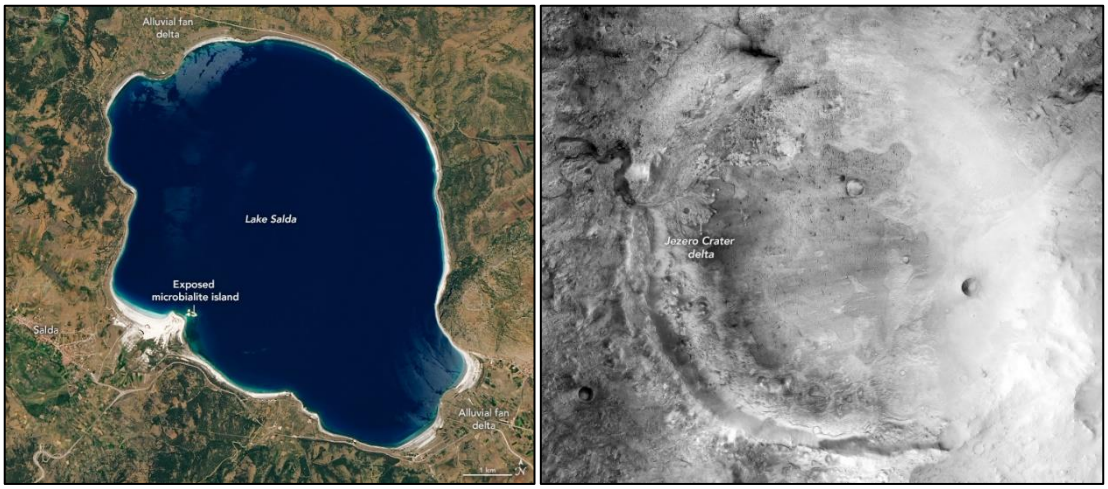

Fig. 1. *Lake Salda in 2020 and Jezero Crater in 2017 [12]*

Almost 4.6% decrease was observed in the water surface area of the lake between 1972-2019 as a result of a spatial analysis with the aid of Geographical Information Systems (GIS), and statistical analysis of the meteorological data and satellite images has been determined. According to the assessment of these works, Lake Salda has also been experiencing adverse effects of climate change over years like many of the other lakes in the same region [13]. Similarly, the shoreline changes in the lake up to 16.35 m/year between 1975 and 2019 were calculated [14]. Based on the results of the study, there was a considerable decrease in the lake area. In another study where the limnological character of the lake was presented, it is indicated that the lake highly is threatened by dropping water levels and organic pollution [15]. In a research conducted to determine the water quality of the lake and to evaluate its prevailing hydro-geochemical processes, it was found that the dominant water type of the lake is Mg-CO_3-HCO_3, and the lake was of Class I in terms of temperature, dissolved oxygen, NH_4 and NO_2 parameters according to USEPA regulations [16]. However, the water belonged to Classes II, III, IV and even V with respect to pH, electrical conductivity (EC), NO_3, biochemical oxygen demand (BOD), oxygen saturation, As and Cr in different periods. The increase in the As and Cr concentrations was considered to be geo-genic in origin.

Even though quite a lot of studies exist on the various features of Lake Salda, an overall water quality characterization and evaluation involving a high number of parameters to determine its physicochemical properties, organic matter and nutrient concentrations together with metals and semi metals presence based on annual water sampling results was lacking. This study attempts to fulfill this gap in the scientific arena through

presenting the yearlong monitoring results of 2018 and assessing the water quality status according to the revised National Regulation on Surface Water Quality dated 2021. Conducting studies on the control of pollution in this lake are important not only for the preservation of the existence of natural resources, but also for the sustainability of studies on life at Mars.

Within the scope of this study, anthropogenic point and non-point (diffuse) pollutant loads arising from the lake's basin and ending in the lake were identified and calculated, year-around water samples were taken and experimental analyses were carried out for pollution monitoring. The physico-chemical parameters, organic matter, nutrients, metals and semi metals were evaluated according to both the national water quality standards and Water Framework Directive (WFD) of European Union (EU) [17]. Moreover, the need to reduce pollutants exceeding the Environmental Quality Standards (EQS) were determined based on the quantitative values of pollution loads to which the lake was exposed. In that sense, this article is the first attempt to put forth the detailed water quality assessment that aims to give feedback to the decision-makers and related local authorities in charge of its management for the sake of its sustainability.

2. Materials and Methods

2.1. Study Area

Lake Salda is a natural park located within the district of Yesilova in Burdur Province of Turkey (Figure 2). It has a surface area of 45 km^2 located within a closed basin and stands at 1,139 m above the sea level [18]. It is known as the 3rd deepest lake of the country with a depth of 184 m. It is highly alkaline (pH 8-10) and magnesium rich [19]. The groundwater of the area recharges the lake, where it is intensively used for drinking, domestic and irrigation purposes.

Lake was declared as a Special Environmental Protection Area in 2019, and it has been registered as a 1st degree Natural Protection Area in 1989. At the same time, as the lake has a sensitive and fragile ecosystem, it is classified as an 'Important Plant Area' (IPA) and 'Important Bird Area' (IBA) according to international criteria [20, 21]. Lake Salda owns a rich biodiversity and bears satisfactory sheltering, breeding and nesting conditions for the endemic and endangered species. Within this context, the Ministry of Environment and Forestry of the Republic of Turkey (TR) stated that the area is a habitat to 301 aquatic and terrestrial species belonging to 61 families, among which 20 of such species are endangered and endemic [22]. With its snow-white sand based on its geological properties faces the risk of vanishing. Due to the human-induced activities of the recent years, it has started to darken. The dams and reservoirs built near the lake for providing irrigation water to the agricultural fields, and presence of stone and marble quarries on the mountains and their skirts has significantly cut and/or diminished freshwater entrance to the lake. Therefore, the balance of the water feeding the lake and lost through evaporation has been spoilt recently. The main reasons for the changes in the shorelines were the structures such as irrigation ponds and dams built on the rivers that recharge the lake, and changes in precipitation/temperature conditions [14]. The small beaches on the southwest and southeast coasts of the lake are used for recreational purposes due to the cleanliness of the turquoise-colored water.

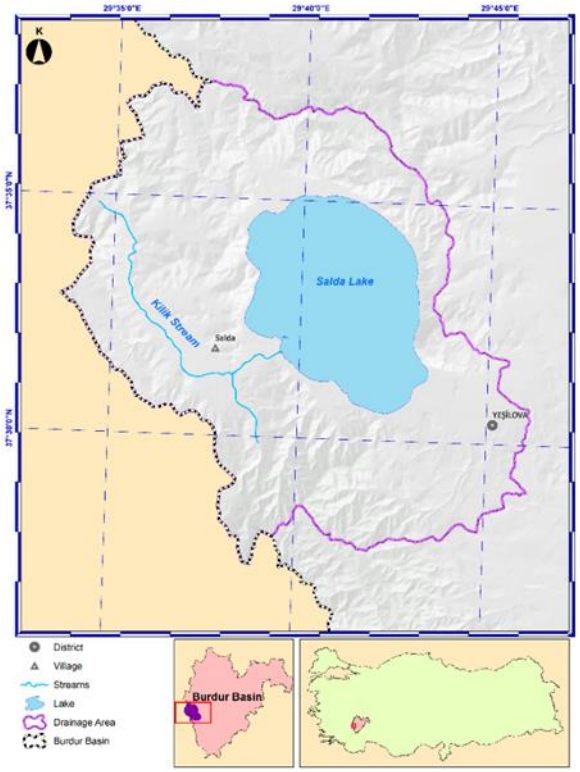

Fig. 2. *Lake Salda and its location in Turkey*

2.2. Sampling and Analyses

Water sampling study was carried out at three points (L1, L2 and L3) within the lake between January-December 2018. Samples from each of the sampling stations were taken at three different depths; namely, surface, mid and bottom layers. 8 physicochemical, 3 organic matter, 8 nutrient parameters and 27 metal/semi metals were analyzed monthly and/or once every three months representing seasonal variations.

In all sampling work, 5-liter prewashed amber glass bottles were shipped to the laboratory. Samples were transported to the laboratory and stored at 4°C until analysis. Temperature, pH, dissolved oxygen, turbidity, secchi disc measurements were carried out in the field.

Pre-processing and analysis of metals was performed in dissolved and total phase according to EN ISO 17294 1-2 methods. Water samples for trace metal analyses were filtered through 0.45 µm acetate-cellulose filters, the filtrate was taken in 50 mL plastic vials and acidified with 0.5 mL of analytically pure HNO_3. After pre-processing and microwave extraction, it was analyzed by ICP-MS device from Agilent Technologies.

The plasma conditions were forward power (1550 w), gas flow rate (15 L/min), auxiliary gas flow rate (0.9 L/min) and nebulizer gas flow rate (1.1 L/min). The recovery was in the range of 85-99%. It was analyzed with the quality control solution before each run (Level of Quantification (LOQ): 0.02-1 µg/L; Level of Detection (LOD): 0.007-0.3 µg/L). The recovery was in the range of 85-99%. Locations of the 3 sampling points are shown in Figure 3.

2.3. Pressures and Threats on the Lake Basin

The limnological character of the lake has been threatened by decrease in water levels and organic pollution [15]. Point and diffuse anthropogenic sources of pollutants were determined in the lake basin that would affect the water quality as follows;

- There are direct domestic wastewater discharges from two settlements to the lake; Yeşilova district with a population of 6908 and Salda Village with 1104 inhabitants. Other than that, there are no other point sources generating pollution in the basin (Point pollutants).
- There exists an unsanitary solid waste landfill in the basin with a surface area of 4756 m^2 (Diffuse pollutants).
- There are four chrome-mining sites (Diffuse pollutants).
- Livestock activities are carried out with annual breeding of 2223 bovine and 13639 ovine (Diffuse pollutants).

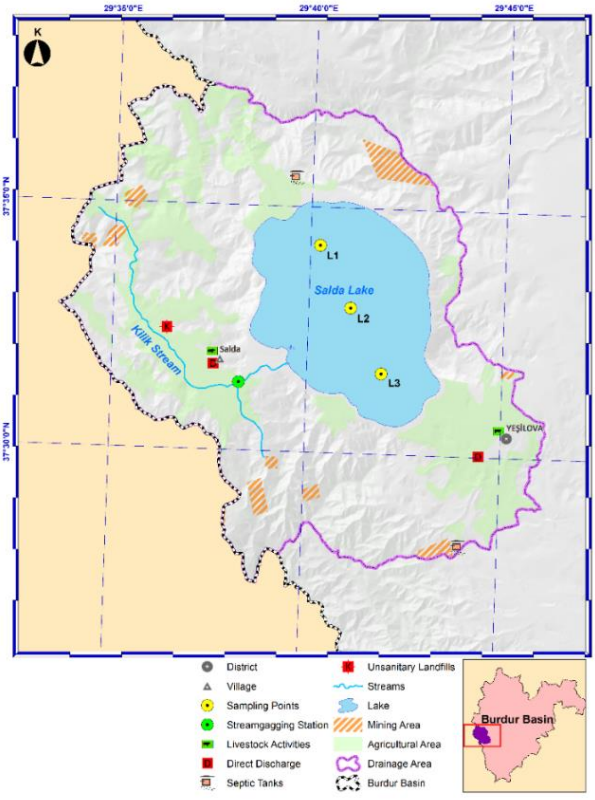

Fig. 3. *Pressures in the lake's drainage area*

3. Results and Discussion

The water quality of Lake Salda has been searched for a yearlong

- Agricultural activities prevail on an approximate area of 3121 hectares. Total annual fertilizer use has been calculated as 3645 tons in the basin [23] (Diffuse pollutants).
- Highways with two or more lanes pass through the south and southeast of the lake as part of the main transportation network (Diffuse pollutants).

Leachate arising from the unsanitary landfill, agricultural irrigation return flow, animal manure, mining outputs, and vehicles emissions are addressed as the different types of diffuse pollutants arising from the lake basin. The point loads calculated from the available sources and the diffuse loads estimated either by obtaining data from the local officials or by using unit loads appearing in the literature are given in Table 1 in the form of percent distribution of Total Nitrogen (TN) and Total Phosphorous (TP) [23].

Table 1. Total N and P loads in the lake basin

Parameters	Total Nutrient Load (t/year)	Point Sources (%)	Diffuse sources (%)
TN	203.5	7	93
TP	14	17	83

and the results of the experimental analyses are given in detail in Table 2. The data analyses are categorized according to the groups of parameters involved. Physico-chemical parameters, organic matter characterization and derivatives of nutrients are listed initially, and the three Water Quality Classes ranked from best to worst are used to define the situation of the lake according to the Revised National Regulation on Surface Water Quality dated 2021, Annex 5 Table 2 [24].

In Table 2, the number of samplings throughout the year are shown by n, while minimum, maximum, average, median and standard deviation values are calculated. All the measurements of the lake throughout sampling period are compiled and analyzed. Average values are considered for defining the water quality classes defined in the national regulation which is in full compliance with Water Framework Directive (WFD) of EU.

In terms of dissolved oxygen, BOD_5 and nutrients Class I quality has been attained and the alkaline character with pH 9, as a major property of the lake, is clearly observed.

Due to the unique characteristics of Lake Salda, it is known that heavy metal concentrations of natural origin are quite high. This situation causes problems in the evaluation of heavy metals measured in the lake in accordance with WFD standards, and the measured values are determined above the limit values in almost all cases. According to WFD, Member States are required to calculate natural background concentrations (NBC) for metal compounds where concentrations prevent compliance with the relevant EQS. Accordingly, the EQS for the relevant pollutants is taken as equal to the revised annual average (AA) environmental quality standards (AA-EQS) as a result of the

natural background concentration calculations.

Variety of semi metals and metals are analyzed according to annual average (AA-EQS) and maximum allowable concentration (MAC) regarding the EQS stated in RSWQ (2021) Annex 5-Table 3 [24]. The averages derived from the results indicate that the lake is rich in Mg and Na concentrations as expected. Al, Zn, Fe, Pb, Co and Ni exceeded the AA-EQS in the lake.

As, Fe and Al were abundant in the aquatic ecosystem, both were chosen as reference metals [25]. On the other hand, it has been revealed that Fe, Mg, Ni, Zn and Co sources can be associated with agricultural activities. These metals are known to be applied to the soil by fertilizers and pesticides in agricultural land [26, 27]. The contents of Co and Ni are commonly found in household products (stainless steel, batteries, etc.), and there are numerous ways of increased input of Pb, Co and Ni from urban areas such as domestic wastewater discharge, fossil fuel burning, etc. [26, 28]. Nickel is one of the priority substances according to WFD and Turkish standards, and is one of the important pollutants of anthropogenic origin in aquatic environments. It is used in the combustion of biomass and fossil fuels, domestic wastewater discharge, etc. As such, various resources are available for Ni [29, 30].

When the results obtained from this study are compared with the previous research of [16], Al (2-109 µg/L); Pb (0-16.4 µg/L); Zn (0.7-77.90 µg/L) values were consistent with the concentration levels obtained in this study, and the values measured for Fe (15-97 µg/L) and Ni (1.1-19.10 µg/L) were found to be lower than this study. The previous study also reported high As and Cr concentrations which were determined to be of geo-genic origin [16].

Among the parameters given in Table 2, those that will reveal the characteristics of the lake (temperature, electrical conductivity (EC), dissolved oxygen, alkalinity, Fe, Mg, Al and Ni) were further selected and the quality changes in the lake based on sampling depth (surface layer, mid layer, bottom layer) and time were also evaluated (Figure 4). Accordingly, when examining the temperature change with varying depth, it was observed that the temperatures on the surface varied on the average around 16 ^{0}C, 13 ^{0}C at the mid-depth and 11^{0}C at the bottom layer. Although the changes do not differ according to the location, the surface temperatures increased to 24^{0}C in July-August months. In February-March, when the temperature in the lake decreased the most, it was observed that the surface temperatures decreased to 7-8^{0}C.

EC values of the lake were high, and while the measured values from surface and mid-layers were close to each other, a slight decrease was observed at the bottom layer in all the three sampling points. No significant change was observed spatially and temporally.

When looking at the change of dissolved oxygen throughout the depth of the lake, it was observed that the values were around 8.6 mg O_2/L at the surface and increased to 9.3 mg O_2/L at the mid-layer and to 9.6 mg O_2/L at the bottom layer. The measured levels in each period and at each point in the lake were observed as above the WFD "very good" water quality level of 8 mgO_2/L. Dissolved oxygen levels increased from April to September during the year Regarding the organic matter concentration in the water ecosystem, one can say that BOD_5 presents Class I characteristics as expected in parallel to dissolved oxygen levels. However, COD concentrations lie within Class II and Class III characteristics indicating the presence of chemically oxidizable organic matter in the water rather than biologically degradable organics. Nutrient concentrations expressed in terms of nitrogen (N) and phosphorous (P) parameters and their derivatives, indicated no serious problem on the average; however, the maximum values detected underline the reality that there are signs of nutrient pollution in the lake system at certain time intervals. This situation is important nutrients arise both from untreated domestic discharges and from any of the diffuse pollutants experienced in the basin of the lake.

The lake is an alkaline lake and its alkalinity level was detected around 1030 mg$CaCO_3$/L. There was no significant change in the alkalinity level in the lake depending on the location and depth. When the change over time was examined, it was observed that the highest values were obtained in September and October during the year of inspection.

Concentration of iron (Fe), as a heavy metal, generally increase with depth in stagnant water bodies. It can be stated that the variation of iron concentrations measured in the lake with depth varied according to the sampling point. As generally expected, in L1, iron concentration slightly increased with depth. In L2 and L3 points, the surface and bottom layer concentrations were close and higher, while the mid-layer concentrations were slightly lower. The concentration values in L3 varied over a wide range.

There is no classification or limit value for magnesium (Mg) among the WFD standards. When the change in Mg concentrations with depth in the lake was examined, it was observed that the mean values were quite close to each other in L1 and L2, and there was no significant change with depth. Concentration levels at these points varied around 350 mg/L. In L3, while the mid-layer and bottom layer Mg concentrations were close to each other and the values observed at other sampling points, some of the measurements exceeded 500 mg/L concentration on the surface layer of the lake.

Nickel (Ni) concentrations measured in the lake were generally around the AA-EQS value. The highest value was measured at the mid-layer of the L1 station. While the concentrations measured at the surface and bottom layers at the L1 point were closer, the concentration value measured at the medium level was high. An increase was observed in the level as one goes deeper at the L2 point. In L3, on the other hand, higher levels were observed at the surface.

Aluminum (Al) values measured in the lake were well above the limit value. In general, concentration levels ranging from 20-80 mg/L, although it varied in a wide range at the mid-layer in the

L1 station, closer values were obtained in terms of averages. At L2, lower and varying values in the narrow range were determined on the surface, slightly higher but wider range measurements were detected at L2 and L3 points. At the L3, the highest value was measured at the surface, and at the bottom point values were within an average of around 50 mg/L; but were varying in a wider range.

Table 2. Water quality characteristics of Lake Salda

Parameters		**Water Quality Classes***			**n**	**Max.**	**Min.**	**Aver.**	**Median**	**Std. Dev.**
Physico-chemical		**I**	**II**	**III**						
Temperature	°C	-			108	24.60	7.20	13.46	12.10	4.86
pH		6-9	6-9	6-9	108	9.72	7.89	8.99	9.29	0.58
Electrical Conductivity	µS/cm	< 400	1000	> 1000	99	2113	1909	2081	2081	28.91
Dissolved O_2	mg/L O_2	> 8	6	< 6	106	11.32	7.84	9.17	9.18	0.94
Turbidity	NTU	-			36	3.83	<0.02	0.67	0.55	0.83
Secchi Disc	M	-			12	15	6.40	11.22	11.70	3.37
TSS	mg/L	-			36	31.40	<2	2.15	1	5.26
Alkalinity	mg/L	-			36	1444	811	1031	924	229
Organic Matter										
BOD_5	mg/L	< 4	8	> 8	36	4.42	<2	1.13	1	0.59
COD	mg/L	< 25	50	> 50	36	138	10	65.02	58.40	40.92
TOC	mg/L				36	51.03	2.29	20.73	22.52	14.60
Nutrients										
NH_4-N	mg/L	< 0.2	1	> 1	36	0.44	<0.02	0.06	0.01	0.12
NO_2-N	mg/L				0	0.00	0.00	-	-	-
NO_3-N	mg/L	< 3	10	> 10	36	0.40	0.07	0.21	0.20	0.09
TKN	mg/L	< 0.5	1.5	> 1.5	36	0.87	<0.1	0.24	0.17	0.21
Organic N	mg/L				36	0.59	<0.08	0.19	0.13	0.18
TN	mg/L	< 3.5	11.5	> 11.5	36	0.98	<0.5	0.38	0.25	0.24
TP	mg/L	< 0.08	0.2	> 0.2	36	0.37	<0.075	0.06	0.04	0.08
Orto P	mg/L	<0.05	0.16	>0.16	0	0.00	0.00	-	-	-
Metals and Semi metals		**EQS**			**n**	**Max.**	**Min.**	**Aver.**	**Median**	**Std. Dev.**
		AA-EQS		**MAC-EQS**						
Aluminum	µg/L	2.2		27	36	138.14	10.75	46.58	42.37	25.62
Antimuon	µg/L	7.8		103	36	0.75	<0.3	0.33	0.15	0.21
Arsenic	µg/L	53		53	36	3.38	0.34	0.98	0.89	0.55
Copper	µg/L	1.6		3.1	36	4.07	<0.3	1.44	1.45	1.17
Barium	µg/L	680		680	36	14.64	2.21	6.40	5.80	2.57
Beryllium	µg/L	2.5		3.9	36	3.94	<0.3	0.44	0.15	0.75
Bore	µg/L	707		1472	36	840.61	<33	441.65	418.08	171.34
Zinc	µg/L	5.9		231	36	80.05	<0.3	29.86	27.81	18.63
Iron	µg/L	36		101	36	171.25	18.13	56.19	49.26	36.39
Silver	µg/L	1.5		1.5	36	0.74	<0.3	0.29	0.15	0.21
Cadmium	µg/L	< 0.08		< 0.45	108	0.55	<0.007	0.08	0.04	0.09
Tin	µg/L	13		13	36	1.73	<0.3	0.48	0.46	0.38
Calcium	mg/L				36	85.82	0.79	7.52	5.36	13.38
Cobalt	µg/L	0.3		2.6	36	2.01	<0.03	0.27	0.19	0.34
Chromium	µg/L	1.6		142	36	1.05	0.31	0.68	0.69	0.22
Lead	µg/L	1.2		14	108	25.32	0.98	2.39	2.01	2.40
Magnesium	mg/L				36	601.95	318.61	350.67	344.35	46.24
Manganese	µg/L				36	5.17	<0.3	2.02	2.11	1.14
Nickel	µg/L	4		34	108	86.08	0.60	4.69	3.36	8.62
Potassium	mg/L				36	32.03	21.85	27.02	27.47	2.95
Sodium	mg/L				36	1994.65	208.35	294.21	231.59	291.80
Titanium	µg/L	26		42	36	13.10	<3.3	2.37	1.65	2.27
Vanadium	µg/L	1.6		97	36	3.05	1.19	2.19	2.18	0.35
*Class I: Potable water quality; *Class II: Slightly polluted; *Class III: Polluted, **Natural Background Concentrations										

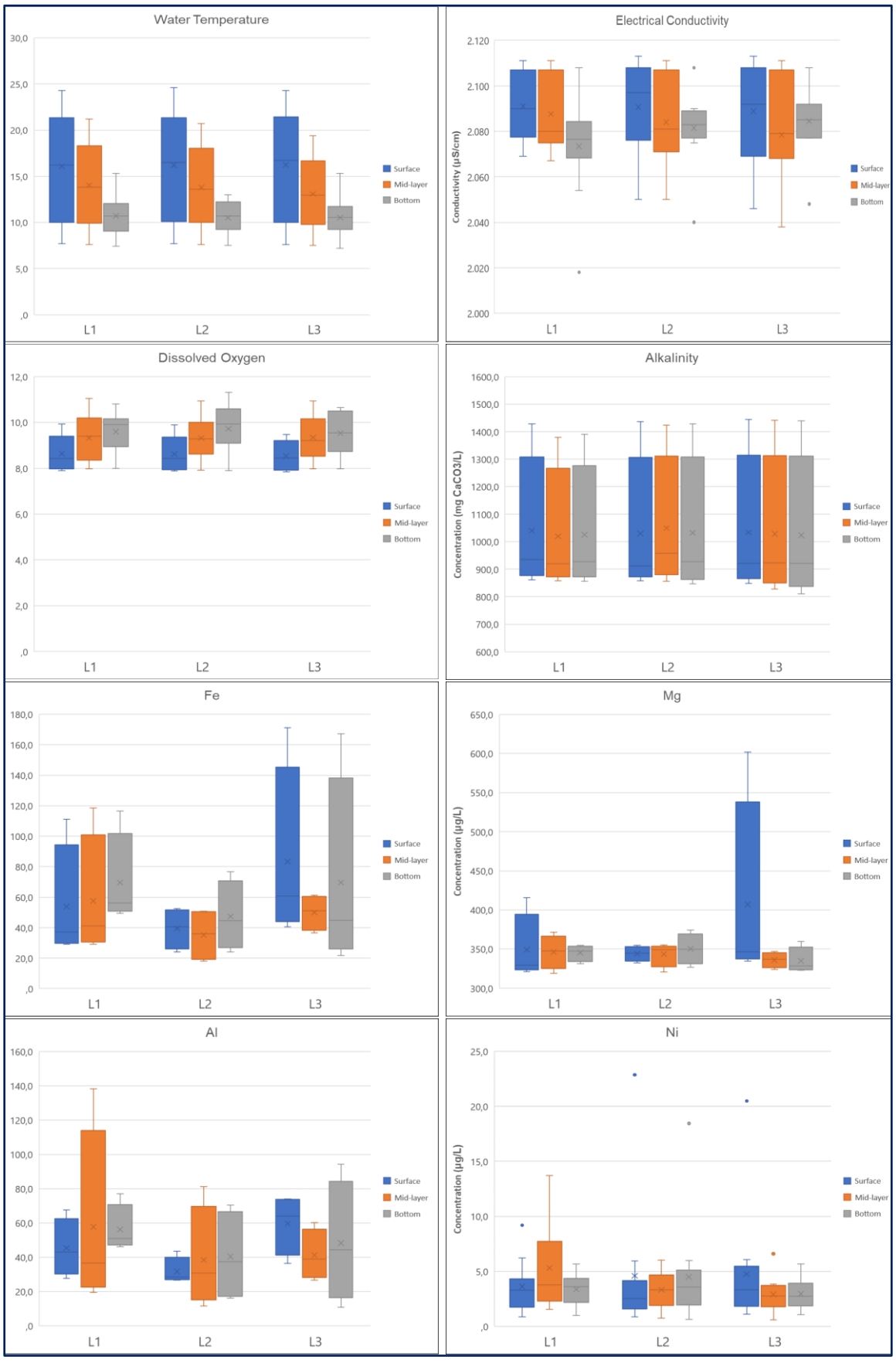

Fig. 4. *Variations of some parameters with depth*

4. Conclusion

Lake Salda, due to its natural intrinsic properties and unique features, it is observed within this study that anthropogenic activities and water loss through climate change effects accelerated its degradation as is the case in many of the world's stagnant water ecosystems. In that sense, Lake Salda is one of the lakes that should be taken under protection in due time. Therefore, as an initial step towards its protection from any further human-induced activities, the Turkish Government declared this lake and its basin as a Special Protection Area in 2019.

It is crystal-clear that the increase in anthropogenic activities will adversely affect the characteristics of any lake in the world. Thus, within the scope of this study, the existing pollution in the lake was put forth according to land-based sources of pollutants detailed as point and non-point (diffuse loads, monitoring of polluting parameters via experimental analyses were conducted for a year long, and thus, the prevailing water quality was presented for the attention of especially decision-makers and politicians so as to urge them to take the necessary measures to further prevent the deterioration of such a vulnerable lake ecosystem. Previous water quality determination efforts were rather based on some parameters; however, this study covers all the parameters that takes place in both the WFD and in the revised National Regulation on Surface Water Quality dated 2021.

Author Contribution

Data curation – A.H., A.T.; Formal analysis – A.H.; Investigation – A.T., A.H.; Data Collection – A.H., A.T.; Processing – A.T.; Literature review – A.H, A.T; Writing, review and editing – A.T., A.H.

Declaration of Competing Interest

The authors declared no conflicts of interest with respect to the research, authorship, and/or publication of this article.

Acknowledgements

The authors would like to express thanks to the General Directorate of Water Management under the Ministry of Agriculture and Forestry for realizing the Burdur River Basin Management Plan (RBMP) in which the year around water quality monitoring work was conducted.
This study utilized the corresponding data of various parameters analyzed during the realization of RBMP.

References

[1] Aybar D. H., E. Icigen (2020). A content analysis on the internet news about Lake Salda as a new destination. Mediterranean Journal of Humanities, vol. x, pp. 49-59, in Turkish. DOI: 10.13114/MJH.2020.517

[2] Kempe S., J. Kazmierczak (2011). Soda Lakes in Reitner, J., Thiel, V. (eds) Encyclopedia of Geobiology. Encyclopedia of Earth Sciences Series. Springer, Dordrecht, pp. 824-829, DOI: 10.1007/978-1-4020-9212-1_191

[3] USGS, (2022). Soda Lakes, U.S. Geological Survey https://www.usgs.gov/volcanoes/soda-lakes (accessed July 1, 2022)

[4] Kucukergin K. G., M. Gurlek (2020). What if this is my last chance?: developing a last-chance tourism motivation model. Journal of Destination Marketing and Management, vol. 18, no. 100491, 2020, DOI:10.1016/j.jdmm.2020.100491

[5] Russell M. J., Ingham J. K., Zedef V., Maktav D., Sunar F., Hall A. J., A. E. Fallick (1999). Search for signs of ancient life on Mars: expectations from hydromagnesite microbialites, Salda Lake, Turkey. Journal of Geological Society, vol. 156, no.5, pp. 869-888, 1999. DOI:10.1144/gsjgs.156.5.0869

[6] Shirokova L. S., Mavromatis V., Bundeleva I. A., Pokrovsky O. S., Bénézeth P., Gérard E., Pearce C. R., E. H. Oelkers (2013). Using Mg isotopes to trace cyanobacterially mediated magnesium carbonate precipitation in alkaline lakes. Aquatic Geochemistry, vol. 19, pp. 1-24, 2013. DOI: 10.1007/s10498-012-9174-3.

[7] Horgan B. H. N., Anderson R. B., Dromart G., Amador E. S., M. S. Rice (2019). The mineral diversity of Jerezo Crater: evidence for possible lacustrine carbonates on Mars. Icarus, vol. 339 no.113526, 2020. DOI:10.1016/j.icarus. 113526

[8] Varol S., Davraz A., Sener S., Kirkan B., Tokgozlu A., F. Aksever (2017). Project on the determination of pollution level and monitoring the hydrogeological and hydrogeochemical properties of Lake Salda Wetland. The Scientific and Technological Research Council of Turkey (TUBITAK), Project no: 114Y084.

[9] Varol S., Davraz A., Aksever F., Sener S., Sener E., Kirkan B., A. Tokgozlu (2020). Determination of the origin and recharge process of water resources in Salda Lake Basin by using the environmental, tritium and radiocarbon isotopes (Burdur/Turkey). Bulletin of the Mineral Research and Exploration, vol.161, pp.57-70. DOI:10.19111/bulletinofmre.604352

[10] Varol S., Davraz A., Aksever F., Sener S., Sener E., Kirkan B., A. Tokgozlu (2021). Assessment of groundwater quality and usability of Salda Lake Basin (Burdur/Turkey) and health risk related to arsenic pollution. Journal of Environmental Health Science and Engineering, vol.19, pp. 681-706. DOI:10.1007/s40201-021-00638-5, 2021.

[11] Balci N., Gunes Y., Kaiser J., On S. A., Eris K., Garczynski B., B. H. N. Horgan (2020). Biotic and abiotic imprints on Mg-rich stromatolites: lessons learnt from Lake Salda, SW Turkey. Geomicrobiology Journal, vol. 37, no.5, pp.401-425. DOI:10.1080/01490451.2019.1710784

[12] NASA, Earth Observatory, (2022). https://earthobservatory.nasa.gov/images/147041/jez-like-mars (accessed July 1, 2022)

[13] Ariturk S. K., B. Ustaoglu (2020). Determination of climate change impacts on Lake Salda Basin. Journal of Anatolian Cultural Researches, vol. 4, no.3, pp.233-249, in Turkish. DOI: 10.15659/ankad.v4i3.132

[14] Dereli M. A., E. Tercan (2020). Assessment of Shoreline Changes using Historical Satellite Images and Geospatial Analysis along the Lake Salda in Turkey. Earth Science Informatics, vol. 13, no.3, pp.709-718. DOI: 10.1007/s12145-

020-00460-x.

[15] Kazanci N., Girgin S., M. Dügel (2004). On the limnology of Salda Lake, a large and deep soda lake in southwestern Turkey: Future management proposals. Aquatic Conservation: Marine and Freshwater Ecosystems, vol.14, no.2, pp:151-162. DOI: 10.1002/aqc.609

[16] Davraz A., Varol S., Sener E., Sener S., Aksever F., Kırkan B., A. Tokgözlü (2019). Assessment of water quality and hydrogeochemical processes of Salda alkaline lake (Burdur, Turkey). Environ Monit Assess, vol.191, no.:701. DOI: 10.1007/s10661-019-7889-y.

[17] EC (European Commission), (2000). Directive 2000/60/EC of the European Parliament and of the Council of 23 October 2000 establishing a framework for Community action in the field of water policy. Off. J. Eur. Communities (327/1 22/12/2000).

[18] Temurcin K., Atayeter Y., U. Tozkoparan (2019). Tourism potential of Lake Salda and its vicinity and its impact on the socio-economic structure of Yesilova District. Suleyman Demirel University, Journal on Social Sciences of the Faculty of Arts and Sciences, vol.2, no.47, pp.40-63, in Turkish. DOI: 10.35237/sufesosbil.604016.

[19] Kaiser J., On B., Arz H., S. Akcer-On (2016). Sedimentary lipid biomarkers in the magnesium rich and highly alkaline Lake Salda (south-western Anatolia). Journal of Limnology, vol.75, no.3, pp.581-596. DOI: 10.4081/jlimnol.2016.1337.

[20] Kara V. M., Celep M., S. Kanigur (2020). Determining the physical carrying capacity of Lake Salda in the scope of overtourism. Journal of Tourism and Gastronomy Studies, vol.Special Issue (4), pp.79-92, in Turkish. DOI: 10.21325/jotags.2020.671.

[21] WWF (2021). World Wildlife Fund, There is no other place like Salda. https://www.wwf.org.tr/calismalarimiz/ormanlar/baska_salda_yok_/(accessed 11 March 2021) (in Turkish)

[22] MoEU (2021). Ministry of Environment and Urbanization, Lake Salda Special Environmental Protection Area. https://tvk.csb.gov.tr/salda-golu-i-91578 (accessed 11 March 2021) (in Turkish).

[23] WMGD (2020). Burdur River Basin Management Plan. Ministry of Agriculture and Forestry, Water Management General Directorate, 450 p., Ankara, Turkey (in Turkish).

[24] RSWQ (2021). Changes on the National Regulation on Surface Water Quality (RSWQ), Official Newspaper dated 16.06.2021 and numbered 31513.

[25] Islam M. S., Hossain M. B., Matin A., M. S. I. Sarker, (2018). Assessment of heavy metal pollution, distribution and source apportionment in the sediment from Feni River Estuary, Bangladesh. Chemosphere, vol.202, pp.25–32, 2018. DOI: 10.1016/j.chemosphere.2018.03.077.

[26] El-Hassanin A. S., Mamaka M. R., Abdel-Rahman G. N., Abu-Sree Y. H., E. M. Saleh (2020). “Risk assessment of human exposure to lead and cadmium in maize grains cultivated in soils irrigated either with low-quality water or freshwater. Toxicol Rep, vol.7, pp.10-15. DOI: 10.1016/j.toxrep.2019.11.018.

[27] Kayode O. T., Ogunyemi E. F., Odukoya A. M., Aizebeokhai A. P. (2022). Assessment of chromium and nickel in agricultural soil: implications for sustainable agriculture. IOP Conf. Ser.: Earth Environ. Sci., vol.993, no.012014. DOI: 10.1088/1755-1315/993/1/012014

[28] Zhang Y., Liu S., Cheng F., Coxixo A., Hou X., Shen Z., L. Chen (2018). Spatial distribution of metals and associated risks in surface sediments along a typical urban river gradient in the Beijing Region. Arch Environ Contam Toxicol, vol.74, pp.80-91, 2018. DOI: 10.1007/s00244-017-0462-1.

[29] Tian H. Z., Lu L., Cheng K., Hao J. M., Zhao D., Wang Y., Jia W., P Qiu (2012). “Anthropogenic atmospheric nickel emissions and its distribution characteristics in China.” Science of the Total Environment, vol.417-418, pp.148–157. DOI: 10.1016/j.scitotenv.2011.11.069.

[30] PubCHEM, (2020). National Center for Biotechnology Information. https://pubchem.ncbi.nlm.nih.gov/#query= (accessed July 1, 2022).